Lehrstuhl für Technische Elektrophysik
Technische Universität München

Modeling and Simulation of an Electrostatic Image Transfer

Dipl.-Ing. Univ. Rainer Hoffmann

Vollständiger Abdruck der von der Fakultät für Elektrotechnik und Informationstechnik der Technischen Universität München zur Erlangung des akademischen Grades eines

Doktor-Ingenieurs

genehmigten Dissertation.

Vorsitzender:	Univ.-Prof. Dr.-Ing J. S. Kindersberger
Prüfer der Dissertation:	1. Univ.-Prof. Dr. rer. nat. G. Wachutka
	2. Univ.-Prof. Dr.-Ing. W. Peukert, Friedrich-Alexander Universität, Erlangen-Nürnberg

Die Dissertation wurde am 24.01.2003 bei der Technischen Universität München eingereicht und durch die Fakultät für Elektrotechnik und Informationstechnik am 15.07.2004 angenommen.

Abstract

The various process steps of an electrophotographic printer are modelled to simulate the whole process from the exposure to the toner deposition on the photoconductor. The main part consists of a many-body simulation where the complex motion of a large number of toner particles is calculated by solving the equation of motion, where all relevant forces and the specific particle properties have been taken into account. The simulation results are calibrated by comparing them with appropriately simplified experiments prior to the simulation of the complete real printing process. Based on these simulations, the physical background of the essential process-specific effects is revealed.

Zusammenfassung

Die verschiedenen Teilschritte des elektrophotographischen Druckprozesses werden modelliert, um eine Simulation des Gesamtprozesses von der Belichtung bis zur Tonerablagerung auf dem Fotoleiter zu ermöglichen. Den Hauptteil bildet eine Vielteilchensimulation, bei der die komplexe Bewegung einer großen Menge von Tonerteilchen unter Berücksichtigung aller relevanten Kräfte sowie der spezifischen Teilcheneigenschaften durch Lösen der Bewegungsgleichungen berechnet wird. Die Simulationsergebnisse werden zuerst im Vergleich mit geeigneten, vereinfachten Experimenten kalibriert, um dann den kompletten, realen Druckprozess nachzubilden. Mit Hilfe der Simulation lassen sich die physikalischen Hintergründe der wichtigsten prozeßspezifischen Effekte erklären.

Meinen Eltern

Contents

List of Figures

Chapter 1

Introduction and process overview

1.1 Motivation

Since the first experiments, conducted by Chester Carlson and Otto Kornei in 1938 [DMB55], leading to the first commercially available electrophotographic equipment in 1950, the electrophotographic print process has become widely used due to its capability of high print performance, high print quality and low page costs [Sch75, Gol01]. Much effort has been made to further improve the process, especially for higher printing speed and increased resolution.[1] These issues have shown that further development can only be achieved by a deeper understanding of the physical mechanisms behind the process, whereas today many parameters can only be adjusted using empirical knowledge [SR99, BPÅ99].

In this work the physics of toner deposition on the photoconductor as the central part of the printing process will be modeled to be used as a basis for a realistic, predictive numerical simulation of the whole printing process. The last transfer step from the photoconductor to the paper or another medium is not included, since much work has already been done in this area [MT97, Tom98, ARO01] showing that simplified continuous models are sufficient to explain the experimental results.

The simulation of toner deposition conducted here consists of a many-body system where the motion of each particle is calculated based on the forces acting on it. The results of the simulations shall be compared with the results of real experiments to ensure its validity so that further time-consuming real experiments can be partly replaced by virtual ones (although the simulations require a significant amount of computation time there is no need of human interaction, so that the amount of working hours can be reduced compared to real experiments). These simulations allow to make predictions about the consequences of changes in the geometric or electric setup. Additionally, valuable hints for the further printer development can be drawn from the simulation due to its possibility of tracing the motion of single particles. This makes it possible, for example, to understand why particles are deposited in the background area (i.e. the part of the print area which should stay white), what influences the creation of sharp edges of small details or how to ensure a maximum optical density. The enhanced knowledge of the process enables the developers to improve the geometric design of the components, the electric and magnetic setup and the various active control loops.

[1] As of today (2003), typically commercially available high-speed printers use paper speed of up to 1.5 m/s, corresponding to 600 A4 images/minute at a print resolution of 600 dots per inch (dpi)

1.2 Process overview

1.2.1 Functional description

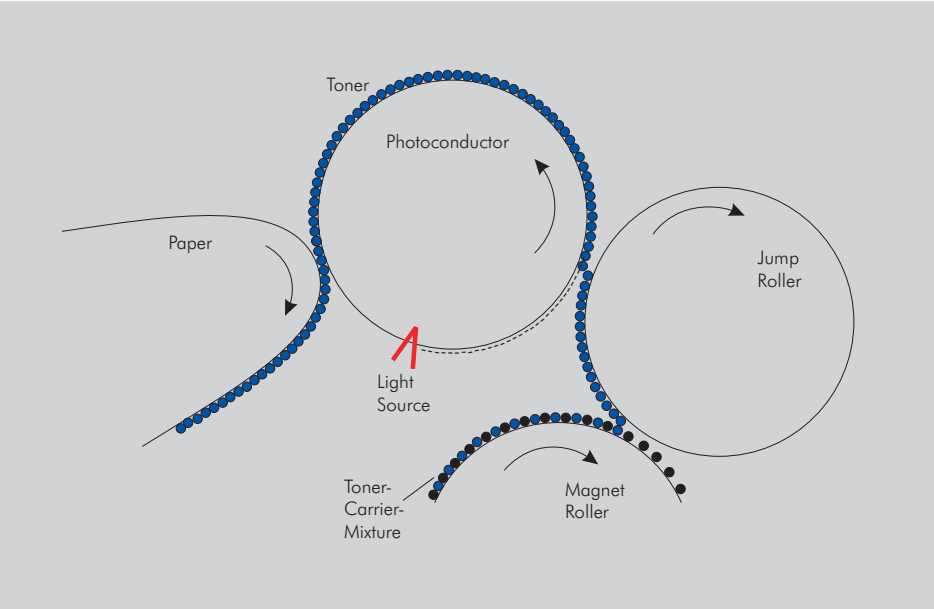

Figure 1.1: Process steps

Some components are being used by all modern electrophotographic printers to ensure a constant high print quality at high print speeds for different print patterns:

- A photoconductor is the core component in the electrophotographic process. It is charged homogeneously and discharged selectively to create the electric fields that will guide the image development afterwards. The photoconductor consists typically of a semiconducting material like As_2Se_3 or amorphous silicon or organic photoconducting materials [Tab69, Sch71].

- A light source (print head) to expose the photoconductor: The first generation of electrophotographic printers used gas lasers ($HeNe$- or Ar-Lasers) that were coupled with an external acusto-optical modulator for this purpose. The disadvantages of this system were the elliptic distortion of the laser beam at the outer edges of the print area and the limited data throughput due to the amount of moving parts. Therefore todays high performance printers use LED technology, where light emitting diodes, mounted on a solid substrate, are arranged in series across the entire width of the photoconductor drum. Each diode addresses one print dot and the spacing between the LEDs correspond exactly to the resolution desired for the printed image [ANCN86].

- Toner, a micron-sized pigmented powder, to mark the latent charge image on the photoconductor. The toner is mixed in a two-component mixture called developer, consisting of toner and carrier. Carriers are spherical or irregularly shaped particles made of magnetic material such as steel, ferrite or magnetite. During the mixing process the toner develops a tribo-electric charge by means of friction. Due to this charge and additional applied voltages, the toner is drawn towards those areas that have been previously discharged

by light - this is also referred to as "discharged area development" (DAD). In other systems, e.g. conventional copiers the areas with high charges are developed ("charged area development")[Gol01].

The process used here consists of three important process steps (see fig. 1.1):

1. The creation of a selective charge pattern on the photoconductor: The photoconductor is charged homogeneously by a charge corona and discharged afterwards by a tightly focused light beam emitted by the print head at the areas that will form the toner image afterwards.

2. The formation of a stable layer of charged toner on an intermediate roller (jump roller): After charging the toner tribo-electrically in the toner-carrier mixture the toner is separated from the carrier by electrostatic forces. The magnetic properties of the carrier are used to form a brush of carrier particles that touches the jump roller, enabling the toner particles to be deposited there.

3. The toner development process where the toner is detached from the jump roller and deposited on the photoconductor: By using alternating electric fields the toner is detached from the jump roller and transported across the jump nip towards the photoconductor. Due to the potential difference between charged and discharged areas on the photoconductor the toner particles are deposited only at those areas of the photoconductor that were previously exposed.

1.2.2 Modeling and Simulation

Several attempts have been made to understand the physical mechanisms of the various processes by creating a mathematical model and subsequent numerical simulation:

- The charging and discharging behavior of various photoconducting materials have been studied for a long time. Models include the charging of a photoconductor by a corona [GFM02, Lea99], the exposure curve (i.e. the relationship between the light and the created charge) [Joh92, JP96], and the spatial and temporal distribution of the created charges [Sch75].

- The triboelectric charging of the toner is a complex process that has been only partly understood. Several models have been proposed, that range from more general considerations about contact electrification [CS97] to more specific models that try to fit the various experimental data [YC97, NST98, CY02].

- A prerequisite for a simulation of toner motion is the understanding of toner-substrate adhesion since this parameter is one of the main influencing factors for the behavior of the system. This is especially difficult since adhesion depends on several factors like the chemical composition and the physical structure of toner and substrate surface, or the charge (and its spatial distribution) of the toner. Much effort has been made to understand the phenomenon by experimental (see chapter 2.4) and modeling studies (see chapter 5.7).

- The toner development simulations that have been done so far range from abstract continuous models [Tom98, KNSA98] to discrete element models of simplified processes [BPÅ99, SR99]. It has been shown, that continuous models can only partly reproduce the effects of the real process. Discrete element simulations seem to have the potential to produce better results, provided that a large number of particles is used and the material properties of the particles correspond to the measurement results.

1.3 Organization of the thesis

Chapter 2 provides an overview of the material properties and the respective measuring methods of toner. Since the toner used here is in powder form, its material properties have to be measured as distributions over a large set of particles. These are essential input parameters for the following process simulation. In addition, some experiments are shown that help to understand the behavior of toner under near process-like conditions. These experimental results are used later to calibrate and verify the simulation results.

For a simulation of the whole deposition process, three process steps as shown in fig. 1.1 have to be included:

Chapter 3 explains the creation of the selective charge pattern on the photoconductor. First, the homogeneous charging by the corona is calculated by finite element calculations. Then the surface potential of the photoconductor after the exposure, that determines the toner deposition in chapter 5, can be calculated from the light pattern, the initial charge density, the exposure curve and the motion of the photoconductor.

Chapter 4 analyzes the process of supplying a stable layer of charged toner for the development process. For modeling the deposition process of toner onto the jump roller, many-body simulations where the carrier particles are following the magnetic fields have been employed as well as a simplified stochastic deposition model to speed up computation time.

Chapter 5 describes the toner deposition on the photoconductor. Finite element methods are used to calculate the electric fields and the air flow in the jump nip. Then, the various forces on toner particles, like particle-field forces, particle-particle forces and particle-surface forces have to be modeled properly so that many-body simulations can be used to describe the complex behavior of a large particle set.

Chapter 6 gives an overview of the soft- and hardware implementation of the various simulation steps. Several commercial and newly developed software packages have to be combined to perform a complete simulation. To improve the computation performance, the main simulation calculations are distributed over a small cluster of processors.

Chapter 7 shows the results from simulations of various applications. The results are compared with the experimental results to assure the correctness of the solution. From the simulations, explanations are deducted for some effects, that were previously only poorly understood. Conclusions are drawn how to improve transfer efficiency and image quality. Some suggestions are made how to further improve modeling accuracy and efficiency.

Chapter 2

Physical properties of the toner

The different characteristic material properties of toner are important parameters for a correct simulation of toner particle motion. Since most of these properties are distributed statistically, measurements with large particle sets have to be carried out to obtain credible results. In addition, the adhesion force measurements, where toner is exposed to various electric fields, deliver valuable insights into the behavior of toner in the real print process. Therefore, these experimental results will be used to verify and refine the simulation result.

2.1 Distribution of toner diameter

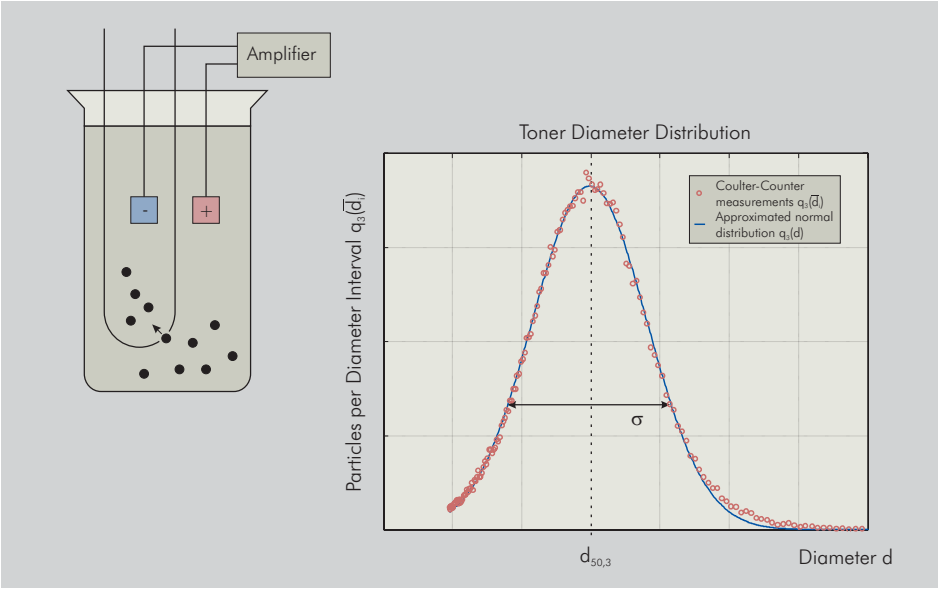

Figure 2.1: Coulter-counter

The typically used toner in standard electrophotographic processes is produced using a melt-grind technology. All the ingredients of the toner are molten, solidified and then ground to the desired particle size. The result of this process is a diameter distribution density

$$q_3\left(\bar{d}_i\right) = \frac{\text{fraction in interval } [d_i, d_{i+1}[}{\text{interval width } (d_{i+1} - d_i)}.$$

The subscript three in q_3 indicates, that the distribution density is measured volume-based, i.e. the third moment of the distribution is taken into account. The result can be approximated

by a normal distribution with the standard deviation σ. The probability density function is [Peu02]

$$q_3(d) = \frac{1}{\sqrt{2\pi}} e^{-\frac{1}{2}\left(\frac{d-d_{50,3}}{\sigma}\right)^2}.$$

To avoid unrealistic negative particle sizes, it is often preferable to use a log-normal distribution by making the transformation $z = \frac{1}{\sigma} \ln \frac{d}{d_{50,3}}$. This is the expected outcome if ratios of equal amount greater than or less than the mean are of equal likelihood rather than differences from the mean [Her60]. In this case the distribution of d is

$$q_3(d) = \frac{1}{d\sigma\sqrt{2\pi}} e^{-\frac{1}{2}\left(\frac{\ln\frac{d}{d_{50,3}}}{\sigma}\right)^2}.$$

The measurement of this distribution was carried out using a Coulter counter. The counter determines the number and size of particles suspended in a conductive liquid by monitoring the electrical current between two electrodes immersed in the conductive liquid on either side of a small aperture, through which a suspension of the particles is forced to flow. As each particle passes through the aperture, it changes the impedance between the electrodes and produces an electrical pulse of short duration, having a magnitude essentially proportional to the particle volume [Hun95]:

$$\Delta R = \frac{4d^3}{1.5\pi D^4} \rho_0 (1 - \rho_0/\rho)$$

where d is the diameter of the particle, D the diameter of the aperture, ρ_0 the density of the liquid and ρ the density of the particle. Using probability calculations, the effect of coincident passages can be taken into account. Thus, the error rate can be limited below 1 %. Figure 2.1 shows the resulting distribution of a measurement of a sample of the used toner.

2.2 Distribution of toner charge

Due to the charge control agents which are among the toner ingredients, intensive friction between toner particles and ferromagnetic carrier particles leads to a triboelectric charge separation. The purpose of the charge control agents is to ensure that the main part of the toner particles receives the same charge polarity. For the toner used here the main polarity is negative. However, the charging process always results also in a significant percentage of so-called opposite polarity toner.

The measurement device to determine the charge distribution is a commercially available toner-charge-spectrometer [KE98]. A developer mixture of toner and carrier is triboelectrically activated using a magnetic stirring unit. The toner particles are then separated from the carrier using a sharp air jet. Thus, the charged toner particles enter the measurement chamber with almost homogeneous velocity, moving freely in the air flow. Two diagonally aligned electrodes cause a perpendicular electrical field which deflects the toner particles until they are deposited on one of the two electrodes. The electrodes are covered with thin removable glass plates which are evaluated afterwards using an optical microscope coupled with an image analysis software, where the diameter and charge of the particles can be derived from their position on the glass plate. The particles are separated by the electrical field depending on their polarity. The higher charged particles are deposited first. The measuring chamber is constructed in such a way that a turbulent air flow is avoided. Collisions between the walls and the particles are largely avoided and there is almost no re-charging of the particles inside the chamber.

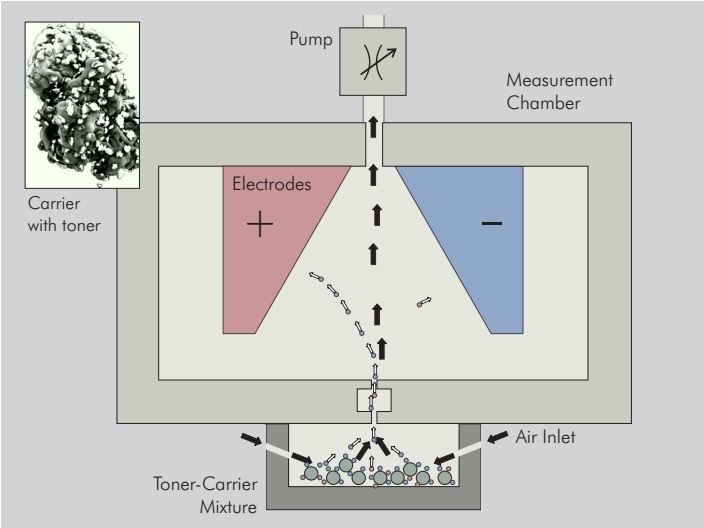

Figure 2.2: Schematic q-test

The results of a fresh mixture of toner and carrier shows that the charge distribution depends on the diameter of the toner particles: The smallest particles show an almost perfect Gaussian distribution which includes almost as many positive as negative particles. For larger diameters an increasing part of correctly charged negative particles appears. Fig. 2.3 shows the charge distributions for different diameter classes. As can be seen from the lower right diagram, an exponential distribution is superimposed on the negative side of the Gaussian distribution.

The complex charging process [SN97, LT98] itself is not part of this work, therefore the charge distribution has been measured several times under reproducible conditions so that together with the diameter distribution, correct initial conditions for the simulation of toner motion are ensured.

2.3 Toner samples for adhesion measurements

One of the most important parameters for any toner simulation is the adhesion force a toner particle experiences near a surface (roller, photoconductor etc.) since this force determines mainly the detachment and the deposition of the particle.

Several methods are available to measure particle adhesion forces (see chapter 2.4). For most of them it is necessary to deposit a toner layer on a sample substrate such that the individual particles are not in contact with each other and therefore no agglomerates can be formed. This ensures that the force which is necessary for detachment is only due to adhesion between toner and substrate, and attractive toner-toner cohesion can be excluded in the experiment.

To create such thin toner layers a device was constructed, where an air flow of a defined duration and flow rate is blown through a measurement cell with a filter. The emitted toner dust is guided by a suitably formed cover towards the substrate. The examinations have shown that the first cloud after activating the air flow contains many clusters of toner particles. Therefore, the substrate is put in place several seconds after the air flow has been started as shown in fig. 2.4.

For specific cohesion measurements samples have to be created where several toner layers are on top of each other. For charged toner the electrical properties of the toner can be used to guide the toner towards the substrate by applying a voltage to the substrate, so that almost 100 % of the emitted toner from the measurement cell reaches the substrate. To charge the

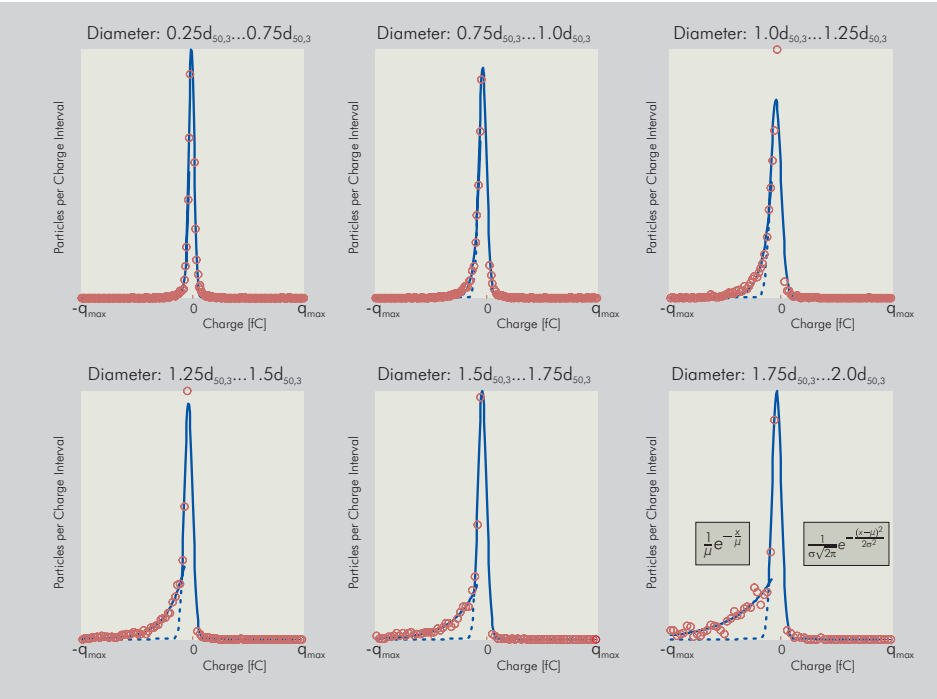

Figure 2.3: Charge distribution in the developer mixture

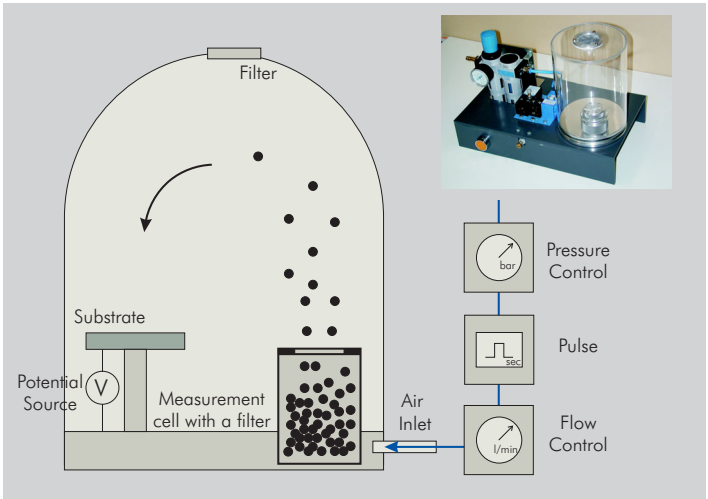

Figure 2.4: Setup for toner deposition

toner the measurement cell is filled with a previously activated mixture of carrier and toner particles.

By adjusting the flow rate with time controlled valves, the steadiness regarding the particle density and the quantity of particles of the created layers can be improved. This reproducibility of the starting conditions is vital to compare the results of several adhesion force measurements.

The jump experiments (see chapter 2.5) with the thus created charged toner layers showed that fiber filter must not be used as a filter in the cover of the setup since fine fibers are deposited together with the toner particles. These fibers create peak fields during the jump process which lead to disturbances of the toner deposition (see fig. 2.5, toner particles are deposited mainly along the fibers due to the high electric peak fields).

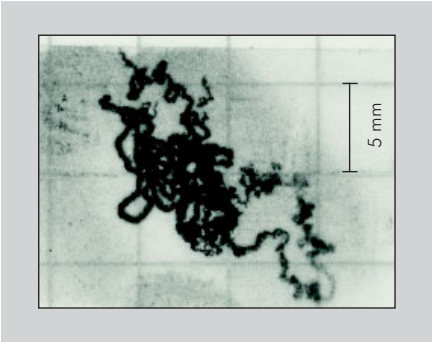

Figure 2.5: Jump experiment with fibers in the toner layer

Different procedures have to be found for the deposition of thin and thick layers to receive suitable reproducible results.

2.3.1 Thin layers of toner

The deposition of a thin layer is necessary to exclude the interaction of toner particles as described above and to determine the diameter distribution by using an optical microscope and an image analysis software.

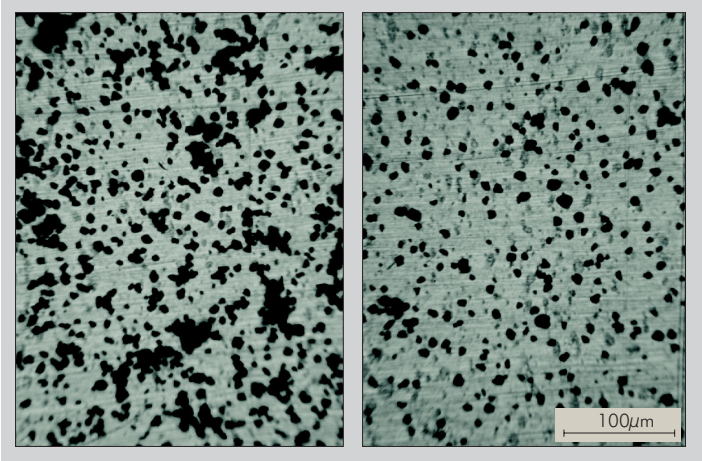

Figure 2.6: Toner layer with high/low number of agglomerates

Since toner is charged by friction with carrier particles triboelectrically, a mixture of 5-8

percent of toner and the appropriate amount of carrier is put into a bottle so that the toner can be charged by rotating the bottle. To separate the toner from the carrier afterwards, the screen of the measurement cell has a screen size which the toner can pass, while the far bigger carrier is kept back.

The problem of clustering arises less often than with uncharged toner, due to the repelling force of the electrical charges that outweigh the short-ranging cohesion forces. Therefore, it is sufficient to fill a measure spoon of developer mixture in the measurement cell and blow an air flow through the cell with full pressure for 10 seconds .

The right image in fig 2.6 shows a thus created layer. The diameter distribution is almost identical to the one from the Coulter counter and shows only a few clusters.

The creation of an uncharged layer is more difficult, since no electric force keeps the particles from clustering. There are two possible ways: Either to use the deposition device with the measurement cell filtered with uncharged toner. Experiments have shown that most clusters are in the first cloud after pressure is switched on. So the amount of clusters can be reduced by placing the substrate on the ground plate some seconds after the pressure was initiated. Another way is to deposit a thin layer of charged toner as described above and to discharge the toner after the deposition by an AC corona. Since the corona creates charged ions of both polarities, the ions will tend towards the charged toner, thus discharging it. A problem with this approach is, that it is difficult to ensure that all charges on the toner have been neutralized.

2.3.2 Thick layers of toner

To study the interactions between toner particles, layers of up to 5 or 6 toner levels (respective 20 to 30 μm) are required, as they are also obtained in the real printing process on the jump roller. Precision scales can be used to quantify layers of this thickness: The desired thickness corresponds to a toner cover of about 2 mg/cm^2.

A problem with producing this type of layer is that there is no possibility to guide uncharged toner explicitly on the substrate. Experiments to place the substrate directly above the measurement cell failed because of the high flow rate which influences the homogeneity of the created layer. The substrate has to be placed as shown in figure 2.4, outside of the direct air flow with a minimum distance from the measurement cell of 5-8 cm. To influence the emitted toner cloud as little as possible, the cover of the setup needs a minimum distance from the measurement cell (20-30 cm), as well as a preferably uniform curvature. However, as a consequence of this setup, not only the substrate is covered very homogeneously with toner but also the whole rest of the inside of the setup. Therefore, the setup has to be cleaned intensively after the deposition of a thick uncharged toner layer.

Creating a thick layer of charged toner is much easier, since its charge can be used to draw the toner towards the substrate by applying an electric voltage.

2.4 Measurements of toner adhesion force

For a quick approximation of the adhesion, sometimes the tape measurement is used [BD96], where a tape strip is applied to the sample for a specified time under a certain pressure. After removing the tape, the amount of detached toner can be quantified by measuring the optical density. For a more precise measurement of the adhesion force, three methods are commonly used:

- Centrifuge measurements [MOEH00]: Toner is detached using the accelerating force created by an ultracentrifuge. The remaining toner is measured by an image analysis software.

- Atomic force microscope (AFM) measurements [GSR96]: A single toner particle is fixed to an AFM cantilever, so that the adhesion force between the particle and a substrate can be measured repeatedly for different positions and different substrates.
- Electrostatic detachment measurements [RF01]: Charged toner can be detached from a substrate using electric field forces. This allows to quantify the influence of the toner charge.

These approaches complement one another: The centrifuge measurement has the advantage that large quantities of particles can be measured simultaneously, which is important since the adhesion forces differ widely (up to three orders of magnitude) between individual particles. In contrast, the AFM method uses only single particles so that the measurement of an adhesion distribution is very time-consuming. However it can be used easily to measure the adhesion force of the same particle at different positions on a substrate and to compare the adhesion forces for different substrates. Also, the AFM method is the best way to measure toner-toner and toner-carrier forces. The third method, the electrostatic detachment measurements can only be used for charged particles. It offers the possibility of measuring the relation between charge and adhesion force by recording simultaneously the electric current and the number of detached particles. The experimental effort is high however, since the necessary electric fields to detach all particles can only be attained in an evacuated experimental setup.

Several studies have been done to compare the results from the various methods [FT98, Hay95, GSR96]. It could be shown, that the results are comparable within the accuracy of measurement as long as the conditions have been set up properly.

2.4.1 Centrifuge measurements

The procedure for the centrifuge measurement is straightforward and has been long used before [FT98]: A sample substrate with a previously deposited thin toner layer (see chapter 2.3.1) is accelerated in a centrifuge at different rotation speeds. To do so, a rubber inlay was constructed which enables the insertion of the substrate parallel to the rotation axis by using common test tubes. After each speed level, the remaining toner on the substrate is evaluated and classified according to its diameter distribution using an image analysis algorithm. Another way is to collect the detached toner on a glass plate which can be evaluated much easier due to the higher contrast by the image analysis unit. Unfortunately, this is only possible for low rotation speeds where only the less adhering particles are detached. It cannot be used in ultracentrifuges because the high acceleration forces (up to 700.000 g) could lead to the destruction of the glass. The resulting out-of-balance of the centrifuge rotor at high rotation speeds could lead to the destruction of the centrifuge.

The effective detachment force can be calculated from the angular frequency ω, the radius R of the rotor and the toner mass m [RQ02]

$$F_{detach} = m\omega^2 R > F_{adhesion}$$

This equation shows one of the disadvantages of centrifuge measurements: If the number of speed steps is too low only rough approximations can be given for the adhesion force. Another problem is the sample preparation: If toner particles are deposited on the substrate as agglomerates, a much higher centrifugal force is in effect due to the higher mass of the agglomerate leading to a wrong adhesion force distribution. These requirements lead to time-consuming series of measurements.

Fig. 2.8 shows the results from such a series of measurements [Her02]: First, a substrate was prepared with a set of charged toner particles, which were detached in a series of 25 speed steps.

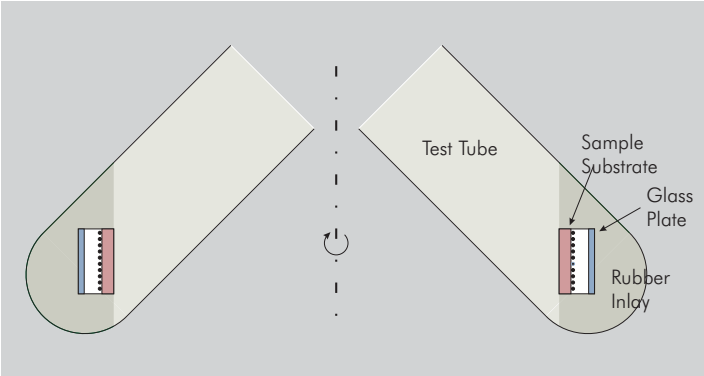

Figure 2.7: Setup for centrifuge measurements

Unfortunately, even the highest acceleration forces are not sufficient to detach all particles, especially the smaller ones (up to 20 % of the smallest particles remain on the substrate), due to their low mass. Neglecting these remaining particles in the summary would falsify the results. So the forces from these particles were estimated such that the force distribution for each diameter class is approximately Gaussian. The resulting relation between the adhesion force $F_{50\%}$ where 50 % of the particles of one diameter class are detached and the diameter is approximately linear (correlation coefficient $r = 0.994$) which concurs with the theory of Johnson, Kendall and Roberts [JKR71].

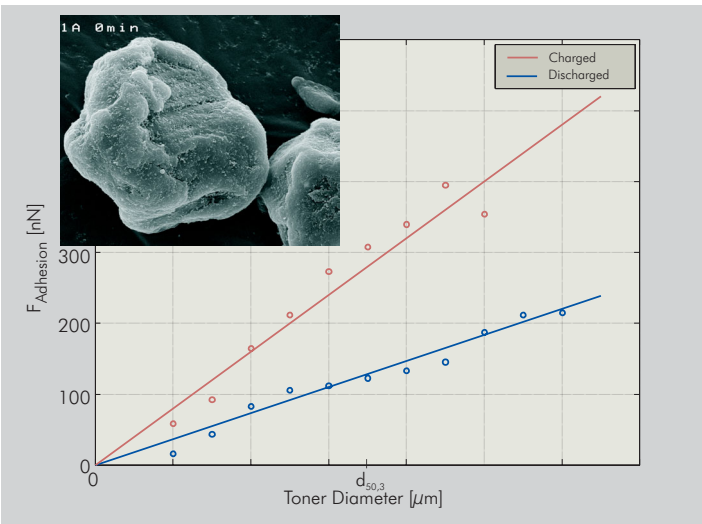

Figure 2.8: Results from centrifuge measurement (SEM micrograph of toner with silica additives)

Preparing a sample substrate of uncharged toner proved to be difficult due to the still high amount of agglomerates deposited. Therefore a substrate with charged toner was prepared and put in a climate chamber (20°C, 80 % r.h.) for one week. From previous experiments it is known that toner should be sufficiently discharged after that treatment. In a second experiment, the toner was discharged, using a high-voltage AC corona as described in chapter 4.1. The results from the adhesion measurements with the thus discharged toner were comparable to the ones from the toner in the climatic chamber. The diameter-force curve for discharged toner is also linear but the absolute force values are only about 40 % compared to the charged particles (see

fig. 2.8).

2.4.2 AFM measurements

Another way of measuring the adhesion force of toner particles on surfaces is the use of an atomic force microscope (AFM) [PGM02, GP03]. An AFM always measures only a single particle, so it is difficult to create a force statistic for a large particle set. The main advantage is that the variance of the adhesion force for a single particle at different positions on a substrate can be measured as well as the difference between several substrates. Using appropriate techniques it should also be possible to measure the distance dependency of the adhesion force.

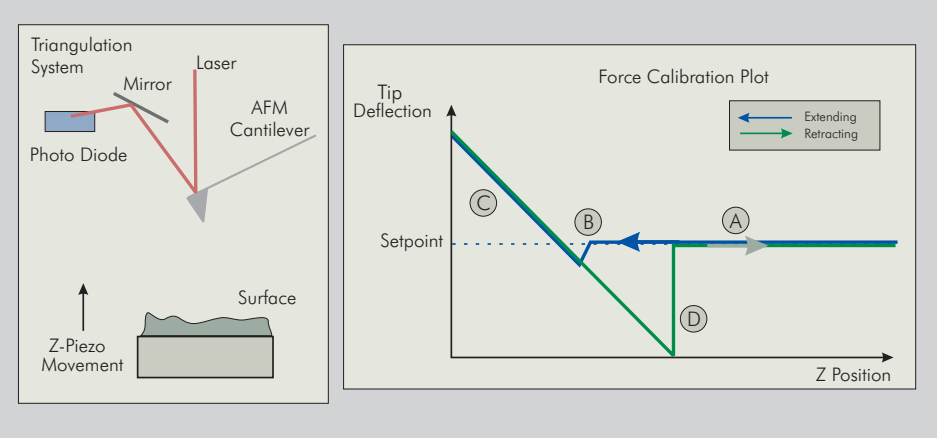

Figure 2.9: AFM principle

The basic functionality of an AFM is shown in figure 2.9: A small probe tip, which is attached to a cantilever spring, is brought down towards a sample surface (A). The elevation of the cantilever can be detected by using a laser triangulation system. When the distance between tip and surface is small enough so that van-der-Waals-forces become dominant, the tip jumps to the substrate (B). After that point a further motion of the substrate in z-direction results in a curve of constant rise in the force-position diagram (C), which represents the spring constant of the cantilever. When retracting the substrate, it can be observe that the point where the probe is detached from the surface (D) is different from the point where it jumped in initially. The distance between these two points multiplied by the spring constant of the cantilever is the adhesion force detaining the release of the probe [BCP92].

To measure the adhesion force of toner on a sample substrate, the AFM cantilever has to be prepared so that a single toner particle is fixed firmly on the tip of the cantilever. To achieve this, a small amount of toner dust is dispersed on a glass plate, which is then placed in a light microscope. The cantilever is then dipped slightly into quick-setting glue so that a very small drop of glue sticks to the cantilever. With the help of the microscope, the thus prepared cantilever is then positioned above an isolated toner particle, lowered down and lifted up again. When the toner particle cannot be seen any longer in the microscope it has to be removed from the focal plane and therefore has to stick to the cantilever. A scanning electron microscope (SEM) image can be used to find out whether the toner particle is covered with glue, which would be fatal since the measured adhesion value would be dominated by the glue.

The main use of the AFM method for the toner simulations of this work were the measurements of toner-toner cohesion and toner-carrier adhesion. Instead of the sample substrate described above a thick layer of toner (see chapter 2.3.2) or carrier particles was used. These

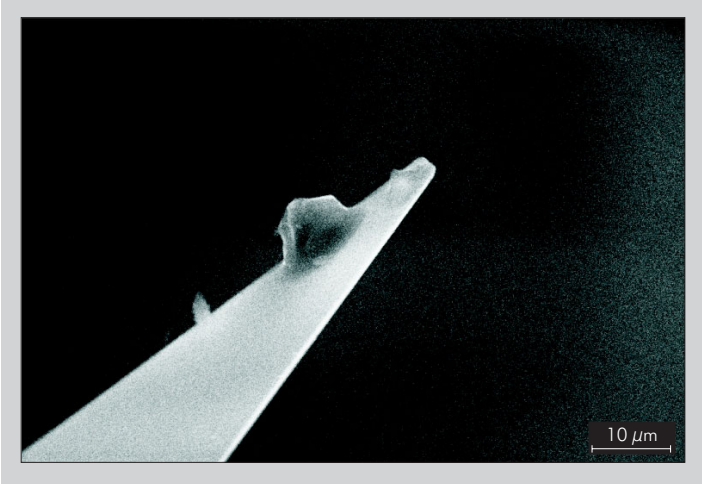

Figure 2.10: Toner on AFM cantilever (SEM image)

measurements can only be done by an AFM since a centrifuge would destroy the thick layer of toner or carrier.

2.5 Toner motion under the influence of electric fields

2.5.1 Setup for electric field detachment experiments

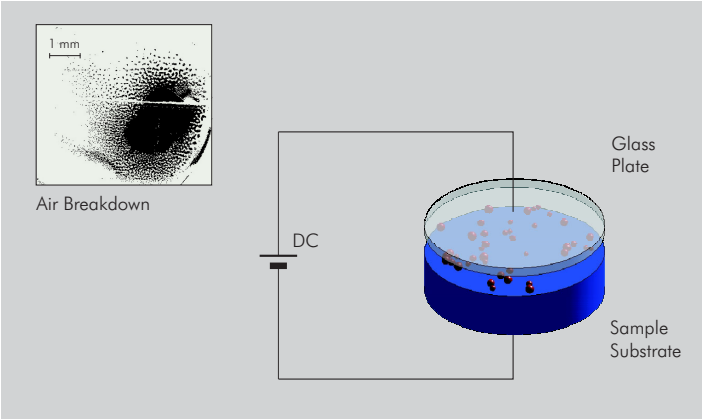

Figure 2.11: Toner jump experiments with parallel plates

As the centrifuge measurements showed, the adhesion force of charged toner is much higher compared to uncharged toner, due to the mirror forces of induced charges. However, its charge can be used to measure its adhesion force by detaching it using electrical fields [FT99]: A DC voltage is applied to a sample substrate and a parallel counter electrode. As with the centrifuge experiments, the detached toner particles are collected on glass plates and classified by their diameters.

However, this setup has significant disadvantages: If the two plates are not adjusted exactly parallel, the higher fields at the narrowest spot lead to air breakdown. This problem can only be solved with high mechanical adjustment effort. Therefore, a series of measurements with many

experiments can be very time consuming. The alternative of evacuating the whole setup leads to even more time consuming experiments.

The small image in figure 2.11 shows the result of an experiment where an air breakdown occurred. The breakdown is clearly audible during the jump process. Furthermore, the jumped toner shows a distinct concentration in one spot surrounded by smaller round toner agglomerates, which is a characteristic result for air breakdowns.

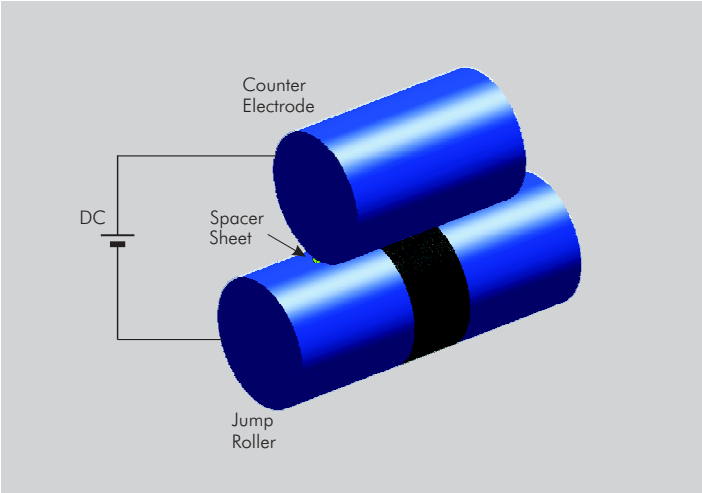

Figure 2.12: Toner jump experiments with resting rollers

To avoid this problem and to reduce the necessary time per measurement, a different setup had to be developed (see fig. 2.12): A rotating roller (jump roller) was covered completely with a homogeneous toner layer using the developer station of the printer. Then the roller was stopped and the toner was removed from the roller except from a small strip along its circumference. A second roller was adjusted axially to the first roller, using spacer sheets to calibrate the distance. This roller substitutes the photoconductor in the real print process. The spacer sheets had to be placed outside of the toner strip so the layer thickness cannot influence the total distance. This way an exact adjustment is only necessary in one dimension. However the whole experiment had to be carried out very carefully since even small dust particles or fibers can cause peak fields and lead to air breakdowns.

This setup has another huge advantage: Since the geometric boundary conditions are comparable to the real printing process, experiments can be performed where not only the toner detachment is studied but the whole process of detachment, motion and deposition under the influence of different voltage forms. However, due to the fact, that the rollers are not rotating compared to the real process, the number of influencing effects is reduced, so that it is easier to identify relations between variations of input variables and the resulting behavior.

2.5.2 DC voltage experiments

In a first series of measurements only a DC voltage was applied to the two rollers. The reason for this approach was that a simple constant voltage should produce results both easier to interpret and to simulate. Several effects could be observed (Fig. 2.13):

- The toner on the counter electrode formed only a diffused strip, not a clearly distinguishable domain.

- The width of the strip on the counter electrode was about the same as the strip on the jump roller where toner was missing.
- Only a small percentage of the toner amount was transferred, so that the missing strip on the jump roller cannot be perceived easily.
- Even with voltages where small air breakdowns are audible a significant amount of toner remains on the jump roller. This is especially remarkable since the resulting fields from the constant DC voltage here are higher than with the AC-DC voltage combination used in the printing process [Taj83], where a much higher percentage of the toner is transferred. It can be concluded that the electrostatic force due to the occurring fields is not sufficient for detaching all the toner.

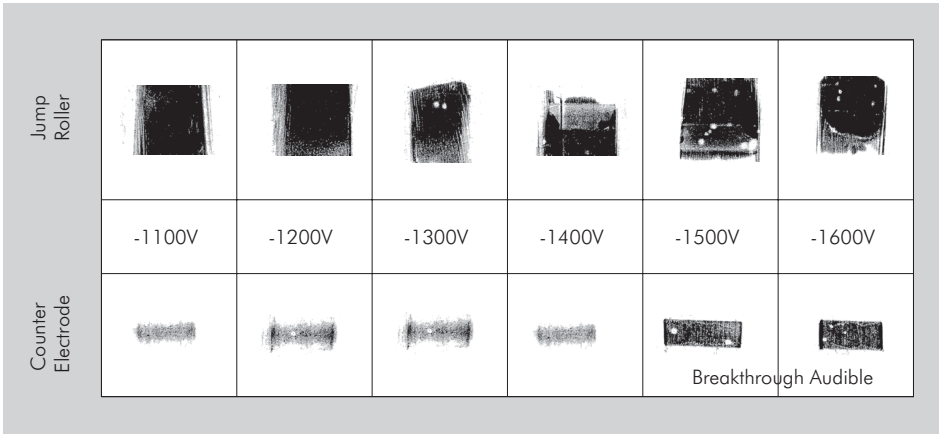

Figure 2.13: DC voltage variation

For a quantification of the amount of toner transferred with the DC voltage, the thickness of the transferred strip was measured, as well as the thickness of the original toner layer and the thickness of the missing part. This was performed using the white-light interference phenomenon [Jak98]:

White light is transmitted to a sensor head via fiber and is then focused onto the object to be measured. Because of a strong chromatic aberration of the light emitted from the measuring head, the focal length varies significantly with wavelength. As soon as the focus corresponding to one specific wavelength is on the object's surface, the light reflected to the measuring head and recoupled into the fiber has a maximum at this wavelength. The spectrum of the reflected light, which is evaluated in the control unit, shows a narrow peak. From the peak position, the distance to the object is calculated.

Figure 2.14 shows the results: The two upper diagrams show the thickness of the removed toner layer compared to the deposited strip. The thickness is around 8 μm in both diagrams indicating that the transferred toner consists of a single particle layer. The lower diagram on the left side displays the results of a thickness measurement at the edge of the original toner layer before the experiment, compared to the blank roller. The result of more than 20 μm means that only about one third of the original layer was transferred. Not only the particles directly attached to the roller remained there, but also the particle layer on top of them, whereas only the uppermost particle layer jumped to the counter electrode.

The measurements themselves, as well as the analysis of its results, were difficult to perform: The lower diagram on the right shows the raw measurement data from the sensor. The main characteristic measured is the curvature of the roller whose elevation is far greater than the toner

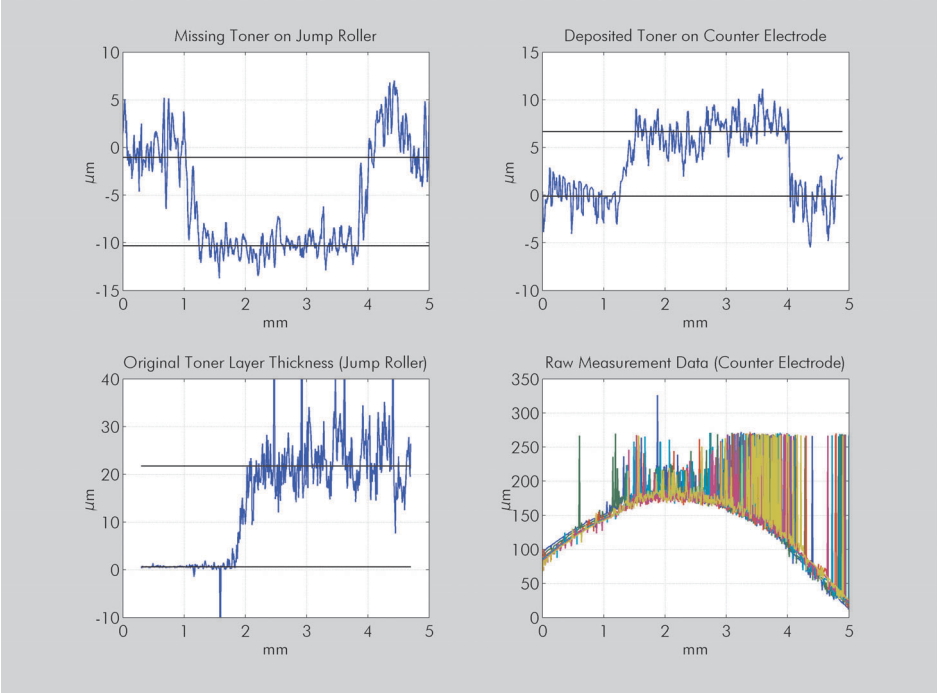

Figure 2.14: DC voltage toner layer thickness measurements

layer thickness. Also, the totally different reflection characteristic of the toner layer and the aluminum roller produced highly unstable results, which had to be stabilized by careful filtering and redundant measurements.

To compare the results of a numerical simulation with results from the experiment, it is important to know not only the average thickness of the deposited toner strip, but also the typical configuration of the individual toner particles. For this purpose, the counter electrode was covered with a thin aluminum foil before the experiment was conducted again. Care had to be taken that the foil was as smooth as possible so that no sparks would be produced at small spikes. After the experiment, the foil with the deposited toner could be taken off the roller and examined both in an optical microscope (fig. 2.15, right) and in a scanning electron microscope (fig. 2.15, left).

The microscope reveals that the toner particles are deposited mostly isolated, as well as in small agglomerates of two to five particles. Some areas are not covered with toner at all, so the layer is not complete as could be expected from visual inspection. The agglomerates were observed in the SEM to examine their spatial layout. In several cases agglomerates were found where one particle was lying on top of the others as indicated in the figure.

2.5.3 AC voltage experiments

Next, an AC voltage ($U = \pm 1000V$, $f = 2.7kHz$) without a DC voltage component was applied to the two rollers for several seconds, meaning many thousand periods. The result is much more complex than with the DC voltage experiment before (fig. 2.16):

1. Two dense toner bars are deposited on the counter electrode. Between them only a small amount of isolated toner particles can be found.

2. The jump roller is still covered with toner, but there are two lines visible where almost all the toner was detached. Between these lines the toner seems to be less uniformly

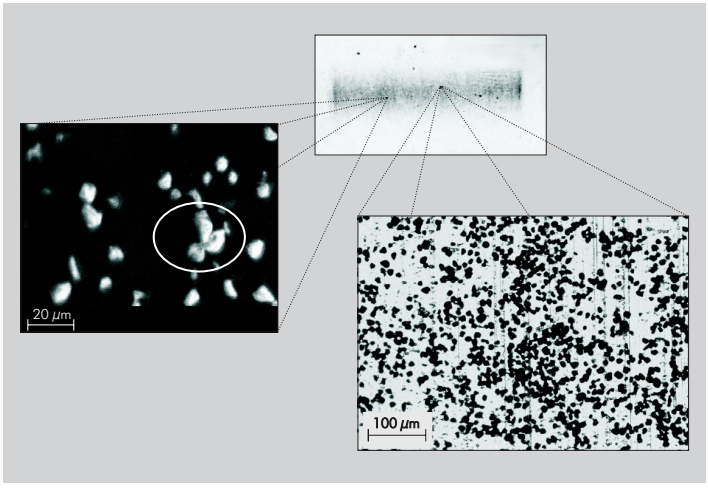

Figure 2.15: DC voltage toner layer characteristic

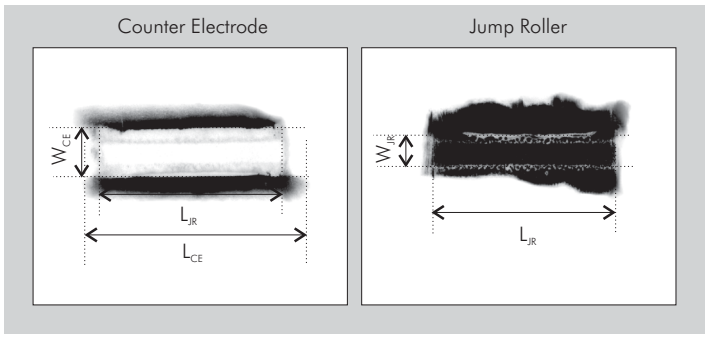

Figure 2.16: Result of AC voltage experiment

distributed than before the experiment.

3. The bars on the counter electrode are larger than the original strip on the jump roller ($L_{CE} > L_{JR}$) .
4. The distance between the bars on the counter electrode W_{CE} is larger than the distance between the two lines on the jump roller W_{JR} ($W_{CE} > W_{JR}$) .
5. The total amount of transferred toner is much higher than with the DC voltage, although the resulting fields were lower and there was no driving field towards the counter electrode.

These results shall be explained step by step:

1. Forming of two bars The explanation for this result could be that toner is detached from the jump roller near the narrowest gap and then bounces up and down, following the alternating electric fields. Due to the curved surface of the rollers, the electric field lines between them are bent outwards, so that the particles experience an additional force moving them away from the center. As they are moving outwards, the electric fields get weaker. At some point, where the adhesion and mirror forces hold the toner down, they are no longer sufficient to draw the toner back from the surface.

To validate this suggestion, another experiment is carried out: This time the AC voltage is created using a waveform generator, where the AC voltage can be stopped after a predefined number of periods and at a specified phase.

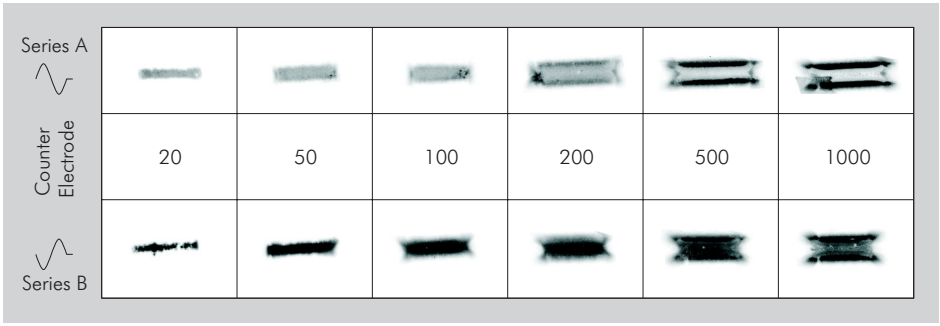

Figure 2.17: AC voltage experiment with fixed number of periods

Fig. 2.17 shows the results on the counter electrode:

- With an increasing number of AC periods, more toner is deposited further away from the center, eventually forming the two bars observed before.
- There is a distinctive difference between series A and B in fig. 2.17 depending on the half cycle with which the AC voltage stops. Series B shows the result of an AC voltage which ends with a half cycle where the electric field is directed towards the counter electrode. The amount of toner deposited is noticeably larger than in series A, especially between the two bars.

This means that the assumption of toner moving outwards with an increasing number of AC periods can be confirmed. Furthermore, the direction of the last half-cycle determines whether the toner which is still moving in the air gap is deposited on the counter electrode or back on the jump roller. So the comparison of the toner deposition of the two series of this experiment can be used to estimate the ratio of toner already deposited firmly on the counter electrode (series A) and the toner still moving in the air gap (difference between series A and B).

2. Large bars on the counter electrode As can be seen in fig. 2.16, the bars on the counter electrode are larger than the original toner strip on the jump roller was ($L_{CE} > L_{JR}$). The most obvious explanation for this behavior is the repulsion of the equally charged toner particles when they move freely in the air gap. This can be confirmed by the fact that the enlargement to grows in fig. 2.17 the longer the AC voltage was applied.

3. Large amount of transferred toner Comparing fig. 2.13 and fig. 2.16, it becomes clear that an AC voltage with a moderate peak voltage can transfer much more toner to the counter electrode than a DC voltage even at the air breakdown limit. So the transfer process in the AC voltage case has to be fundamentally different than in the DC voltage case. To find out more about this mechanism, the following experiment was performed: First a DC voltage of $-1200V$ was applied. The transferred toner (shown in the left column in fig. 2.18, experiments 1a and 2a) was cleaned from the counter electrode, and then the electrode was placed opposite the jump roller again at the same position as before. Now an AC voltage was applied to that toner which was not transferred by the DC voltage before. The result is shown in the middle column in fig. 2.18. For comparison, the same AC voltage was also applied to a fresh toner strip (experiments 1b and 2b).

Looking at the first series there is a clear difference between the toner that jumped due to the AC voltage of $\pm 500V$ which had seen the DC voltage of $-1200V$ before, and that which had not. The AC voltage after the DC voltage could detach only very few toner particles. Also, the sum of toner from the DC voltage and the AC voltage seems to be far smaller than the fresh toner only detached by the AC voltage.

An explanation could be that on top of a fresh toner strip there is one particle layer which is for some reason easier to detach than the layers below. This particle layer is transferred in the DC voltage experiments. In an AC voltage experiment these particles are also detached at first, but due to the alternating fields they are always rebouncing on the rest of the toner strip where the mechanical impact helps to detach other particles. So when these initially detached particles were removed by the DC voltage in this experiment, they are no longer available to start the transfer process with the AC voltage afterwards.

This can be shown very impressively in the results from Experiment 2a with $\pm 600V$ AC voltage: Due to some slightly inaccurate positioning of the counter electrode during the DC voltage part the left side of the electrode was a bit further away. This caused fewer particles to be detached by the DC voltage on that side. In the AC voltage part afterwards, where the positioning was correct again, the redundant particles on the left side which couldn't be detached before were now able to start detaching far more other particles compared to the right side.

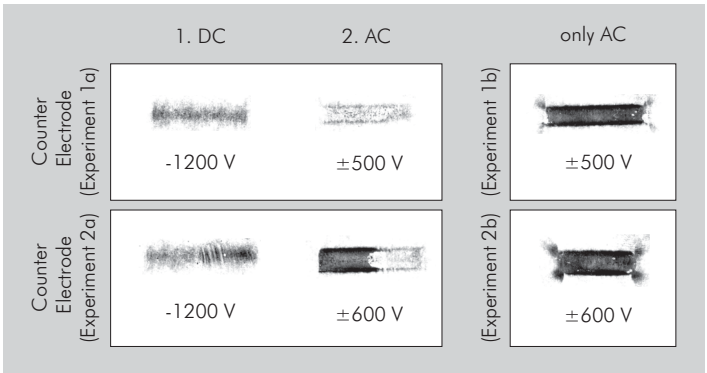

Figure 2.18: Experiment with AC voltage following DC voltage

2.5.4 AC-DC voltage experiments

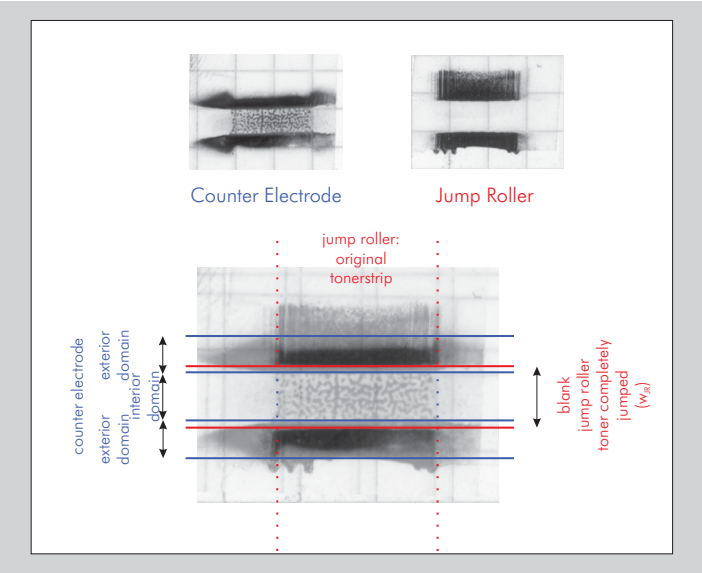

Figure 2.19: Typical result for jump experiment with AC-DC voltage

Now combinations between AC and DC voltage were tested: Figure 2.19 shows the results from the counter electrode and the jump roller as well as an enlarged superposition of the two pictures to compare their dimensions. The toner strip on the jump roller is completely removed in one zone where the roller is clearly shiny. The boundaries of this zone look precisely confined and almost parallel. The toner on the counter electrode is deposited in three different domains. The two exterior domains are the two broad black bars already observed in the AC voltage experiment above, which start a bit more inward than the end of the corresponding strip on the jump roller. As noticed before, their axial extension is far broader than the original toner strip on the jump roller. Between these bars, there is an interior domain which is characterized by a very inhomogeneous toner cover. The enlargement shows a distribution of large toner agglomerates. Whether these lump together during the jump process, or if they are detached as a whole is not clear. But it can be shown later on that short-range attractive forces between toner particles play an important role in the creation and the size of these clusters. When these clusters move in the air gap, their large mass prevents them from following the quickly alternating AC voltage. They are just drifting along, following the DC voltage component to the other side. This seems to be the reason why they are not accumulated in the exterior bars like the smaller agglomerates or the single particles.

Several series of measurements were performed to improve the understanding of the transfer mechanism:

1. Constant AC voltage with different DC voltages One series of measurements was set up with a constant AC voltage of ±1000 V and a variation of the DC voltage. The following results can be observed:

- The two toner bars on the counter electrode are deposited even when the DC voltage is pointing towards the jump roller (positive sign).
- For a positive DC voltage, the picture on the jump roller shows two spikes to the left and to the right. These are the ends of two bars similar to those on the counter electrode

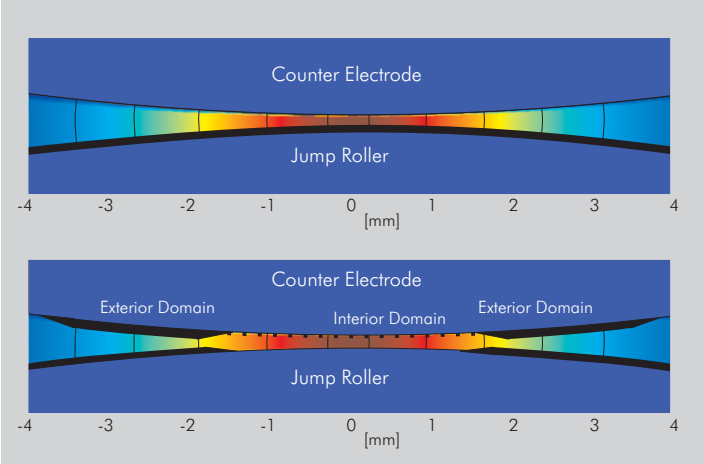

Figure 2.20: Transverse profile before/after jump process (schematically)

which cannot be seen clearly due to the rest of the original toner strip. This would mean that the toner particles which are detached are deposited both on the counter electrode and on the jump roller when they have jumped far enough. The amount of the DC voltage varies the ratio between the two depositions.

- For small positive and for negative DC voltage values, toner is also deposited in the interior domain between the two toner bars

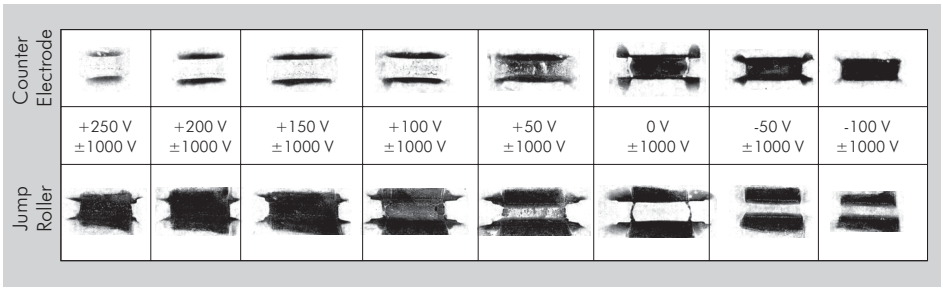

Figure 2.21: DC voltage variation with constant AC voltage

2. Constant DC voltage with different AC voltages For the next measurements, the DC voltage was held at a constant level of -300 V while the AC voltage was varied. The patterns on the counter electrode did not vary qualitatively, but the two black bars moved outwards with rising AC voltage, so that the interior domain got wider. This can be easily explained with the higher fields due to the higher voltages: A certain level of field strength has to be undershot so that the toner can be deposited. For higher voltages this level of field strength moves outwards to wider air gaps.

Additionally, the type of the AC voltage was varied: Before, all the experiments were carried out using a sine-wave voltage. Now a second series was done with a square-wave voltage [Taj83]. The resulting patterns were again qualitatively the same, but the square-wave AC voltage was able to detach toner much more efficiently than the sine-wave (see fig. 2.22 left). The distance between the black toner bars was much broader and the toner bars themselves looked darker. The reason for this behavior could be that the integral of the accelerating force during one

half-cycle is higher for a square-formed AC than for a sine-formed. This results in a higher velocity when a detached toner particle bounces back on the original toner layer so that there is a higher probability of detaching other particles.

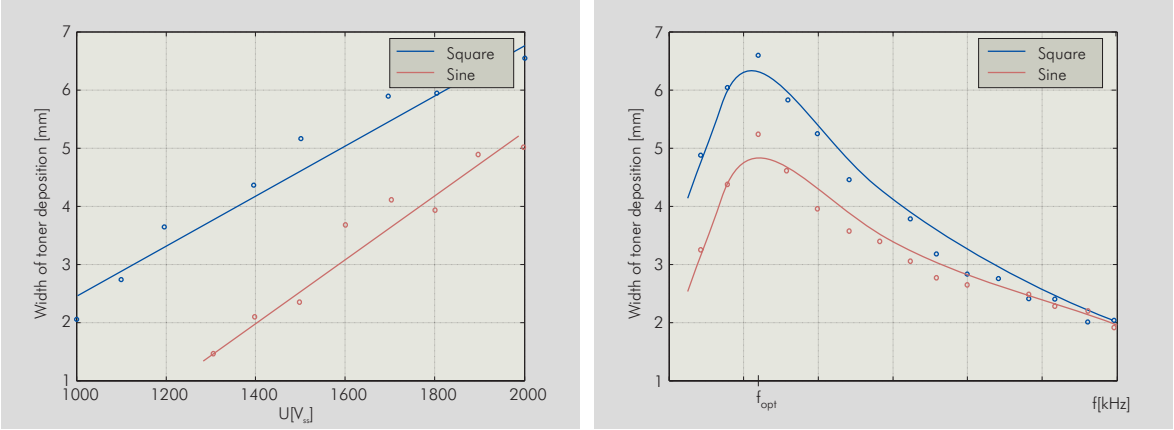

Figure 2.22: Variation of voltage magnitude and frequency

3. AC voltage with different frequencies It is known from the printing process that another important parameter for the transfer efficiency is the frequency of the applied AC voltage. This was examined in the next series of measurements. The resulting patterns were qualitatively comparable but the amount of toner transferred varies drastically with the frequency. This is once again measured using the distance between the two toner bars on the counter electrode. Fig. 2.22 right, shows that there is a clear maximum with a sharp decline towards higher and lower frequencies. The explanation (see chapter 7.2.2) is that there are not enough impacts of the initial particles with the rest of the toner strip for frequencies below f_{opt}. For higher frequencies, the mechanical width of the air gap seems to be too large so that with the shorter periods the particles do not always bounce back and forth, thus also reducing the number of impacts with the rest of the toner layer. As before, the square-wave AC voltage detaches more toner than the sine-wave.

4. Thickness variation of the original toner strip As before in the DC voltage case, the thickness of the original toner strip was varied. This was especially interesting since it was shown above, that a small amount of loosely bound toner particles is necessary to start the detachment of the rest. The image on the counter electrode (fig. 2.23) shows no significant changes, i.e. the three domains are still clearly distinguishable, even at a thickness of only 7μm. This means that the few initial particles are able to detach other particles even if these lie directly on the jump roller. Another observation is that with lower toner thicknesses the interior domain on the counter electrode seems to be more homogeneously covered with toner so that less agglomerates are visible. This indicates that the agglomerates found at higher thicknesses are detached from the jump roller and do not form in the air gap.

2.5.5 Summary

The various jump experiments showed a characteristic behavior of toner under the influence of an electric field:

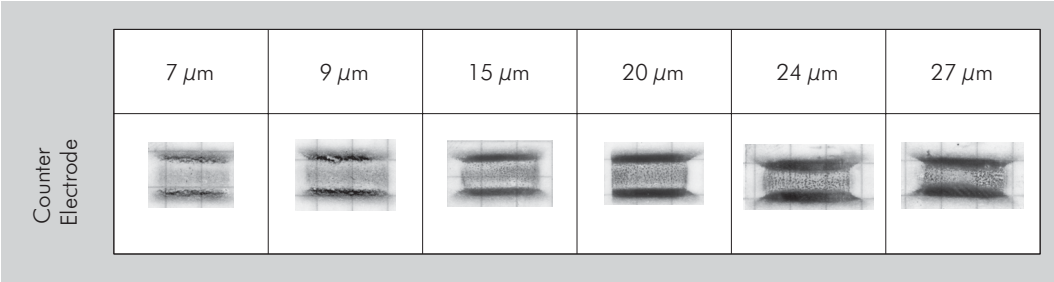

Figure 2.23: AC-DC voltage experiment with thickness variation

- A DC voltage can only transfer about a third of a thick toner layer even if the resulting electric fields are near the air breakdown limit.
- To transfer a thick toner layer completely an AC voltage is needed. The mechanism seems to be that some particles are only loosely bound so that they can be detached more easily. Under the influence of an AC field, these particles are jumping up and down in the nip, thus bouncing against the remaining particles and mechanically aiding in detaching them.
- Single particles detached by an AC voltage will only be deposited when they have moved away from the center of the nip so that the electric fields become weaker.

These characteristics delivered some very valuable insights in the physical mechanisms of the jumping process and will be used in chapter 7 to test the many-body simulation for correctness.

Chapter 3

Charging and exposure of the photoconductor

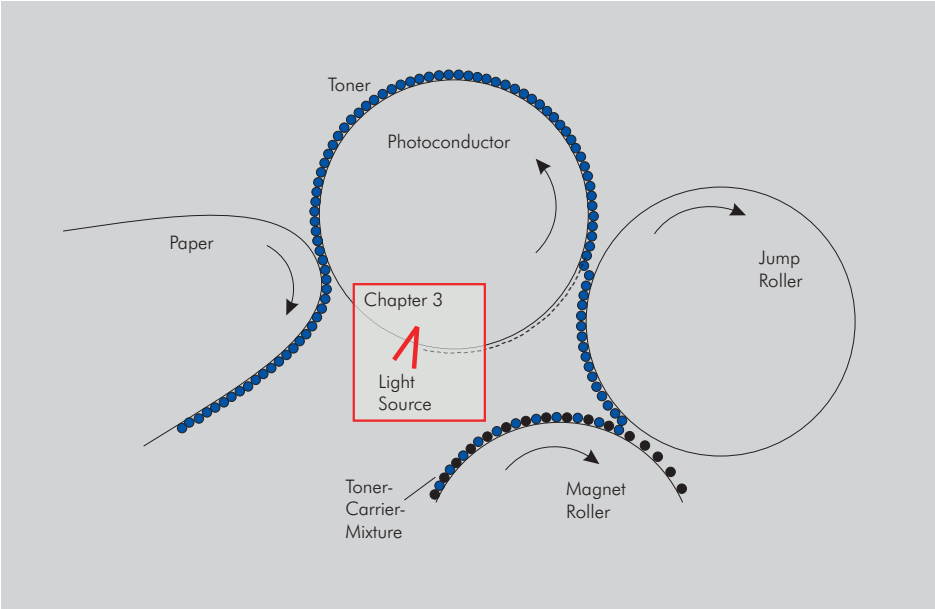

Figure 3.1: Process steps

Toner deposition in an electrophotographic printing process is essentially controlled by electric fields attracting the toner towards the image and repulsing it from the background areas. These electric fields are created by a selective latent charge pattern on the photoconductor. This charge pattern results from charging the photoconductor uniformly with high-voltage corona wires and discharging it afterwards selectively with an appropriately designed light source.

To calculate an exact field distribution, the corona charging process has to be taken into account, as well as the light from the LED print head and the appropriate exposure curve of the photoconductor. Figure 3.2 shows a complex print pattern, where the light energy of the LED print head discharged the uniformly charged photoconductor as described in chapter 3.2. Due to the Gaussian light form of the LEDs, a significant ripple can be observed in the resulting charge distribution. The potential distribution created by the charge distribution, however, has a significantly reduced fluctuation because of the integrating effect. Nevertheless the resulting electric field will be less homogeneous than the one resulting from a uniform light source. This effect becomes even more obvious if the LEDs are not operated with maximum power, so that

the photoconductor is only partly discharged.

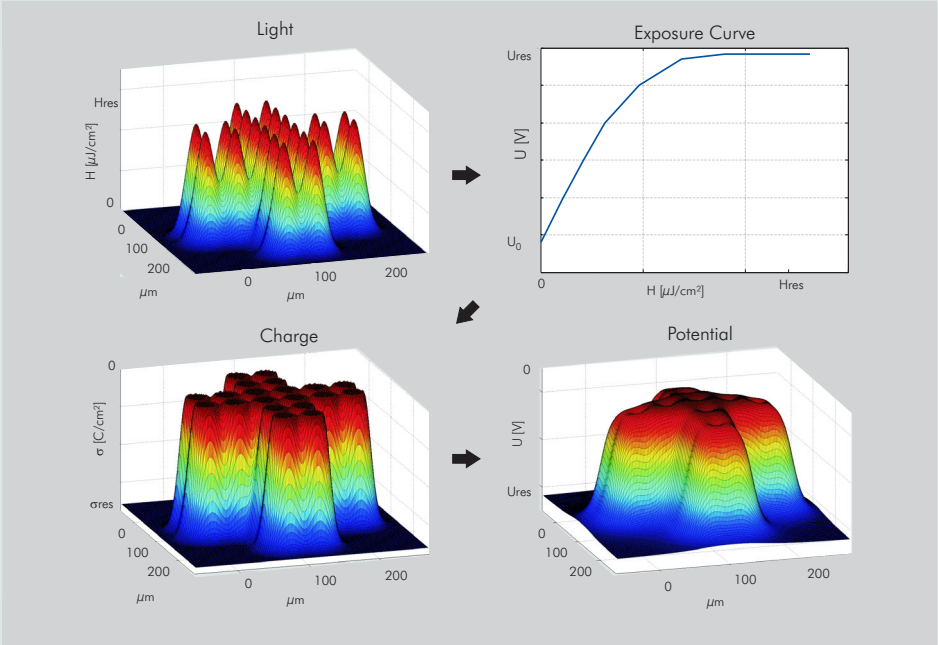

Figure 3.2: Distribution of light, charge and potential of a complex geometry

3.1 Corona charging process

The photoconductor is charged by a corona unit, consisting of several corona wires surrounded by a metallic shield. An AC voltage of high magnitude is applied to the wires to ionize the air around them. By applying a negative voltage to the shield, positive air ions are drawn towards the shield, while positive ions and free electrons are pushed towards the photoconductor, where they remain on the surface [Lea99].

To calculate the charge of the photoconductor the following steps are performed:

- For each time step Δt the potential and electric field of the corona is calculated, according to the applied voltages, using finite element methods (FEM).

- It is assumed that the charges from the corona wires move in small packages with charge δq, starting from N circularly arranged starting positions around each wire. Since the total current i in one wire is known, δq can be calculated as $\delta q = i \cdot \Delta t / N$. The motion of these packages is now calculated according to the electric field forces with the assumption that the electron velocity is high enough to reach either the photoconductor, or the corona shield, before the next time step starts. This can be justified by the measurements described in [Gal77] where the resulting transit time of the ions is between 50 μs and 100μs, whereas the cycle duration of the applied corona AC voltage is above 200 μs.

- The charge distribution on the photoconductor is then calculated from the density of charge packages reaching the photoconductor. At the end of the time step, the charge distribution is moved according to the photoconductor velocity.

3.2 Setup and functionality of the print head

A typical print head [Gol01] consists of about 10000 LEDs, mounted on a solid substrate, which are arranged in series across the entire width of the photoconductor (see fig. 3.4). Each diode addresses one print dot. The spacing between the LEDs corresponds exactly to the resolution desired for the printed image. With the help of the projecting optics, which comprises glass fiber lenses arranged in two rows, these LEDs perform an exact exposure of the photoconductor. The required data is delivered from the print controller, using special driver-chips along the print head. Figure 3.3 shows the comparison of a layer structure of an As_2Se_3 photoconductor versus an organic photoconductor (OPC). An As_2Se_3 photoconductor absorbs the incident light in the upper layer and generates electron-hole pairs in this layer. While the negative charges (electrons) compensate the positive surface charges and thus discharge the surface, the positive charges pass over to the counter electrode, the Al-drum. In contrast to this, the OPC absorbs the light in the charge generation layer, which is situated above the ground electrode on the carrier material. The positive charges thus generated penetrate the charge transport layer and compensate the imposed surface charges there, while the negative charges migrate directly to the ground electrode [Sch75].

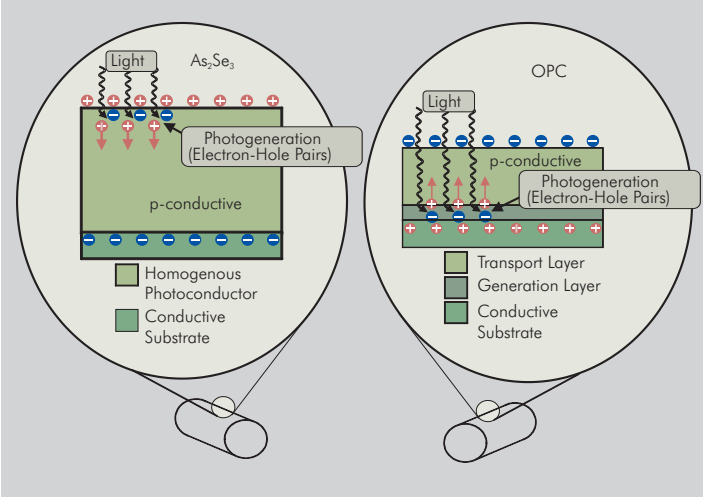

Figure 3.3: Charge generation for different types of photoconductors

3.3 Form and energy of the light dots

To determine an exact light distribution 3000 light dots from a print head were measured (Figure 3.4). As a result, the shape of a light dot can be approximated as Gaussian:

$$H = H_{max} e^{-\frac{1}{2}\left(\frac{(x-x_0)^2}{\sigma_x^2}+\frac{(y-y_0)^2}{\sigma_y^2}\right)}$$

The average light intensity per area H_{mean} is the full quantity of light Q of one dot, $Q = \int_{-\infty}^{\infty}\int_{-\infty}^{\infty} H dx dy$, multiplied by the amount of points per square centimeter. With a spacing of 42.3 μm (corresponding to 600 dpi) these are 55888 points.

$$H_{mean} = 2\pi\sigma_x\sigma_y H_{max} \cdot 55888 \frac{1}{cm^2}$$

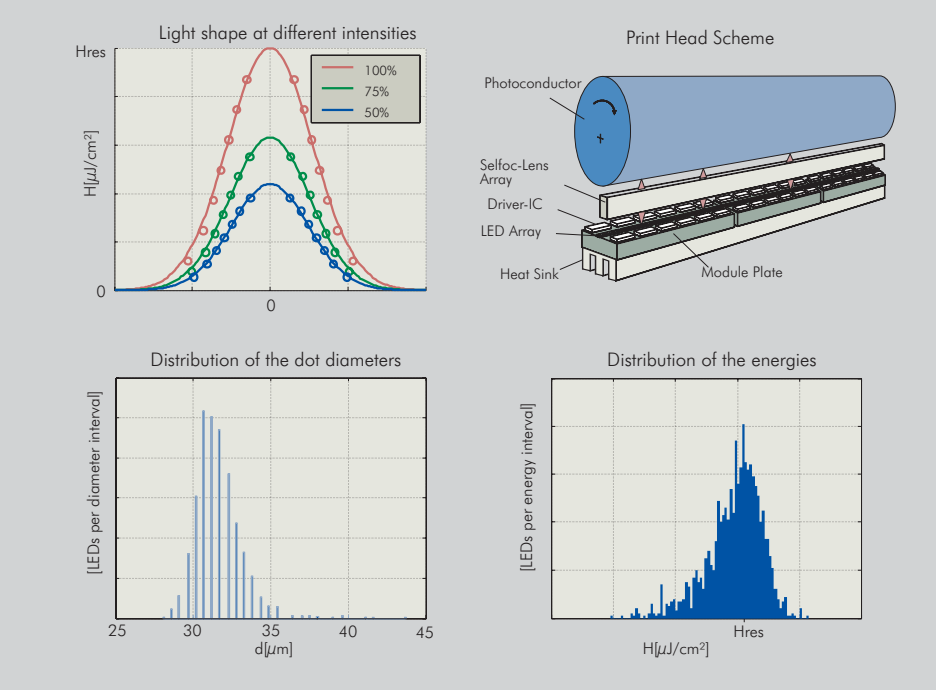

Figure 3.4: Measurement results from 3000 light dots

Furthermore, the values of each individual light dot can vary. The variation of the dot diameter is typically about 10 %, while the dot energy varies about 5 %. In the simulation, the dot diameters and energies of the used LEDs were distributed according to these measurements.

The results from these measurements can be used to create a realistic light distribution from a given print pattern by applying the gauss function and varying the diameter and the energy according to the measured distribution.

3.4 Motion of the photoconductor

During the switch-on time $T_{LED_{ON}}$ of a LED, the photoconductor moves on with constant velocity $\vec{v}$. To get the correct light energy that the photoconductor is exposed to, the light power Φ per area, i.e. the irradiance E, has to be integrated

$$H(\vec{x}, t) = \int_{T_{LED_{ON}}} E(\vec{x} - \vec{v}t, t)\, dt$$

The resulting light, charge and potential distribution of a moving photoconductor shows a slightly elliptic form compared to a resting one (see fig. 3.5).

As a consequence, the individual dots of a rasterized halftone screen will overlap in printing direction.

3.5 Exposure curve of the photoconductor

The exposure curve describes the discharge voltage of the photoconductor as a function of the print head light energy. It is gained by measuring the photoconductor surface potential after charging it with the corona (see chapter 3.1) and then discharging it with a print head, where all light dots are operated at a certain light energy level. In the simulation, the curve can therefore

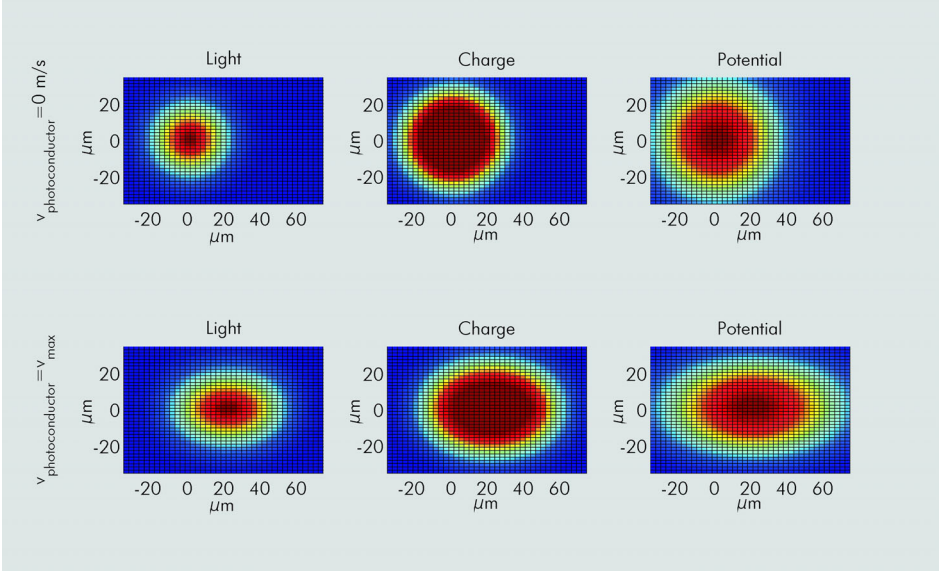

Figure 3.5: Comparison of moving and resting photoconductor

only be used for a correct calculation if the print pattern is a large homogeneous area. For smaller details, the curve has to be transformed from a light-potential to a light-charge-curve as described in chapter 3.6. From this charge distribution, the potential can be calculated by integration or by FEM calculations.

A typical feature of an exposure curve is the almost linear trend in the beginning and the saturation at higher light energies. In order to optimize the toner deposition, the maximum light energy is set to reach the saturation of the photoconductor.

The exposure curve for an organic photoconductor can be characterized by several specific values, depending on the material properties of the OPC (see fig. 3.6):

- Charge potential: U_0
- Extrapolation of linear beginning of the curve to 0 V: H_{lbo}
- Light energy to reach a potential of 100 V: H_{100}
- Residual Potential at H_{res}: U_{res} (Assumption $U_{res} = const$ for $H \geq H_{res}$)

3.6 Charge distribution

A capacitor model is used to calculate the charge distribution which is necessary to achieve the measured discharge potential at a certain homogeneous light energy. The photoconductor is modeled as a plate capacitor (thickness d) filled with a dielectric substrate ϵ_r. The lower plate is on zero potential. With these assumptions, the charge density σ on the upper plate necessary to achieve a certain potential U can be easily calculated:

$$\sigma = \frac{Q}{A} = \frac{\epsilon_r \epsilon_0 U}{d}$$

If an irregular light pattern is used for the exposure of the photoconductor, each dot of the photoconductor will receive a charge density corresponding to the light energy at that dot. This charge density is equal to the one resulting from a homogeneous exposure with that light energy.

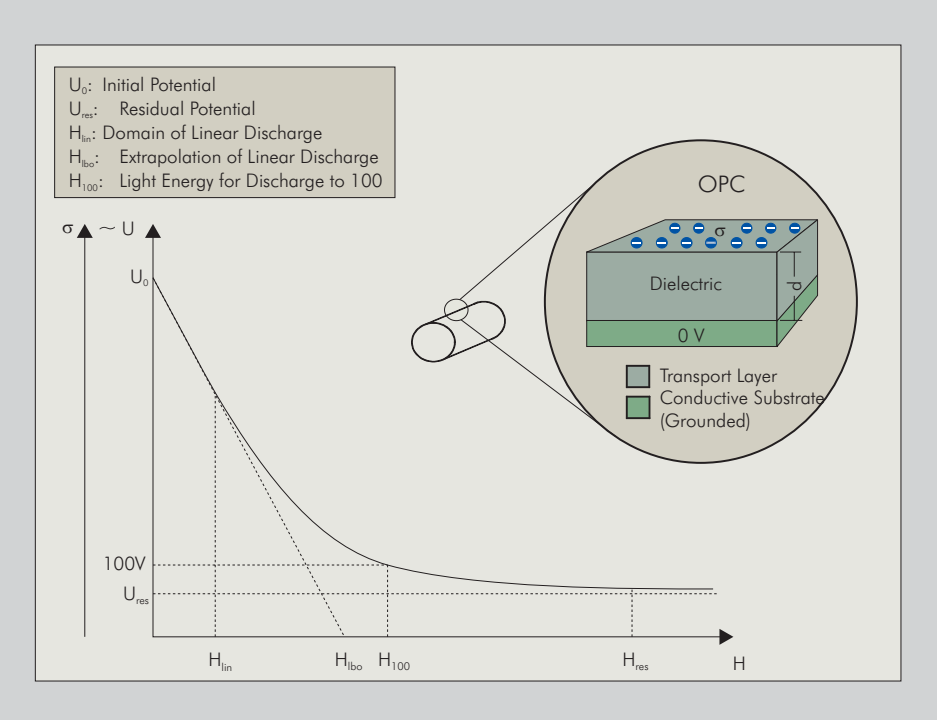

Figure 3.6: Typical OPC exposure curve

This is true under the premise that any blurring of the latent image due to a horizontal drifting of the generated electron-hole pairs is neglected. This can be justified by the small thickness d of the photoconductor and the high transversal electric field compared to the longitudinal field. With these assumptions the ordinate of the exposure curve can be rescaled in V instead of Q/m^2.

3.7 Potential calculation

The potential U at a point (x_0, y_0) at distance z_0 above the surface of the photoconductor can be calculated by integrating the charge distribution $\sigma(x, y)$

$$\begin{aligned} U &= \frac{1}{4\pi\epsilon_0} \iint \frac{\sigma(x,y)}{r}\, dA \\ &= \frac{1}{4\pi\epsilon_0} \int_{-\frac{L}{2}}^{\frac{L}{2}} \int_{-\frac{L}{2}}^{\frac{L}{2}} \frac{\sigma(x,y)}{\sqrt{(x_0-x)^2 + (y_0-y)^2 + z_0^2}}\, dy\, dx \end{aligned}$$

L is the product of the amount of light dots and their spacing. To simulate a potential sensor, (x_0, y_0) is varied over all points. The distance z_0 is set at the radius of a toner particle ($3.5\,\mu m$). The potential value calculated this way is only useful for getting a quick approximation how the potential distribution of a complex print pattern (see fig. 3.2) looks like, compared to the charge distribution. It does not take the opposite electrode in account. This is only possible by a FEM calculation which can also determine the resulting electric fields (chapter 5.3.1), as they are required for the n-body simulation.

3.8 Summary

To calculate the charge distribution on the photoconductor for a given print pattern, the following steps have to be performed:

1. Assign each LED an energy and dot diameter, according to the measured statistical distribution.
2. Calculate the light pattern from the used LEDs.
3. Distort the light pattern according to the photoconductor motion.
4. Convert the measured light-potential exposure curve to a light-charge exposure curve.
5. Use this curve to transform the light distribution $H(x)$ to a charge distribution $\sigma(x)$.

This charge distribution will be used in chapter 5 to calculate the actual electric fields governing the toner deposition.

Chapter 4

Developer station

The developer station accounts for a continuous, homogeneous supply of charged toner to the development nip. As mentioned above, the charging process is performed by intensely mixing the developer mixture of toner and carrier. This leads to the charge distribution described in chapter 2. Then, the toner has to be separated from the carrier, and deposited in a uniform layer on the jump roller. This is done in the gap between the magnetic roller and the jump roller. Between these rollers, a "brush" consisting of carrier particles is formed: The carrier particles arise because they are aligned along the field lines of the permanent magnets within the magnetic roller. Their tips touch the jump roller, while the toner, owing to the electrostatic force of the potential difference between the rollers, is drawn onto the jump roller.

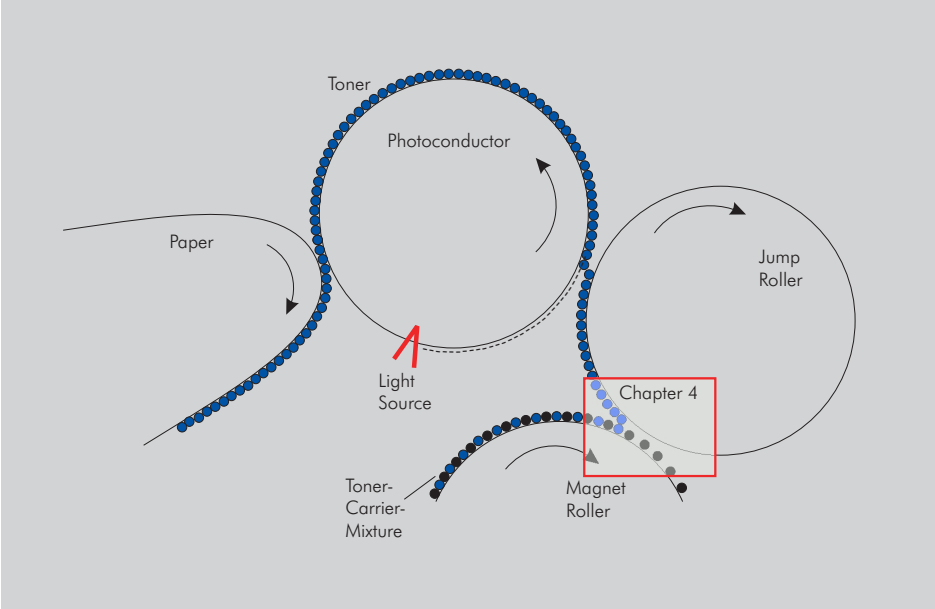

Figure 4.1: Process steps

It is important to simulate the toner deposition process in the magnetic brush correctly, to ensure proper initial conditions for the jumping process in the development nip. The most obvious approach is a many-body simulation of the toner-carrier mixture, where the carrier particles follow mainly the magnetic forces, while the charged toner particles are deposited due to the applied voltages. Such a simulation requires the external fields (air flow, magnetic, electric) as input conditions, and has to model the particle-field and particle-particle interactions correctly.

4.1 External fields

4.1.1 Air flow

The air flow $\vec{v}(\vec{x})$ through the nip was determined by finite element calculations where the Navier-Stokes equation [GV93]

$$\begin{aligned} \rho \cdot \vec{v} \cdot \vec{\nabla} \vec{v} &= -\vec{\nabla} p + \eta \triangle \vec{v} \\ \vec{\nabla} \cdot \vec{v} &= 0 \end{aligned}$$

is numerically solved with the assumption of a stationary laminar flow of an incompressible medium ([GS00], see fig. 4.2). Due to the relatively low particle density in the nip, there is no significant feedback from particle motion to the air flow to be expected, so that the air flow can be calculated once and is then considered to be constant throughout the simulation. The assumption of laminarity can be justified by the Reynolds number [Kuc91]

$$\begin{aligned} Re &= \frac{l \rho v}{\eta} \\ &= \frac{1250 \mu m \cdot 1 \frac{kg}{m^3} \cdot 1.5 \frac{m}{s}}{17.2 \mu Pa \cdot s} \\ &\approx 110 \end{aligned} \tag{4.1}$$

where l is the width of the nip, ρ the density of air, v the velocity of the boundary and η the dynamic viscosity of air. The resulting Reynolds number of about 110 is far below the critical value where turbulence starts ($Re \approx 1000$).

The boundary conditions for the FEM calculation were the tangential velocity of the jump roller and the magnet roller, as it can be assumed that the air adjacent to a roller moves in a stationary state ($\vec{v}(\vec{x}) = const$) uniformly with the roller surface. Figure 4.2 shows the calculated velocity field. Since the two rollers have opposite directions of rotation, a zone of non-moving air separates the rollers.

4.1.2 Magnetic field

The magnetic field distribution $\vec{B}(\vec{x})$ (fig. 4.3) that mainly determines the behavior of the carrier particles, also results from FEM calculations, where the 2-dimensional equation [Ste97]

$$-\vec{\nabla} \cdot \left(\frac{1}{\mu} \vec{\nabla} A_z - \begin{pmatrix} -M_y \\ M_x \end{pmatrix} \right) = 0$$

is numerically solved for A_z, the z-component of the magnetic vector potential $\vec{A}$ [Jil91]. The magnetic flux density $\vec{B}$ can then be calculated from $\vec{B} = \vec{\nabla} \vec{A}$.

The problem is that the magnetization $\vec{M}$ of a permanent magnet depends on the magnetic field intensity $\vec{H}$, following the second quadrant of its (nonlinear) hysteresis curve, which is the normal operation mode for permanent magnets [Cam96]. Therefore, a nonlinear, iterative solver has to be employed to solve the equation [Ste97, Com02]

$$\vec{H} = \vec{B}/\mu - \vec{M}\left(\vec{H}\right)$$

The main input parameters for the FEM calculation are therefore the geometric positions of the permanent magnets and their hysteresis curves, which are provided by the manufacturer.

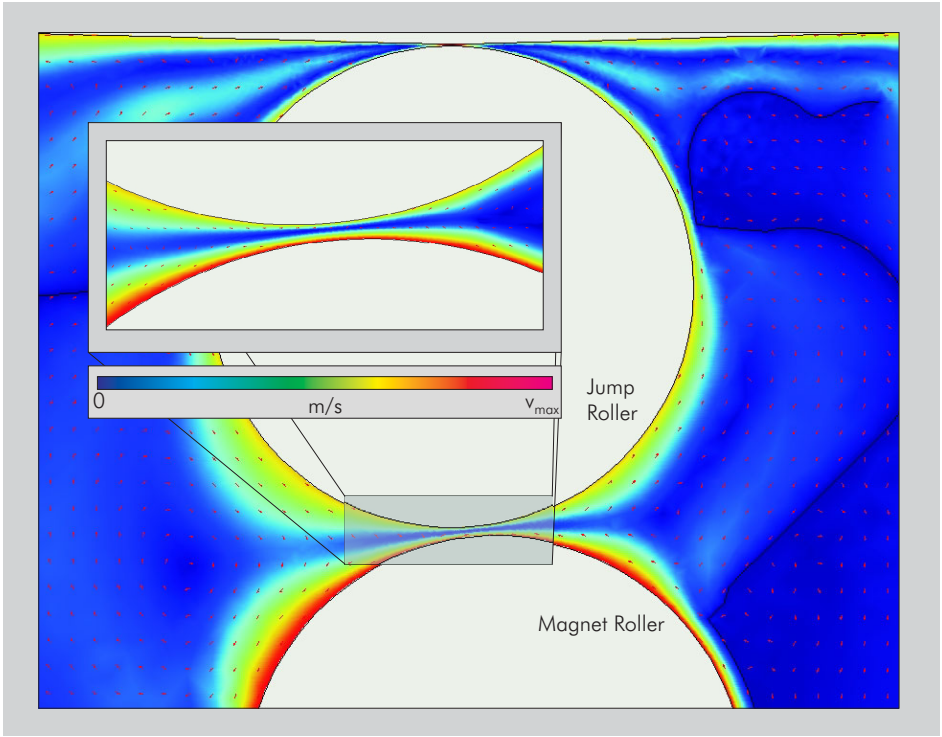

Figure 4.2: Velocity field of the air flow

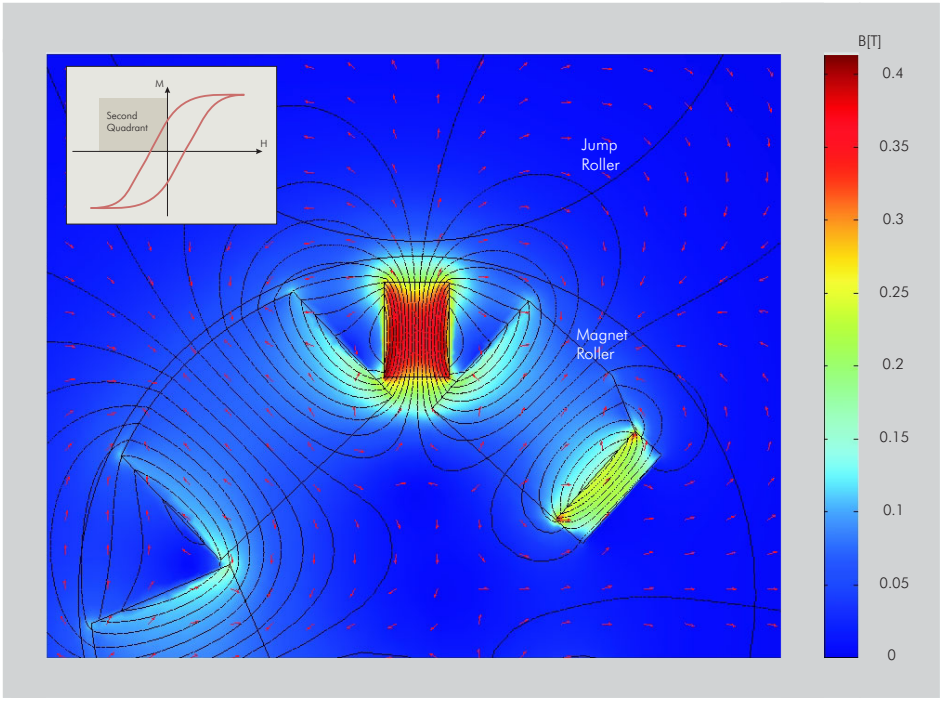

Figure 4.3: Magnetic field (small figure: Hysteresis curve of permanent magnet)

4.2 Magnetic brush many-body simulation

4.2.1 Equation of motion

Performing an n-body simulation consists essentially of solving a coupled system of second-order differential equations, i.e. the equation of motion for every particle, with the force depending on the position of some or all other particles. This is based on the model proposed first by Cundall & Strack [CS79], which is now known as the classical discrete element method (DEM) and has been proven to be a versatile numerical tool, particularly suitable for the simulation of granular and particulate systems [OFC02, OF02]. A common way to speed up the simulation of the mechanical behavior of a granular system is to upscale the system by using larger particles than in reality, so that the total number of particles can be reduced [KK02]. However this is not possible for the simulation intended here, since an upscaling results in a different ratio of particle volume to particle diameter. This would falsify the ratio of the various forces since some of them depend on the particle mass and therefore the particle volume (like the magnetic forces) and others on the particle diameter (like the air friction forces). Therefore the particle size for the DEM simulation has to be chosen according to the real particle size, regardless of the resulting larger computation times.

$$\begin{aligned} m_i \ddot{\vec{x}}_i &= \vec{F}_i(\vec{x}_i, \vec{x}_j, \dot{\vec{x}}_i) \\ &= \underbrace{\vec{f}_{mag_{field}}(\vec{x}_i)}_{particle-field} + \underbrace{\vec{f}_{vis}(\dot{\vec{x}}_i)}_{particle-air} \\ &+ \underbrace{\sum_j \vec{f}_{mag_{ij}}(\vec{x}_i, \vec{x}_j) + \sum_j \vec{f}_{col_{ij}}(\vec{x}_i, \vec{x}_j)}_{particle-particle} \end{aligned}$$

The force on a carrier particle consists essentially of two dominant components:

1. The forces resulting from external fields:

   $\vec{f}_{mag_{field}}$ The magnetic field force due to the permanent magnets, which does not depend on the simulation time t like the electric field force

   $\vec{f}_{vis}$ Friction force due to the motion of the particle in an air flow

2. The forces resulting from particle-particle interactions

   $\vec{f}_{mag_{ij}}$ The magnetic force resulting form the dipole-dipole interaction between the magnetized particles i and j

   $\vec{f}_{col_{ij}}$ Forces emerging from particle collisions

Other forces, like van-der-Waals adhesion forces between adjacent particles or between particles and rollers, can be neglected for carrier particles, since the magnetic forces for the particles used here are more than a hundred times higher. Adhesion forces will, however, be very important for the toner simulation in chapter 5.

4.2.2 Initial configuration

To integrate the differential equations, initial values have to be chosen for the state variables position $\vec{x}$ and velocity $\dot{\vec{x}}$ of each particle. Since the thickness of the carrier layer in the developer

station is limited by a blade an initial, compact layer of carrier particles was chosen, with the layer thickness equivalent to the distance between the blade and the magnet roller. The velocity vector was aligned parallel to the magnet roller surface with the absolute value equivalent to the roller surface speed. The orientation of the magnetization for these initial particles was set parallel to the external magnetic field (see fig. 4.4).

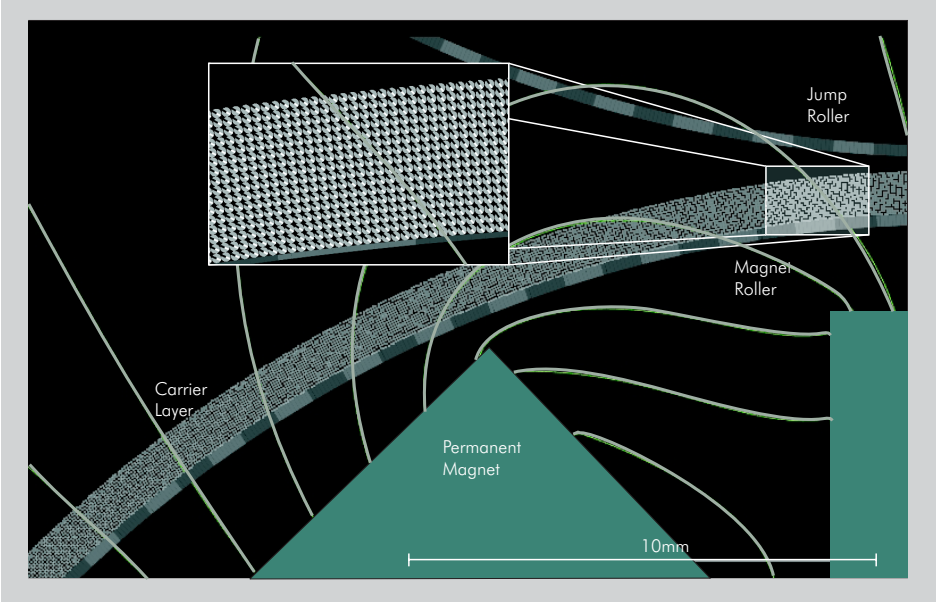

Figure 4.4: Initial configuration for 16000 carrier particles

4.2.3 Friction force $\vec{f}_{vis}(\vec{x}_i, \dot{\vec{x}}_i)$ in air flow

Assuming a spherically shaped particle, the force due to the air flow can be calculated using Stokes' Law since the corresponding Reynolds number is about 4...6, so that the flow around the particle can be considered to be laminar. Actually Stokes' Law is usually only considered to be valied for $Re < 1$, but the total error on the simulated forces proved to be less than 1.5% even for the higher Reynolds numbers. The force is proportional to the velocity of the particle relative to the velocity of the air at the particle position. Since the air flow is considered to be stationary the air velocity can be taken from the lookup-table where the results from the previous FEM calculation (chapter 4.1.1) were stored.

$$f_{vis}(\vec{x}_i, \dot{\vec{x}}_i) = -6\pi\eta_{air} r_i (\dot{\vec{x}}_i - \vec{v}_{air}(\vec{x}_i))$$

where η_{air} is the dynamic viscosity of air (17.2 μPa·s) [Kuc91].

4.2.4 Carrier magnetization

The carrier used consists of ferrite particles with a distinctly soft magnetic behavior so that the magnetization curve shows almost no hysteresis, as the measurements (see fig. 4.5) have confirmed. As a consequence, the assumption that the magnetization will follow the external fields almost instantaneously is justified. This will be important for the simulation. Another important aspect is the fact that the carrier does not reach its saturation magnetization for fields as they occur in the developer station. Therefore, the magnetization value in the simulation has to be adjusted every time step according to the respective external fields.

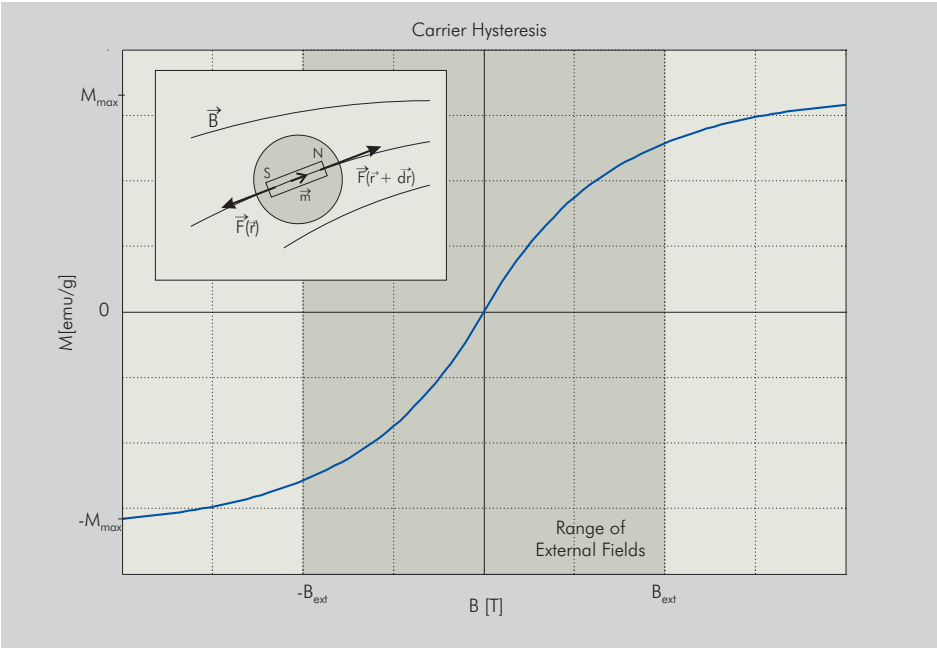

Figure 4.5: Carrier magnetization curve

4.2.5 Magnetic field force $\vec{f}_{mag_{field}}$ effected by permanent magnets

A magnetized particle, that can be approximated as a magnetic dipole, experiences various forces when interacting with an external field. First, a torque will turn the magnetization vector of the dipole parallel to the external field. This can either be achieved by actually turning the whole particle, or by realigning the magnetic domains within the particle. If the field is inhomogeneous, an accelerating force will also be applied to the particle.

This can be justified by considering the particle as a magnetic dipole with length $d\vec{r}$. The force on one pole is $\vec{F}(\vec{r})$, and on the other pole is $\vec{F}(\vec{r}+d\vec{r})$, so the force on the whole particle is $\vec{F} = \vec{F}(\vec{r}+d\vec{r}) - \vec{F}(\vec{r})$ (see small illustration in fig. 4.5). This means that the force depends on the gradient of the magnetic field [Pur83]

$$\vec{F} = \left(\vec{m}\cdot\vec{\nabla}\right)\vec{B} \tag{4.2}$$

However, there is a significant difference between the electric field force and the magnetic field force: Since the magnetic field force depends on the angle between the magnetization vector and the field vector, the force due to several field sources can not be calculated by linear superposition of the force from each field source. On the contrary, as described in 4.2.6 below, the fields from all sources (i.e. the other magnetized particles plus the permanent magnet) have to be summed up to calculate the total force.

4.2.6 Magnetic field forces $\vec{f}_{mag_{ij}}$ caused by carrier-carrier interaction

Due to its magnetization in the external field, every carrier particle creates a dipole field of its own [Jac82]

$$B_r = 2\,|\vec{m}|\,\mu_0\frac{\cos\theta}{r^3} \tag{4.3}$$

$$B_\theta = |\vec{m}|\,\mu_0\frac{\sin\theta}{r^3} \tag{4.4}$$

which can be written in Cartesian coordinates

$$\vec{B}(\vec{x}) = \mu_0 \frac{3\vec{n}(\vec{n}\cdot\vec{m}) - \vec{m}}{|\vec{x}_0 - \vec{x}|^3}$$

where $\vec{n}$ is a normalized vector pointing from $\vec{x}_0$ to $\vec{x}$

$$\vec{n} = \frac{\vec{r}}{r} = \frac{\vec{x}_0 - \vec{x}}{|\vec{x}_0 - \vec{x}|}$$

The problem is that the magnetization vector of each particle in turn depends on the dipole fields, and thus on the magnetization of the other particles around it. For particle numbers greater than two, this problem can only be solved iteratively.

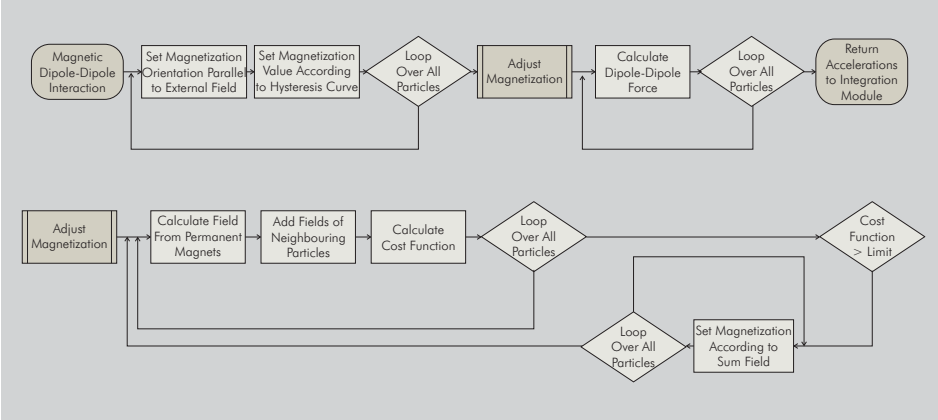

Figure 4.6: Flow chart for magnetic dipole interaction

The flow chart in fig. 4.6 shows the approach:

1. The initial conditions are chosen by setting the orientation of the magnetization vector parallel to the external field, and its value according to the hysteresis magnetization curve.

2. Then a loop is performed where, for each particle, the closest neighboring fields, are summed up. Since magnetic fields decrease with $O\left(\frac{1}{r^3}\right)$, it is not necessary to take the whole particle set into consideration. An efficient way to determine all particles within a certain distance from the current particles is to employ the tree code algorithm described in chapter 6.5.

3. A cost function, consisting essentially of the inner product between the sum of the magnetic fields at a particle position and magnetization of the particle, is evaluated:

$$c_f = \sum_i \frac{\left(\vec{B}_{ext_i} + \sum_j \vec{B}_{ij}\right)\cdot\vec{m}_i}{\left|\vec{B}_{ext_i} + \sum_j \vec{B}_{ij}\right| |\vec{m}_i|}$$

4. If the cost function is above a predefined limit, the orientation of the particles is consistent with their generated fields, and the force on the particle can be calculated using (4.2)

$$F_{mag_k} = \sum_l m_l \frac{\partial B_k}{\partial_l}$$

where $\vec{B} = \vec{B}_{ext} + \sum_j \vec{B}_{ij}$ is the sum of the external field and the dipole fields of the nearest neighbors

5. Otherwise, the orientation of the particles is set parallel to the calculated magnetic field, the absolute value of the magnetization is set according to the magnetization curve, and the calculation starts anew.

The whole procedure is performed at the beginning of every time step. The implicit assumption is that the timescale of the realignment of the particles is much smaller than the timescale of particle motion.

4.2.7 Results

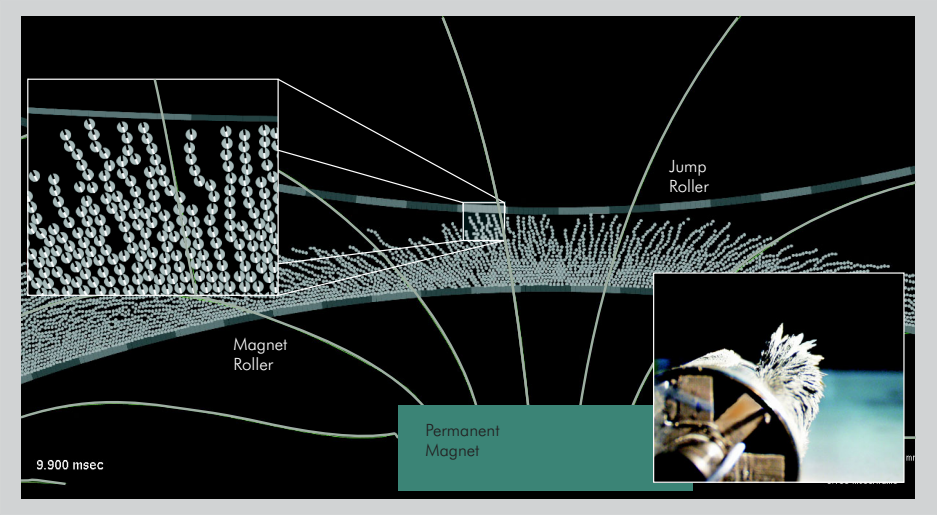

Figure 4.7: Carrier particle simulation

Fig. 4.7 shows the result of a simulation run with 16000 carrier particles. The carrier magnetic brush between the magnet roller and the jump roller can be clearly observed, its size is about the size measured in a real developer station. The magnification shows the carrier particles forming small chains parallel to the magnetic field lines, as they can also be observed (see attached photo in fig. 4.7) in an experiment where carrier powder is brought near a permanent magnet [NK02]. The black-and-white lines inside the magnified carrier particles indicate the magnetic orientation of the particles. As expected, the carrier particles are aligned such that the north and south pole of two adjacent particles are in close proximity.

The main drawback of this method is the required computation time. Due to the additional iterations necessary to adjust the magnetic orientation, a carrier simulation takes up to four times longer than a pure toner simulation. However, this includes only the simulation of the motion of the carrier particles themselves. Although the results from these simulations can be extremely helpful for optimizing the magnet configuration of the developer station, they are not sufficient for this work. To predict the toner deposition behavior of the developer station, it is obviously necessary to simulate the motion of the toner and carrier mixture.

A typical developer mixture contains about between 1% and 10% of toner. For an example of 5% of toner this leads to a toner/carrier particle ratio of

$$\frac{N_{Toner}}{N_{Carrier}} = \frac{0.05}{0.95}\frac{\rho_{Carrier}}{\rho_{Toner}}\left(\frac{r_{Carrier}}{r_{Toner}}\right)^3 \approx 200$$

Some simulation experiments with a small number of carrier particles and an adequate number of toner particles proved to be be quite successful (see fig. 4.8): The carrier particles are aligned

along the field lines while the toner particles cover the carrier almost completely, as the SEM micrographs have shown. However, the available computation capacity was far from being sufficient to solve a complete magnetic brush simulation in an adequate time. In addition to the high number of particles, the time step size also has to be reduced, due to the large difference in size between the toner and carrier particles: Two colliding carrier particles will create an overlap of about 0.5 % of their radius per time step at typical velocities before the repulsive forces (see chapter 5.8.3.2) take effect. Since the size of carrier particles is several times the size of toner, the overlap of a carrier particle colliding with a toner particle would be about 5 % of the toner radius, resulting in high numerical errors up to a complete penetration of the toner. To avoid this, the step size has to be reduced at least by a factor 5, leading to a corresponding extension of the computation time. For the example shown here, the simulation time needed with 2 GHz Pentium 4 Processors was about 100 h.

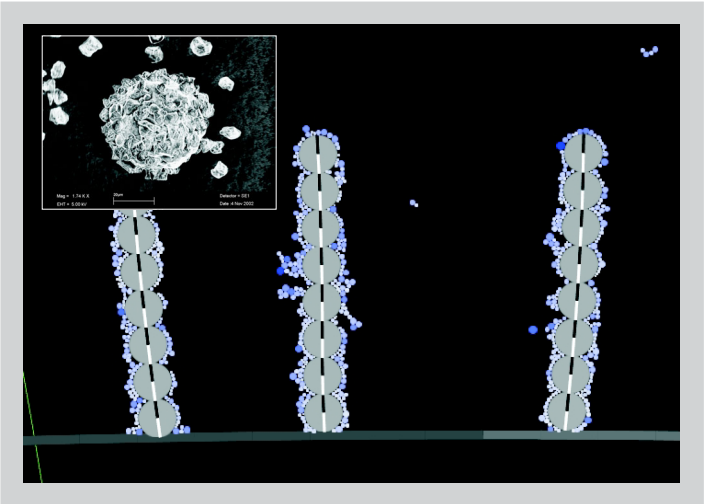

Figure 4.8: Toner-carrier simulation (SEM micrograph of toner-covered carrier)

All in all, these effects lead to a simulation time for a toner-carrier mixture which is more than a hundred times longer than for a toner jump simulation (chapter 5). Therefore, a simplified method had to be chosen to simulate the toner deposition characteristic of the developer station.

However, the algorithm developed here is valuable anyway: The carrier simulation shown above can be used to improve the magnetic setup of the developer station. The goal here is to reduce the heat produced in the station. This can be achieved by analyzing the carrier motion in the simulation results and then by adjusting the magnet configuration so that carrier-roller friction as a heat source is reduced. The carrier-toner-simulation has also shown to produce plausible results. While it cannot be used now due to computation time restrictions, is written in a cross-platform compatible way, so that it can be ported to a vector or massive parallel hardware platform. In addition, the future development of computer hardware will make it possible to reduce computation time, so that this algorithm can be used also on standard platforms.

4.3 Stochastic magnetic brush modeling

As mentioned before, the complex motion of the carrier brush has the main effect of bringing toner particles in close contact to the jump roller, thus enabling it to be withdrawn from its carrier and to be deposited on the jump roller, due to the influence of the applied electric field. Instead of performing the complex DEM simulation described above, this process can be

approximated by sequentially offering toner particles at random positions to a segment of the jump roller, with a width similar to the width of the magnetic brush. The particle properties radius, charge and adhesion are distributed according to previous measurements (chapter 2). For each of these particles the electric force $F_{el} = qE$ drawing it towards the jump roller is compared with the repulsive coulomb force of the already deposited particles $F_{coulomb}$, the toner-substrate adhesion force $F_{toner-substrate}$, the toner-toner cohesion force $F_{toner-toner}$ and the toner-carrier adhesion force $F_{toner-carrier}$:

$$F_{el} + F_{toner-substrate} \geq \sum F_{coulomb} + F_{toner-carrier} \quad (4.5)$$

$$F_{el} + F_{toner-toner} \geq \sum F_{coulomb} + F_{toner-carrier} \quad (4.6)$$

If a particle is tested at a position, where no other particles have been deposited before and the electric forces plus the adhesion force between toner and substrate exceeds the coulomb forces plus the toner-carrier adhesion force (4.5), it is supposed that the toner particle is detached from the carrier and deposited on the jump roller. If another toner particle was already deposited at that position, the toner-substrate adhesion force form (4.5) changes to the toner-toner cohesion force (4.6).

The deposition process assumes that only the newly deposited particle can move, while all the other particles remain in their previously attained positions. The current particle tries to get as close to the roller as possible, resulting in four basic cases (see fig. 4.9), which the algorithm has to take into account:

1. The particle position interferes with none of the already deposited particles, therefore it can be deposited directly on the substrate.

2. The particle meets a second particle: It then 'rolls' down that particle, and if it doesn't touch a third particle, it will be deposited on the substrate next to the second particle.

3. While rolling down the second particle, a third particle is encountered. If these particles form a stable local minimum the current particle will be deposited there.

4. If no stable local minimum is attained, the particle keeps on rolling down, until either case 2 or 3 is finally reached.

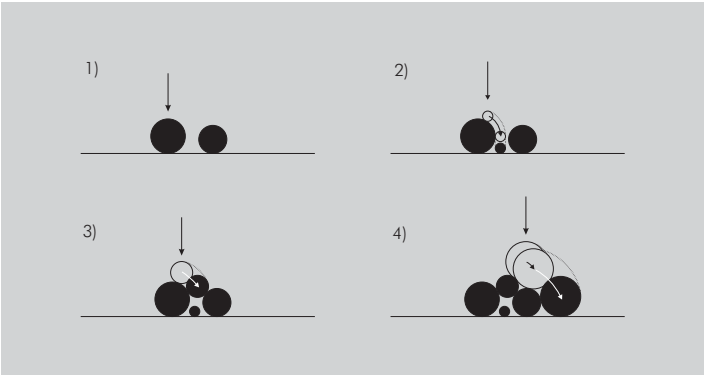

Figure 4.9: Geometric deposition algorithm

This procedure leads to a densely packed layer of toner particles (the packing density varies between 75 % and 85 %). Compared to a random deposition without consideration of the

force equation (4.5), however, the particle properties like charge or cohesion are not distributed uniformly across the layer thickness (see fig. 4.10). The charge per particle increases towards the outside of the particle layer. The reason is that the electric force which is detaching the toner from the carrier has to overcome the toner-carrier adhesion and the repulsive force from the already deposited particles. This means that the probability for particle detachment from the carrier rises with higher particle charge and lower particle adhesion force. The adhesion force dependency can also be seen in the resulting diagram. The particle set which is used as input for the deposition algorithm has a wide adhesion distribution, but for each radius class the mean adhesion value is proportional to the radius. However, at the deposited toner layer, the ratio of adhesion and radius is decreasing towards the outside. And since charge and cohesion are correlated with the particle radius, the radius is also not uniformly distributed.

The lower left diagram in fig. 4.9 shows part of a sample layer that was created using the geometric deposition algorithm. Blue color indicates negative charge. Although there is no strict sorting order, it can be observed that there is a tendency towards larger, higher charged particles towards the outside.

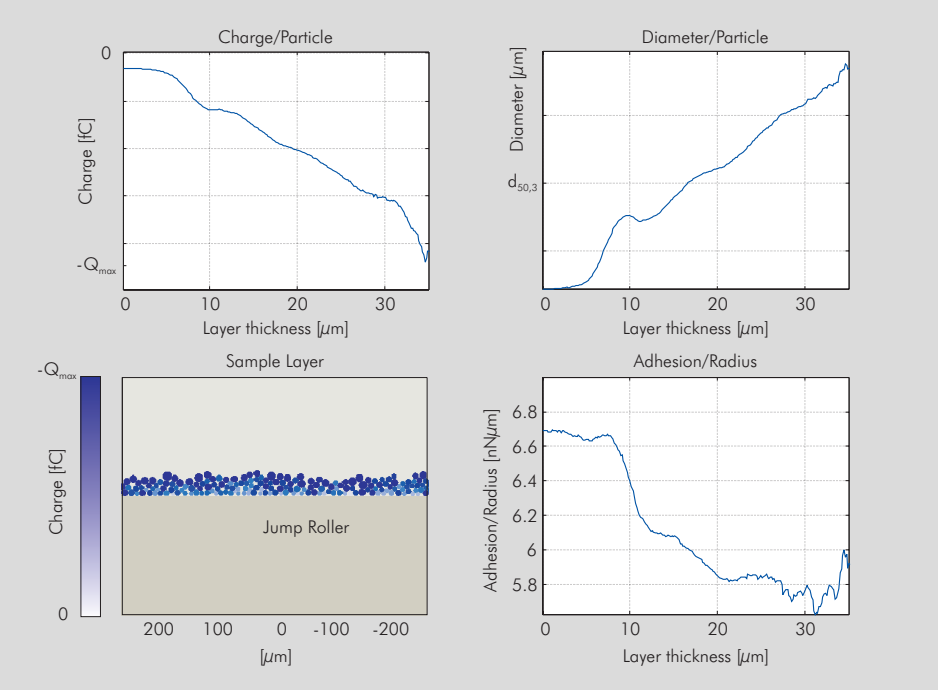

Figure 4.10: Results from stochastic deposition algorithm

Unfortunately, there is no direct way of verifying the results of this modeling approach. However, by comparing the results from the toner simulation with the experiments (see chapter 7) it can be shown, that it is necessary to choose the initial configuration of the toner simulation according to the results of the stochastic magnetic brush modeling introduced here.

Chapter 5

Development nip

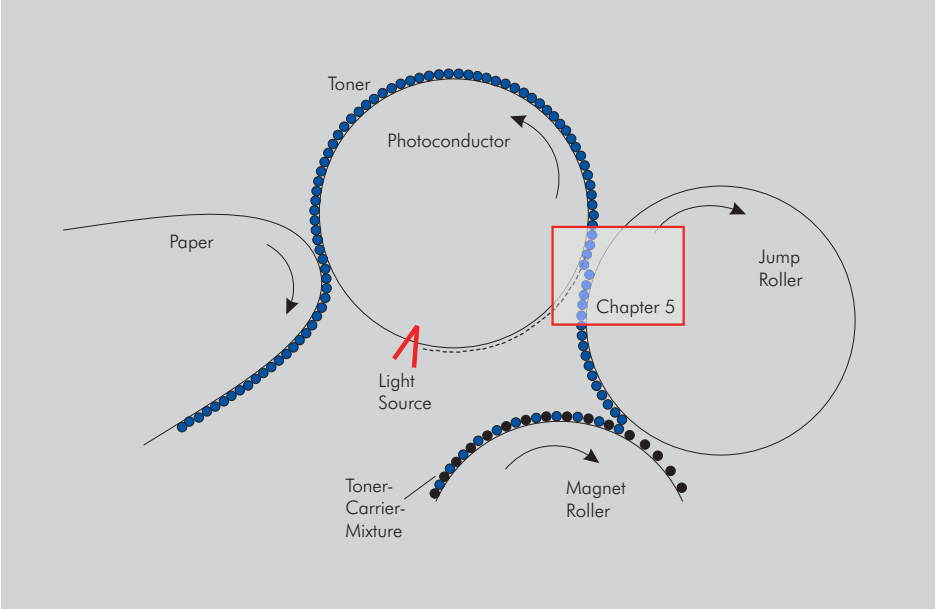

Figure 5.1: Process steps

The development nip is the essential part of the printing process where the homogeneously distributed toner from the jump roller (see chapter 4) jumps over an air gap towards the photoconductor. There, the deposition of the toner follows the electrostatic charge pattern due to the previous exposure of the photoconductor (see chapter 3).

As shown in figure 5.2, the development nip is restricted by the rotating jump roller and the moving photoconductor. The jump roller has to reach the development nip homogeneously covered with toner; the photoconductor has a potential image produced by corona charging and selective exposure as described in chapter 3. In the development nip, the charged toner moves due to the electric fields from the jump roller to the discharged areas on the photoconductor.

5.1 Specification of the electric setup

The photoconductor is grounded on the backside, while the charge density on top of the fully charged photoconductor creates a static potential U_{OPC} (see chapter 3.6) . An AC voltage combined with a DC offset is applied to the jump roller so that the DC potential U_{DC} is

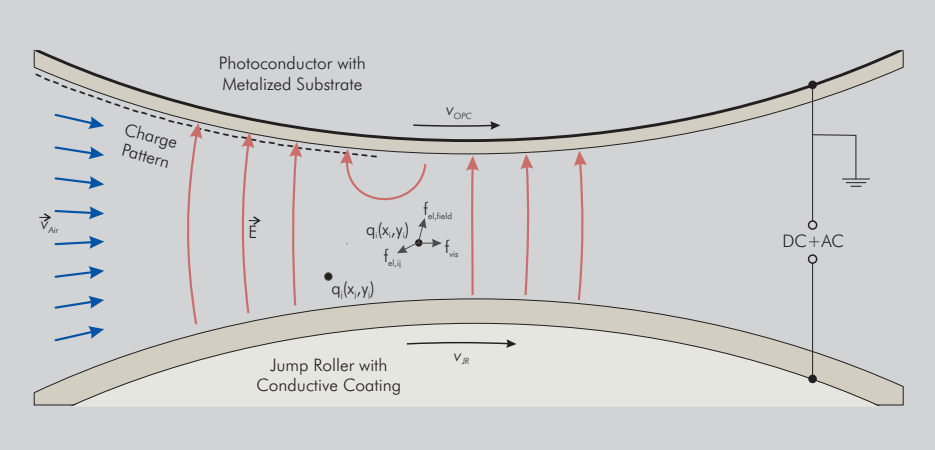

Figure 5.2: Development nip

between the charged and the discharged photoconductor potential. This is important to ensure maximum attractive forces towards the discharged areas and maximum repulsive forces away from the charged areas.

Fundamental charge patterns Four different cases shall be observed as elementary charge patterns, that occur in almost every typical test application (see fig. 5.3). These cases show most of the optimization problems in a typical print process.

- Homogeneous charging (background): Ideally, no toner should be deposited in that area. However, real print applications always show a certain amount of toner in these areas. The task is to find out the factors that influence the level of background toner.
- Homogeneous discharging (maximum toner deposition): In an optimized process, 100 % of the toner from the jump roller should be deposited in these areas.
- Edge (charged half-plane): Some print processes show an undesirable "edge effect", meaning that the optical density at an edge is much higher than in a homogeneous covered toner area, due to the higher electric fields near the edge.
- Periodic Lines (width 42 μm = 1 pixel): The human eye is very sensitive to small disruptions in a periodic pattern. It is therefore important to guarantee a homogeneous toner deposition on every line.

5.2 Air flow in the nip

As in chapter 4.1.1, the air flow through the nip was determined by finite element calculations, with the assumption of a stationary laminar flow of an incompressible medium. The assumption of laminarity can be justified by the Reynolds number of about 20, calculated by using (4.1).

The boundary conditions were the tangential velocity of the jump roller and the photoconductor. Figure 5.4 shows the calculated velocity field, with a clearly visible velocity maximum in the center of the nip, more than 50 % higher than the roller velocity.

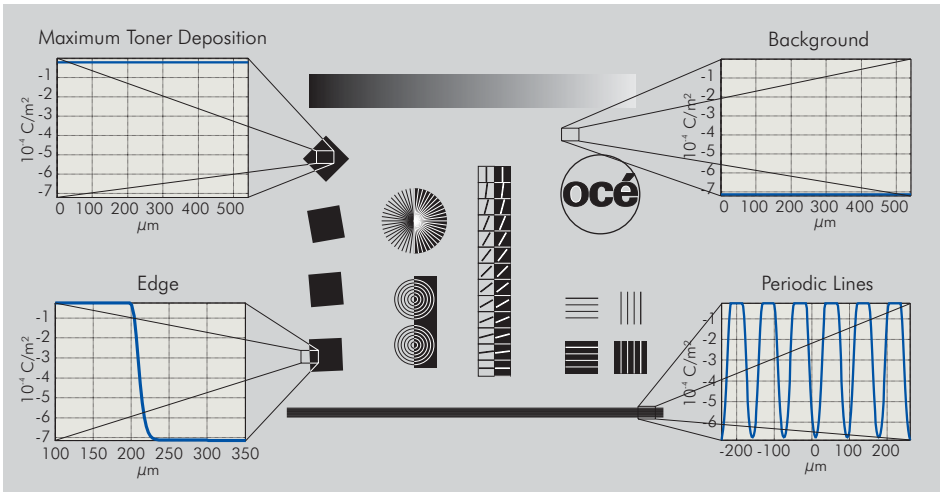

Figure 5.3: Typical test page showing the four elementary charge patterns

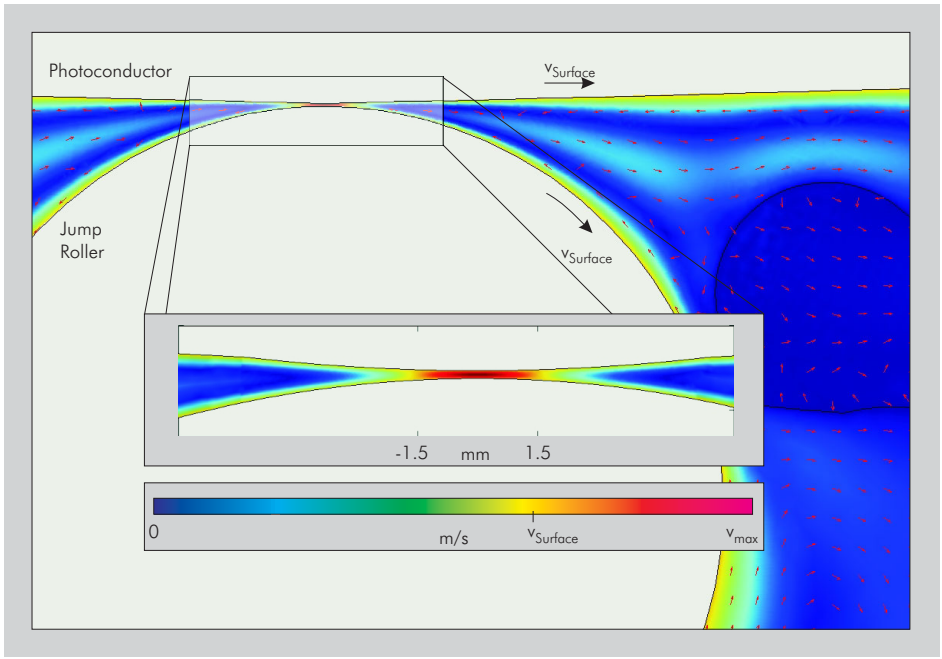

Figure 5.4: Velocity field of the air flow

5.3 Electric field in the nip

5.3.1 Static FEM calculation

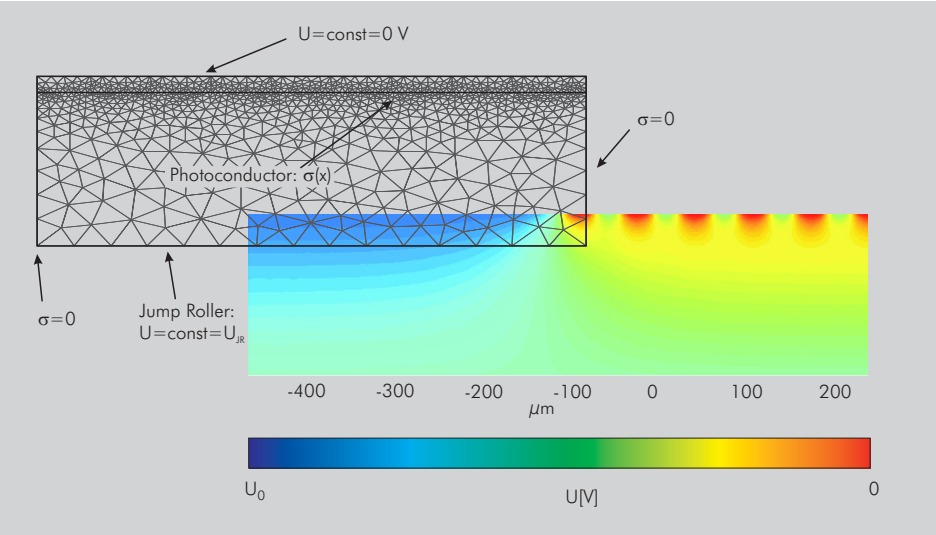

Figure 5.5: FEM calculation of the electric field

A finite element model is used to calculate the electric field distribution by solving the Poisson equation [Jac82]

$$\triangle U = -\frac{\rho}{\epsilon_0 \epsilon_r}$$

The boundary condition for the jump roller is a constant potential U_{JR}, while the bottom of the photoconductor is grounded. A Neumann condition is applied to the side boundaries with $\sigma = 0$, i.e. no field lines can start or end on these boundaries. This condition is only valid if the charge distribution is completely homogeneous, or at least any inhomogeneities are far from the side boundaries (e. g. the left border in fig. 5.5). This means in practice for an inhomogeneous charge distribution, that the calculation has to be extended so that the boundary is far enough from the inhomogeneity. Another application for this condition is the calculation of symmetric charge distributions on the photoconductor, like periodic lines (e. g. the right border in fig. 5.5). On the boundary between photoconductor and development nip, the above calculated photoconductor charge density $\sigma(x)$(see chapter 3) is applied.

To solve the Poisson equation with finite element methods, a mesh is created, using a Delaunay triangulation, so that a system of linear equations can be constructed.

5.3.2 Time-harmonic electric field

To increase the toner transfer efficiency (as shown in chapter 2.5), an AC voltage component is added to the jump roller voltage. Therefore, the electric field will also vary in time, requiring a recalculation at every time step. To avoid this, the field is calculated first for two stationary states ($U_{JR} = 0V$, $U_{JR} = 100V$). The results ($\vec{E}_0(\vec{x}_i)$, $\vec{E}_{100}(\vec{x}_i)$) are stored and then used in the simulation to calculate the field at time step t as the linear superposition of the two stationary states. For a sine-wave voltage of frequency f the electric field $\vec{E}(\vec{x}_i, t)$is

$$\vec{E}(\vec{x}_i, t) = \vec{E}_0(\vec{x}_i) + \left(\vec{E}_{100}(\vec{x}_i) - \vec{E}_0(\vec{x}_i)\right)\frac{U_{DC}}{100V} + \left(\vec{E}_{100}(\vec{x}_i) - \vec{E}_0(\vec{x}_i)\right)\frac{U_{AC}}{100V}\sin 2\pi f t$$

while for a square-wave voltage $\vec{E}(\vec{x}_i, t)$is

$$\vec{E}(\vec{x}_i, t) = \vec{E}_0(\vec{x}_i) + \left(\vec{E}_{100}(\vec{x}_i) - \vec{E}_0(\vec{x}_i)\right)\frac{U_{DC}}{100V} + \left(\vec{E}_{100}(\vec{x}_i) - \vec{E}_0(\vec{x}_i)\right)\frac{U_{AC}}{100V}\frac{|\sin 2\pi f t|}{\sin 2\pi f t}$$

5.3.3 Influence of a conductive substrate on the jump roller

To reduce the adhesion of toner on the jump roller, and therefore to improve detachment, it has been shown that it is advantageous to coat the metal jump roller with a partly conductive substrate [BG94]. Thus the forces from the induced mirror charges (see chapter 5.7.1.1) can be reduced. However, this also influences the electric fields in the jump nip. To estimate that influence, a simple approximation is made for the narrowest part of the nip, where the roller and photoconductor surface are almost parallel: The substrate is considered to be a capacitor, filled with a dielectric substance parallel to an ohmic resistor. The development nip is modeled as an air filled capacitor. The photoconductor is assumed to be completely discharged, and is therefore on ground potential.

This leads to the circuit diagram fig. 5.6 with the elements

R_1 Resistance of the substrate, conductivity κ_1

C_1 Capacity of the substrate, permittivity $\epsilon_1\epsilon_0$, thickness d_1

C_2 Capacity of the development nip, permittivity ϵ_0, thickness d_2

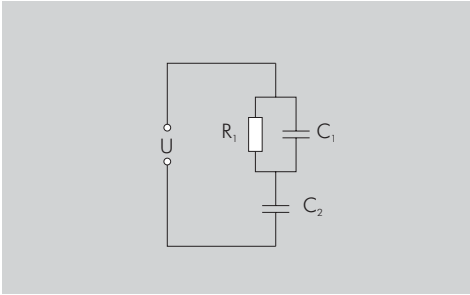

Figure 5.6: Circuit diagram

A differential equation for the voltage at the development nip $U_2(t)$ can be derived, which is only dependent from the applied voltage $U(t)$

$$(R_1C_1 + R_1C_2)\dot{U}_2(t) + U_2(t) = U(t) + R_1C_1\dot{U}(t)$$

For the following calculations, two characteristic time constants are introduced:

$$\begin{aligned} \tau_1 &= R_1C_1 = \frac{\epsilon_1\epsilon_0}{\kappa_1} \\ \tau_2 &= R_1C_2 = \frac{\epsilon_0}{\kappa_1}\frac{d_1}{d_2} \end{aligned}$$

τ_1 is the well known characteristic discharge constant of a lossy capacitor. Using these constants, the differential equation is

$$(\tau_1 + \tau_2)\dot{U}_2(t) + U_2(t) = U(t) + \tau_1\dot{U}(t)$$

If the external voltage is a superposition of a DC and an AC voltage, $U(t) = U_{DC} + U_{AC}\sin\omega t$, the voltage along the development nip is

$$U_2(t) = U_{DC}\left(1 - \frac{C_2}{C_1 + C_2}e^{-\frac{t}{\tau_1+\tau_2}}\right) + U_{AC}\sqrt{\frac{1+\omega^2\tau_1^2}{1+\omega^2(\tau_1+\tau_2)^2}}\sin(\omega t + \phi)$$

This means that after an initial peak subsides, an AC voltage is applied to the development nip. Compared to the external voltage, the field in the nip is reduced by a factor $\sqrt{\frac{1+\omega^2\tau_1^2}{1+\omega^2(\tau_1+\tau_2)^2}}$, and also has a certain phase shift ϕ, which can be neglected in this case, since the simulation does not depend on the absolute time. With these results it is possible to perform a static field calculation for the development nip without a coating, and than consider the effect of the coating by this factor.

5.4 Many-body simulation

5.4.1 Equation of motion

The most precise way to analyze the complex motion of the large number of toner particles involved in the transfer process in the development nip, is to perform a many-body simulation according to the discrete element method (DEM) [Meh94], where the equation of motion is solved for each particle . To facilitate the detection of particle contacts, all particles are considered to be perfect spheres. The orientation of the particles is not taken into account, so that only translational forces have to be calculated. The accelerating force $\vec{F}_i$ on a toner particle consists essentially of three components:

$$\begin{aligned} m_i\ddot{\vec{x}}_i &= \vec{F}_i(\vec{x}_i, \vec{x}_j, \dot{\vec{x}}_i, t) \\ &= \underbrace{\vec{f}_{el_{field}}(\vec{x}_i, t)}_{particle-field} + \underbrace{\vec{f}_{vis}(\vec{x}_i, \dot{\vec{x}}_i)}_{particle-air} \\ &+ \underbrace{\vec{f}_{mirror}(\vec{x}_i) + \vec{f}_{adh}(\vec{x}_i)}_{particle-surface} \\ &+ \underbrace{\sum_j \vec{f}_{el_{ij}}(\vec{x}_i, \vec{x}_j) + \sum_j \vec{f}_{coh_{ij}}(\vec{x}_i, \vec{x}_j) + \sum_j \vec{f}_{col_{ij}}(\vec{x}_i, \vec{x}_j)}_{particle-particle} \end{aligned}$$

1. The forces resulting from external fields:

$\vec{f}_{el_{field}}$	Electric field force due to the applied voltages and charge densities
$\vec{f}_{vis}$	Friction force due to the motion of the particle in an air flow (see chapter 4.2.3)

2. The forces resulting from contacts with the roller and the photoconductor

$\vec{f}_{mirror}$	Electric force due to the induced mirror charges on a conducting surface
$\vec{f}_{adh}$	Adhesion force near surfaces due to intramolecular interactions between particle and surface

3. The forces resulting from particle-particle interactions

$\vec{f}_{el_{ij}}$	Far-reaching electric force due to the interaction between the central charges of two particles
$\vec{f}_{coh_{ij}}$	Short-range attractive forces between two particles
$\vec{f}_{col_{ij}}$	Forces emerging from particle collisions

5.4.2 Initial configuration

For the many-body simulation of the development nip, the initial arrangement of the toner particles on the jump roller results from the previous developer station calculations (see chapter 4.3). The thickness of this initial layer conforms with the results from the white-light interference thickness measurements (see 2.14). The initial particle velocity is chosen so that the particles are moving uniformly with the jump roller.

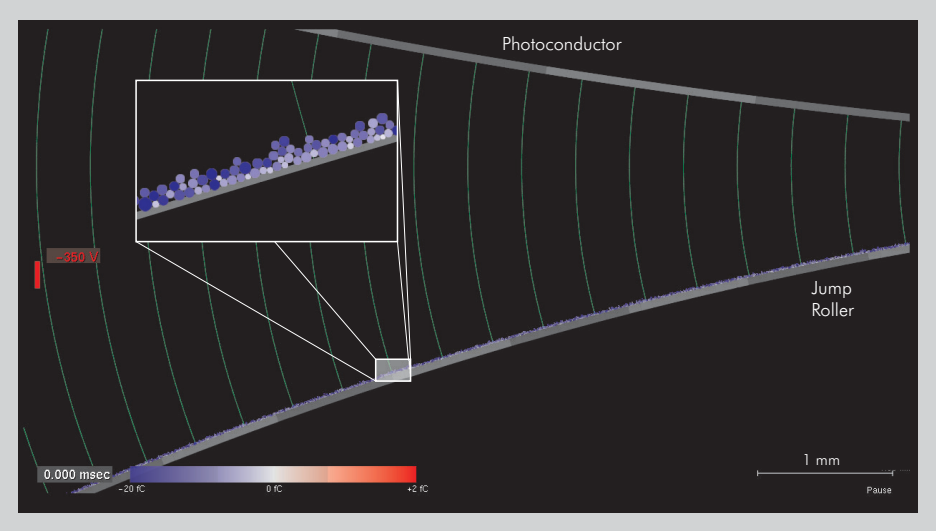

Figure 5.7: Initial configuration for 10000 toner particles

5.5 Electric field-induced forces $\vec{f}_{el_{field}}$

The force on a charge in an electric field is well-defined. The problem is that the charge on a toner particle is arranged in a complex pattern. Due to the triboelectric charging process and the irregular form of the toner particles, only small toner areas are actually in contact with the much larger carrier particles. Measurements have shown that the charge density on the toner is highest in these areas [CY02, NST98, Hay88]. This charge distribution will be important not only for the electric field force, but also for the mirror forces near the rollers and the particle-particle forces. For each of these forces, a model for the complex charge pattern has to be chosen to perform a correct simulation:

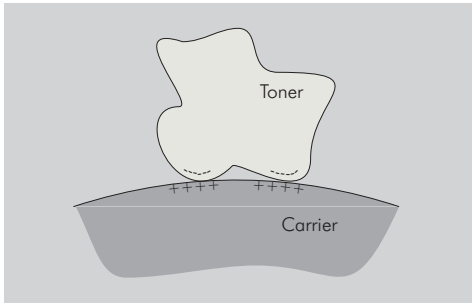

Figure 5.8: Result of triboelectric charging process

Point charge centered in toner particle In the simplest model, the whole particle charge is assumed to be localized in a point charge at the geometric center of the particle. The force is then

$$\vec{f}_{el_{field}}(\vec{x}_i, t) = q_i \vec{E}(\vec{x}_i, t)$$

where q_i is the charge of the particle according to the charge distribution from chapter 2.

Uniformly charged dielectric sphere More realistically, the toner is considered to be a homogeneously charged dielectric sphere, as proposed by Hays [Hay95]. This results in a force

$$\vec{f}_{el_{field}}(\vec{x}_i, t) = \chi q_i \vec{E}(\vec{x}_i, t) - \gamma \pi \epsilon_0 d_i^2 \left|\vec{E}(\vec{x}_i, t)\right| \vec{E}(\vec{x}_i, t)$$

where χ and γ are correction factors (1.6 and 0.063, respectively, for $\epsilon_{Toner} = 4$) and d_i is the diameter of the particle.

In this case, an additional surface charge is created by polarization [Flü86]

$$\sigma = \frac{3}{4\pi} \frac{\epsilon_{Toner} - 1}{\epsilon_{Toner} + 2} E \cos\theta$$

which has to be considered later with the particle-particle interaction.

Irregularly formed particle with inhomogeneous charge distribution The most important effect of considering a realistic charge distribution would be the occurrence of additional torques on the particle emerging due to field gradients.

Summary To reduce the numeric effort, the model of a homogeneously charged dielectric sphere was chosen. The integral force on the particle is sufficiently approximated, while the loss of information about the orientation of the particle does not influence the deposition significantly.

5.6 Friction force $\vec{f}_{vis}(\vec{x}_i, \dot{\vec{x}}_i)$ due to the particle motion in air flow

The friction force on the toner particle due to the viscous air is calculated the same way as for the carrier particle in chapter 4.2.3. The Reynolds number is still low enough, so that Stokes' Law can be used to calculate the force depending on the position $\vec{x}_i$ and the velocity $\dot{\vec{x}}_i$ of the particle:

$$f_{vis}(\vec{x}_i, \dot{\vec{x}}_i) = -6\pi\eta_{air} r_i (\dot{\vec{x}}_i - \vec{v}_{air}(\vec{x}_i))$$

where η_{air} is the dynamic viscosity of air ($17.2\,\mu Pa \cdot s$) [Kuc91].

5.7 Boundary-related forces

5.7.1 Electric field force $\vec{f}_{mirror}$ caused by induced mirror charges

Since both the jump roller and the backside of the photoconductor are conductive, any charge near these two surfaces will induce opposite charges so that the potential along the surfaces remains constant. The induced charges on the potential surfaces can be replaced by the well-known mirror charges [Flü86]. Since there are two potential surfaces, each mirror charge has to be mirrored on the other surface, thus creating an infinite series of mirror charges. However, the calculation of the forces these mirror charges exert on the toner shows that only

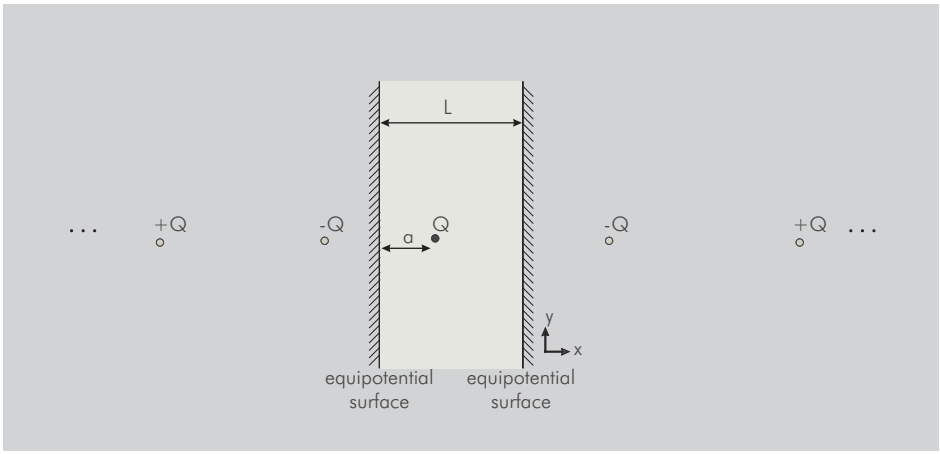

Figure 5.9: Mirror charges on two mirror surfaces

the first mirror charge on the nearest surface yields a significant amount to the total force ($f_{first-mirror-charge}/f_{second-mirror-charge} \approx 10^3$) since the distance Lbetween the two surfaces is much larger than the diameter of a typical toner particle.

The problem here is to find an approximation for the complex charge pattern of the toner, so that the resulting mirror forces model the observed behavior near surfaces correctly. As this is a fundamental problem for the understanding of toner detachment, many different approaches can be found in literature.

5.7.1.1 Homogeneously charged sphere near a conductive plane

In the most simple case, one assumes a homogeneously charged sphere resting on a conductive plane. The resulting mirror charges would be equal to those resulting from a point charge in the middle of the sphere with radius R. The force is then [GV93]

$$F_{mirror} = \frac{1}{4\pi\epsilon_0}\frac{q^2}{(2R)^2}$$

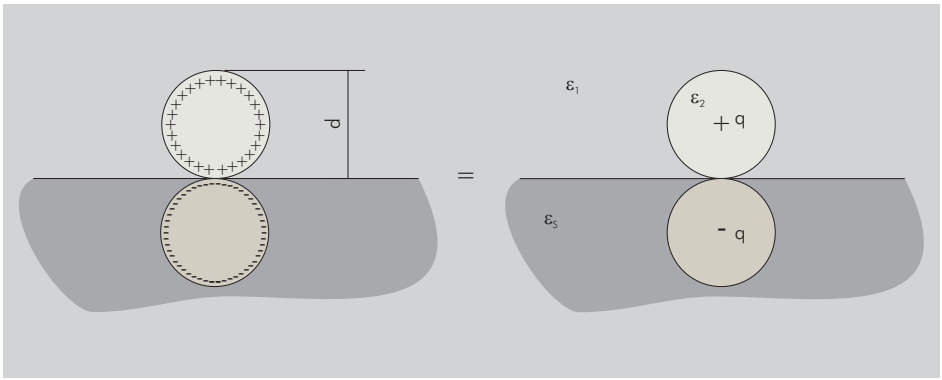

Figure 5.10: Homogeneously charged, non-polarizable sphere resting on a conductive plane

The problem with this model is that the resulting forces are far below the measured ones. The calculations results in forces between $0.1 \ldots 20nN$ for the toner used here, compared to

$150 \ldots 500nN$ measured with the centrifuge (see fig. 2.8). This means that some characteristic effects are not correctly modeled. Therefore, the following approaches concentrate mainly on remodeling the charge distribution and the material properties of toner and substrate.

Considering the different material properties for a sphere (ϵ_2) resting in a medium (ϵ_1) on a dielectric substrate (ϵ_s) under the influence of an external field E_0, leads to a refined expression for the mirror force [Fen98, FH98, Hay88] :

$$F_{mirror} = \alpha \left(\frac{q^2}{16\pi\epsilon_1 R^2} \right) - \chi q E_0 + 4\gamma\pi\epsilon_1 R^2 E_0^2$$

where the three components represent the mirror forces, coulomb forces and multipolar dielectrophoretic forces

For $\epsilon_1 = \epsilon_2$, this yields

$$\alpha = \frac{\epsilon_s - \epsilon_1}{\epsilon_s + \epsilon_1}$$

In the more general case $\epsilon_1 \neq \epsilon_2$, additional correction factors have to be introduced which can be calculated only numerically:

$$\begin{aligned} \alpha &= \alpha'(\epsilon_s, \epsilon_1, \epsilon_2) \frac{\epsilon_s - \epsilon_1}{\epsilon_s + \epsilon_1} \\ \chi &\approx 1 + \frac{1}{2} \left[\frac{\epsilon_s - \epsilon_1}{\epsilon_s + \epsilon_1} \right] \left[\frac{\epsilon_2 - \epsilon_1}{\epsilon_2 + 2\epsilon_1} \right] \end{aligned}$$

For a toner with $\epsilon_2 = 4$, α' varies between 1..1.5, with $\epsilon_s = 1..\infty$, $\chi = 1.6$, $\gamma = 0.063$. The multipole part therefore can be neglected.

Even with this improvement, there is still an order of magnitude between the resulting forces and the experimentally measured ones. One solution would be to calculate the adhesion force of a particle not only based on its own mirror charges, but also on the ones from its neighboring particles. The total force could than be up to 6.9 times higher in a densely packed monolayer than for a single separated particle [Jon95]. If this model were valid, the detachment of one particle out of a monolayer should carry away a chain of other particles, since their adhesion would become gradually lower with each neighboring particle leaving the surface. This is a general characteristic of all models where adhesions strongly depend on neighboring particles.

However following Hays, this behavior can not be observed during microscopic investigations. This is consistent with our experiments, where the remains of toner jump experiments were analyzed: If the influence of neighboring particles were that significant, large areas should be observable where all toner particles had jumped. Quite in contrast, there were almost always large amounts of single particles observable that had not jumped.

Another approach of Fowlkes and Robinson [FR88], where the multipole expansion of the charge distribution was used to explain the higher adhesion forces lead to theoretical predictions about the force distribution that could not be validated in experiments.

5.7.1.2 Inhomogeneously charged particle near a conductive plane

The main problem with all the above mentioned models seems to be the assumption of a homogeneously charged particle. This assumption is doubted by several authors [Jon95]. The theory of an inhomogeneously charged model has been confirmed by measuring the distance-dependence of the adhesion forces [PBC96] by AFM measurements. The results could be best fitted by a patch-charge model, while a center-charge model resulted in large errors. The reason is mainly the mechanism of triboelectric charging, since a charge separation can only occur at the contact areas of toner and carrier particles as described above. Several models were

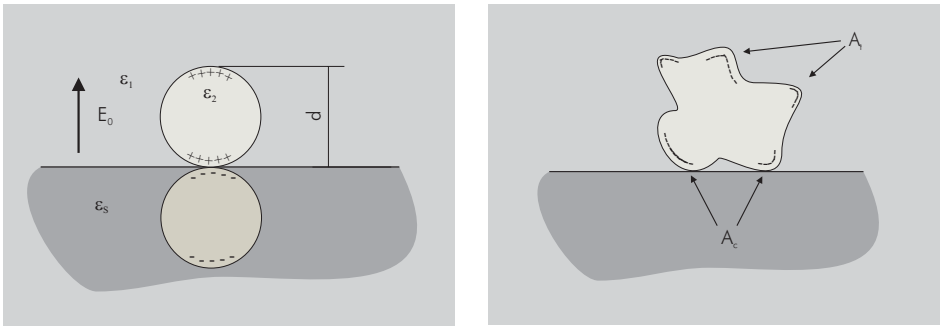

Figure 5.11: Models for inhomogeneous charge distributions: Dumb-bell (left) and irregular particle (right)

proposed to approximate the complex results of this charging process. Two of these shall be presented here as examples:

Starting from the triboelectric charge mechanism, Feng and Hays [FH00] introduced the model of a dumb-bell charge distribution (Fig. 5.11 left). The idea behind it is that toner particles which are charged on one side tend to get in contact with carrier particles on that side. Therefore, another carrier particle tends to get into contact with the opposite side of the toner (due to the diameter relation of carrier/toner: 100μm/10μm) to deposit further charges.

Once again, the mirror force can be written as

$$F_{mirror} = \alpha \left(\frac{q^2}{16\pi\epsilon_1 R^2} \right) - \chi q E_0 + 4\gamma\pi\epsilon_1 R^2 E_0^2$$

However, this time the coefficients α, χ and γ can be calculated only numerically. Since the equation is quadratic in q, two extrema can be found for the particle charge, which limit an interval wherein detachment is possible.

Another possibility to consider irregular charge densities is described by Hays [Hay95, Hay94], using real irregularly shaped particles instead of the sphere approximation (Fig. 5.11 right). This model assumes that the protrusions on the insulating particle are charged to an essentially constant surface charge density σ. The total charged area, A_t, on the particle represents a small fraction of the toner surface area. The sum of the charged areas in close proximity to the conducting surface is A_c. If the extent of a charged area in contact with the substrate is much larger than the average distance between the charged surface and a conductive substrate, the magnitude of the electrostatic force of adhesion can be expressed as

$$F_{mirror} = \frac{\sigma^2 A_c}{2\epsilon_0}$$

By considering an additional non-electrostatic adhesion contribution, which is also proportional to A_c, the total adhesion force is

$$F_{adh} = \frac{\sigma^2 A_c}{2\epsilon_0} + W A_c = Q f \left[\frac{\sigma}{2\epsilon_0} + \frac{W}{\sigma} \right]$$

where $f = A_c/A_t$ is the area ratio of the relevant charged area to the total charged area. This parameter can be used to fit the model to existing measurements.

5.7.1.3 Mirror force simulation model

Since no convincing model consistent with all experimental results was found that was generally accepted, a more pragmatic approach was chosen: As the most simple model, the central

charge model does not reproduce the experiments correctly, a slightly more elaborate model was selected where the surplus charge of the particle is split into two point charges (see fig. 5.12). This yields several advantages:

- The model can be seen as a more abstract dumb-bell model, thus giving some physical motivation.
- By adjusting the distance a between the two point charges, the value for the mirror force can be fitted to confirm with the experimental measurements ($a/d \approx 0.7$).
- The numeric effort consists only of summing up the four coulomb interactions and remains therefore controllable

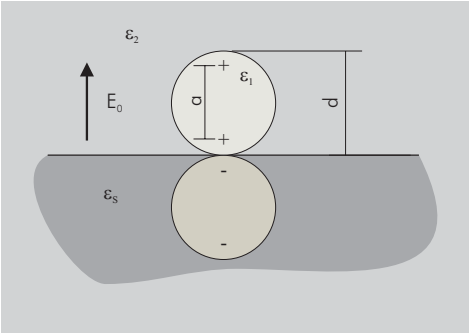

Figure 5.12: Simplified dumb-bell model

5.7.2 Non-electrostatic adhesion force $\vec{f}_{adh}(\vec{x}_i)$ near surfaces

5.7.2.1 Theory

Even completely discharged particles experience an attractive force when they are in contact with a substrate, as the centrifuge measurements showed. These forces are mainly van-der-Waals forces, resulting from interactions between dipoles and induced dipoles. For the simple case of a sphere and a plate, they can be calculated following the microscopic approach of Hamaker [Ham37], or the macroscopic approach of Lifshitz [Lif56]. For a distance $a \ll R$, where R is the radius of the particle, the Hamaker approach results in

$$F_{vdW} = \frac{A_{12} R}{6a^2}$$

where A_{12} is the Hamaker constant for a sphere of medium 1, resting on a substrate of medium 2. The distance a for contact is typically assumed to be 0.4 nm [FT98, VB98, Hay95], resulting from the length of a typical covalent bond of about 0.2 nm [BP83]. With this assumption and an appropriate Hamaker constant, F_{vdW} for a 5 μm toner particle is about 200 nN, which is roughly twice as much as the centrifuge measurements suggest. The discrepancy can be explained by the fact that the toner particles used here are not spherical due to their melt-grind process technology, so that the radii of the toner edges in contact with the surface are significantly smaller than the whole particle radius. Furthermore, sub-micrometer silica particles are added to the toner resin because of their known ability to reduce adhesion forces [GQR99].

5.7.2.2 Experimentally established dependencies

From the centrifuge measurements, as well as from other published measurement results some fundamental dependencies can be found for the non-electrostatic adhesion forces. These dependencies conform well with the theory that the measured forces originate mainly from van-der-Waals forces:

- Adhesion force rises with particle size [FT98]
- Distribution is narrower for smaller particles [FT99]
- Adhesion force is higher for spherical toner (chemically-produced) than for melt-grind toner
- Adhesion force decreases with an increasing concentration of sub-micrometer silica particles on the surface of the toner [GQR98, IKY99]

5.7.2.3 Simulation model

The adhesion force value for the particles in contact with a roller or the photoconductor is chosen so that they fit to the results of the centrifuge measurements, i.e. the forces of a diameter class follow a Gaussian distribution around a mean value that is proportional to the diameter.

Van-der-Waals forces are only in effect at very short distances between particle and boundary, since retardation effects become relevant from distances as low as 5 nm [Hun95]. Therefore, the dependency of the adhesion force from the distance to the surface is assumed to be proportional to $\frac{1}{r^2}$.

5.8 Particle-particle interactions

5.8.1 Electric field forces $\vec{f}_{el_{ij}}$ due to particle-particle interaction

The force between two point charges q_i and q_j is described by Coulomb's law

$$\vec{f}_{el_{ij}}(\vec{x}_i, \vec{x}_j) = \frac{q_i q_j}{4\pi\epsilon_0 \left|\vec{x}_i - \vec{x}_j\right|^3}(\vec{x}_j - \vec{x}_i) \tag{5.1}$$

So the total force on one particle resulting from the other charged particle would be simply the sum

$$\vec{f}_{el_i} = \sum_j \vec{f}_{el_{ij}}(\vec{x}_i, \vec{x}_j)$$

However, since all the simulated particles are in a two-dimensional plane (see figure 5.13) to reduce computation time, this formula neglects the influence of all the particles in front of or behind the simulation plane ($\vec{x}_j - \vec{x}_i = \begin{pmatrix} \Delta x \\ \Delta y \end{pmatrix}$).

One way to approximate that influence is to consider the particle q_j as a series of particles, ranging from $z = -\infty \ldots \infty$. This changes (5.1) to

$$\vec{f}_{el_{ij}}(\vec{x}_i, \vec{x}_j) = \sum_{k=-\infty}^{\infty} \frac{q_i q_j}{4\pi\epsilon_0 \sqrt{\Delta x^2 + \Delta y^2 + (k \cdot d_j)^2}^3} \begin{pmatrix} \Delta x \\ \Delta y \\ k \cdot d_j \end{pmatrix}$$

Unfortunately, this method has the disadvantage of being computationally costly, as a high number i has to be chosen to approximate the summation correctly. A more effective way is

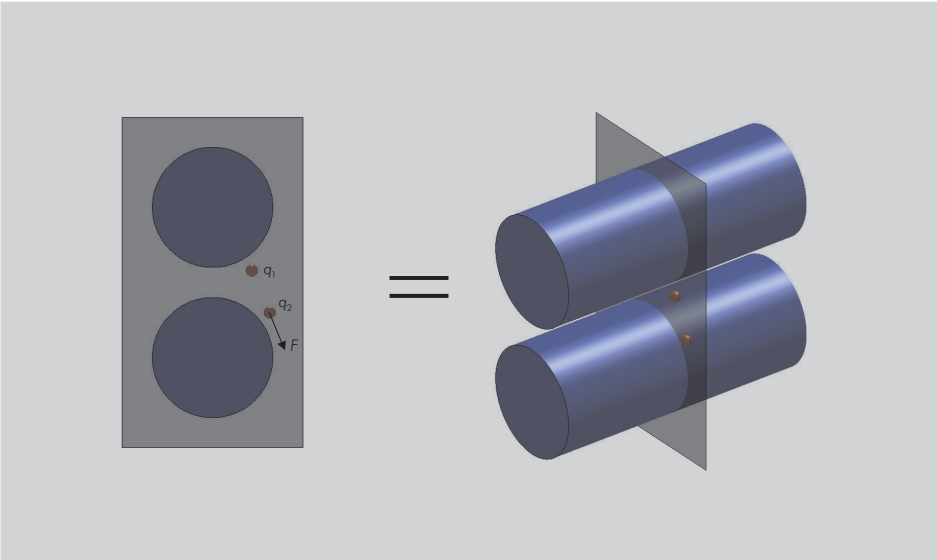

Figure 5.13: Coulomb force, 2D

to distribute the discrete charges of the particles uniformly along a line, so that an integration becomes possible (see fig. 5.14)

$$\vec{f}_{el_{ij}}(\vec{x}_i, \vec{x}_j) = \frac{1}{4\pi\epsilon_0} q_i \frac{q_j}{d_j} \int_{\Delta z=-\infty}^{\infty} \frac{1}{\sqrt{\Delta x^2 + \Delta y^2 + \Delta z^2}^3} \begin{pmatrix} \Delta x \\ \Delta y \\ \Delta z \end{pmatrix}$$

This integral can be solved analytically leading to

$$\vec{f}_{el_{ij}}(\vec{x}_i, \vec{x}_j) = \frac{q_i q_j}{2 d_j \pi \epsilon_0 \left(\Delta x^2 + \Delta y^2\right)} \begin{pmatrix} \Delta x \\ \Delta y \\ 0 \end{pmatrix}$$

Compared to the original correlation, the thus derived expression shows a distance dependence of $O\left(\frac{1}{r}\right)$, instead of $O\left(\frac{1}{r^2}\right)$, and a doubled force value for contact between particles.

5.8.2 Short-range cohesion forces $\vec{f}_{coh_{ij}}$

The previously gained expertise in electrophotographic printing technology has shown that it is easily possible to create thick layers of densely packed charged toner particles. Otherwise the optical density of toner on paper would be far too low. Since most of these particles are charged with the same polarity, a strong repulsive force would be expected, making it impossible to keep those thick layers stable. This behavior can be explained by assuming an additional attractive force, much stronger than the Coulomb repulsion for short distances, but decreasing rapidly for longer distances.

Two effects can account for this phenomenon: First, two particles in close vicinity will experience an attracting van der Waals force similar to a particle near a roller. Following Hamaker's approach [Ham37, Hun95] the van der Waals interaction energy for two spheres (radii r_1, r_2) at a distance $a \ll r_1, r_2$ is

$$\varphi_A = -\frac{A_{12}}{6a} \frac{r_1 r_2}{r_1 + r_2}$$

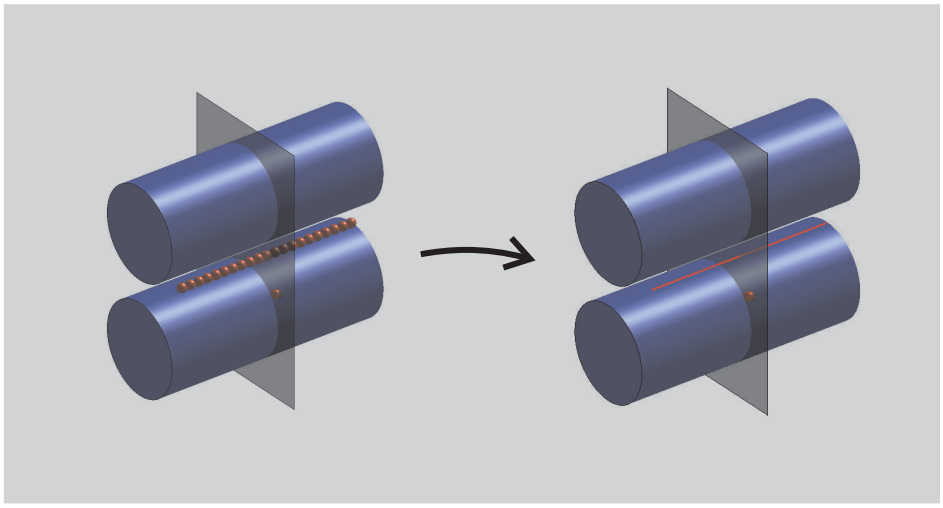

Figure 5.14: Coulomb force, pseudo 3D

compared to the interaction energy for a sphere near a plate

$$\varphi_A = -\frac{A_{12}\, r}{6a}$$

These equations make it possible to give a rough approximation of the inter-particle cohesion forces from the particle-substrate adhesion values, measured in the centrifuge.

A second effect, that can lead to attractive inter-particle forces stems from the fact, that the charge density on the particle surface is highly inhomogeneous, due to the triboelectric charging process. If it is assumed, as shown in figure 5.15, that two toner particles have a negative integral charge, but different charge densities, then it is possible for oppositely charged areas to come into contact, leading to an attraction much higher than the expected repulsion due to the integral charges.

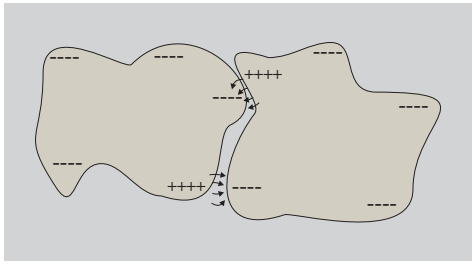

Figure 5.15: Toner cohesion

The attraction force which is exerted can be estimated, under the condition that the contact length is much larger than the contact distance, as

$$F = \frac{\sigma_C A_C}{2\epsilon_0}$$

where σ_C is the charge density in the contact area A_C.

Some attempts were made to measure the inter-particle cohesion force directly. The most promising seemed to be the usage of the AFM in combination with substrate, covered with a thick layer of toner (see chapter 2.3). A toner particle, glued to an AFM cantilever as described

in chapter 2.4.2, and lowered towards the thick toner layer will of course experience the cohesion force. The problem is that the cohesion force, like the adhesion force, is distributed over a wide range of magnitudes. This can lead to the case, that the force between the particle on the cantilever and the other particle it touches on the toner layer is so high, that it exceeds the force that keeps the other particle attached to the toner layer. Therefore, it is necessary to fix the toner layer firmly so that no particles can be removed by the AFM. The easiest way to do this is to expose the toner layer to a heat source or a solvent like acetone for a short time. Thus, the particles in the layer will start to melt and stick firmly together after solidifying. The problem is, that there is no guarantee that the particle surface of the top particle of the layer is not changed during the process (especially the arrangement of the nanometer silica particles).

So while this measuring method can be used to get an approximation of the typical magnitude of the cohesion forces, there is still a large error bound on the results. The cohesion force therefore was used as a fitting parameter to adjust the simulation results to the various experimental results (see chapter 7.1).

5.8.3 Collision incidents

5.8.3.1 Partly elastic impact of a particle on a surface

Due to the applied AC voltage, the toner particles will bounce several times back and forth between the jump roller and the photoconductor. A particle hitting a tangentially moving wall under a certain angle of incidence will be reflected partly elastic. The direction of the velocity component perpendicular to the wall will be inverted, and its amount decreased by a factor considering the partly plastic deformation. The velocity component parallel to the wall will be increased by a factor which is proportional to the relative speed between particle and wall. This proportional factor expresses the friction between the particle and the wall during the impact process.

The momentum before the impact is

$$\vec{p}_b = \vec{p}_{b_\parallel} + \vec{p}_{b_\perp}$$

If $\vec{n} = \begin{pmatrix} n_x \\ n_y \end{pmatrix}$ is the vector normal to the wall, $\vec{p}_{b_\perp}$ can be expressed as

$$\vec{p}_{b_\perp} = \frac{\vec{p}_b \vec{n}}{\vec{n}\vec{n}} \vec{n}$$

The change of the velocity of the particle due to the velocity of the wall $\vec{v}$ is

$$\vec{p}_{a_\parallel} = \vec{p}_{b_\parallel} + k \cdot \left(m\vec{v} - \vec{p}_{b_\parallel} \right)$$

where k is the above mentioned proportional factor and is in the interval $k = 0..1$. The velocity vector of the wall $\vec{v}$ can be calculated from the absolute value of the velocity v and the normal vector $\vec{n}$:

$$\vec{v} = \begin{pmatrix} \frac{1}{\sqrt{1+\left(\frac{n_x}{n_y}\right)^2}} \\ -\frac{1}{\sqrt{1+\left(\frac{n_y}{n_x}\right)^2}} \end{pmatrix} v$$

The damping due to the partly elastic deformation can be introduced by a damping factor d:

$$\vec{p}_a = \vec{p}_{a_\parallel} - d\vec{p}_{b_\perp}$$

Thus the momentum after the impact is:

$$\vec{p}_a\left(\vec{p}_b, \vec{v}, \vec{n}, d, k\right) = km\vec{v} + (1-k)\,\vec{p}_b - (1+d-k)\,\frac{\vec{p}_b\vec{n}}{\vec{n}\vec{n}}\vec{n}$$

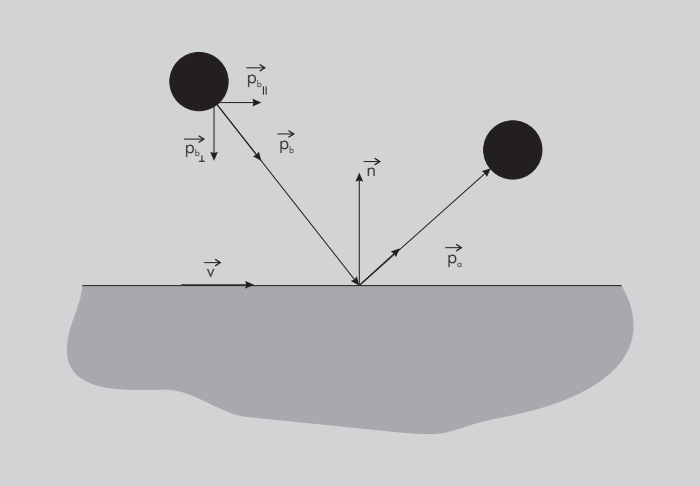

Figure 5.16: Impact particle-wall

5.8.3.2 Partly elastic particle-particle scattering

A particle-particle collision results in a deformation of both particles. Depending on this deformation, a force becomes active which drives the collision partners away from each other. Together with the short-range attractive cohesion forces described above, an oscillating system is created. Since a real system never shows completely elastic impacts, a damping factor d depending on the velocity has to be introduced to avoid non-realistic undamped oscillations.

$$F = m\ddot{x} + d\dot{x} + f\left(x\right)$$

To estimate the deformation of a toner particle, a simple model is set up: Two cubes with the volume equivalent to a toner particle are colliding at typical toner particle speed. By using Hooke's law of elongation $\frac{F}{A} = E\frac{\Delta l}{l}$, where E was set to the elastic modulus of polystyrol ($E = 3.2GPa$ [Kuc91]), the deformation Δl was found to be at about 0.1% of the total length l.

It was therefore assumed that the repulsive force $f\left(x\right)$ will be linear to the deformation, $f\left(x\right) = -kx$. The damping factor d cannot be measured easily. Therefore, it has to be fitted by comparing simulation results with experimental results (see chapter 7.2).

5.8.3.3 Fast impact between toner particles: momentum transfer

Impacts where one of the two partners has a relatively high velocity create a numerical problem: After one time step is completed, one of the two particles has already penetrated the other one to a large degree. The resulting deformation force can be very high if the centers of the two collision partners have approached to a very small distance, or very low if one particle has already passed the other one, so that it seems that one particle can pass through another one almost unhindered.

To avoid this behavior, a velocity threshold is defined. If a collision is detected and one of two particles is faster than that value, a second collision routine is executed which considers the momentum and energy transfer of the two particles as a completed process, and sets the velocity vectors to the values after an almost elastic impact.

To calculate the momentum after an impact, a system of equations is built from the conservation laws:

- Conservation of momentum:
$$\vec{p}_1 + \vec{p}_2 = \vec{p}_1\,' + \vec{p}_2\,'$$
- Conservation of energy:
$$\frac{p_1^2}{2m_1} + \frac{p_2^2}{2m_2} = \frac{p_1'^2}{2m_1} + \frac{p_2'^2}{2m_2} \tag{5.2}$$

The assumption that a momentum transfer is only possible perpendicular to the tangential plane at the impact point leads to:

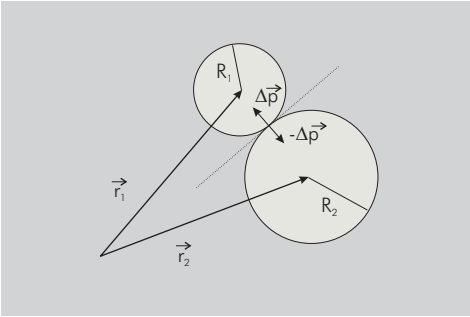

Figure 5.17: Momentum transfer

$$\begin{aligned} \Delta\vec{p} &\parallel \vec{r}_1 - \vec{r}_2 \\ \Delta\vec{p} &= k\,(\vec{r}_1 - \vec{r}_2) \end{aligned}$$

The conservation of the momentum can then be written as:

$$\vec{p}_1 + \vec{p}_2 = \underbrace{\vec{p}_1 + \Delta\vec{p}}_{\vec{p}_1'} + \underbrace{\vec{p}_2 - \Delta\vec{p}}_{\vec{p}_2'} = \vec{p}_1\,' + \vec{p}_2\,' \tag{5.3}$$

Solving the system of equations consisting of (5.2) and (5.3) leads to the solution for the momentum of the two particles after their impact:

$$\begin{pmatrix} p_{1x} \\ p_{1y} \\ p_{1z} \\ p_{2x} \\ p_{2y} \\ p_{2z} \end{pmatrix} = \begin{pmatrix} \frac{\Delta r_x^2((m_1-m_2)p_{1x}+2m_1p_{2x})+\left(\Delta r_y^2+\Delta r_z^2\right)(m_1+m_2)p_{1x}+2\Delta r_x\Delta r_y(m_1p_{2y}-m_2p_{1y})+2\Delta r_x\Delta r_z(m_1p_{2z}-m_2p_{1z})}{\left(\Delta r_x^2+\Delta r_y^2+\Delta r_z^2\right)(m_1+m_2)} \\ \frac{\Delta r_y^2((m_1-m_2)p_{1y}+2m_1p_{2y})+\left(\Delta r_x^2+\Delta r_z^2\right)(m_1+m_2)p_{1y}+2\Delta r_y\Delta r_x(m_1p_{2x}-m_2p_{1x})+2\Delta r_y\Delta r_z(m_1p_{2z}-m_2p_{1z})}{\left(\Delta r_x^2+\Delta r_y^2+\Delta r_z^2\right)(m_1+m_2)} \\ \frac{\Delta r_z^2((m_1-m_2)p_{1z}+2m_1p_{2z})+\left(\Delta r_x^2+\Delta r_y^2\right)(m_1+m_2)p_{1z}+2\Delta r_x\Delta r_z(m_1p_{2x}-m_2p_{1x})+2\Delta r_y\Delta r_z(m_1p_{2y}-m_2p_{1y})}{\left(\Delta r_x^2+\Delta r_y^2+\Delta r_z^2\right)(m_1+m_2)} \\ \frac{\Delta r_x^2((m_2-m_1)p_{2x}+2m_2p_{1x})+\left(\Delta r_y^2+\Delta r_z^2\right)(m_1+m_2)p_{2x}+2\Delta r_x\Delta r_y(m_2p_{1y}-m_1p_{2y})+2\Delta r_x\Delta r_z(m_2p_{1z}-m_1p_{2z})}{\left(\Delta r_x^2+\Delta r_y^2+\Delta r_z^2\right)(m_1+m_2)} \\ \frac{\Delta r_y^2((m_2-m_1)p_{2y}+2m_2p_{1y})+\left(\Delta r_x^2+\Delta r_z^2\right)(m_1+m_2)p_{2y}+2\Delta r_y\Delta r_x(m_2p_{1x}-m_1p_{2x})+2\Delta r_y\Delta r_z(m_2p_{1z}-m_1p_{2z})}{\left(\Delta r_x^2+\Delta r_y^2+\Delta r_z^2\right)(m_1+m_2)} \\ \frac{\Delta r_z^2((m_2-m_1)p_{2z}+2m_2p_{1z})+\left(\Delta r_x^2+\Delta r_y^2\right)(m_1+m_2)p_{2z}+2\Delta r_x\Delta r_z(m_2p_{1x}-m_1p_{2x})+2\Delta r_y\Delta r_z(m_2p_{1y}-m_1p_{2y})}{\left(\Delta r_x^2+\Delta r_y^2+\Delta r_z^2\right)(m_1+m_2)} \end{pmatrix}$$

5.8.3.4 Position after fast impact

A collision is detected using the condition

$$|\vec{r}_1 - \vec{r}_2| < R_1 + R_2$$

When this condition is fulfilled, the particles have penetrated each other already, due to the discrete time steps. This means that the collision itself happened already at an earlier time t

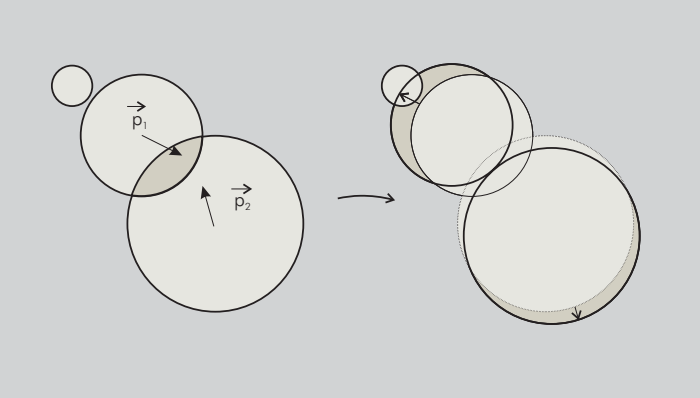

Figure 5.18: Position after fast Impact

Between two time steps the particles move approximately on straight lines

$$\begin{aligned} \vec{x}_1 &= \vec{r}_1 + t\vec{v}_1 \\ \vec{x}_2 &= \vec{r}_2 + t\vec{v}_2 \end{aligned}$$

The condition which has to be met at the time t where the collision happened is

$$\begin{aligned} |\vec{x}_1 - \vec{x}_2| &= R_1 + R_2 \\ (\Delta r_x + t\Delta v_x)^2 + (\Delta r_y + t\Delta v_y)^2 + (\Delta r_z + t\Delta v_z)^2 &= (R_1 + R_2)^2 \end{aligned}$$

The two solutions for t are:

$$t = \frac{-\Delta\vec{r}\Delta\vec{v} \pm \sqrt{(\Delta\vec{r}\Delta\vec{v})^2 - \Delta\vec{v}^2\left(\Delta\vec{r}^2 - (R_1 + R_2)^2\right)}}{\Delta\vec{v}^2}$$

5.9 Integration module

5.9.1 Higher-order methods

There are several ways of solving an ordinary differential equation. They usually all involve the reduction to a set of first-order differential equations. The simplest approach of solving such an ODE is the Euler method:

$$y_{n+1} = y_n + h \cdot f(x_n, y_n)$$

which advances a solution from x_n to $x_{n+1} = x_n + h$. The formula is asymmetrical: It advances the solution through an interval h, but uses derivative information only at the beginning of that interval. That means that the step's error is only one power of h smaller than the correction, i.e. $O(h^2)$.

Euler's method has several disadvantages in practical use. First, it is not very accurate when compared to other methods run at the equivalent step size and second, it can become unstable very easily. This can be shown for an easy example like a perfectly elastic particle bouncing on a flat surface under the influence of a constant force normal to the surface. The expected result would be a perennial series of parabolic curves, with their maxima always at the same height (when neglecting damping altogether).

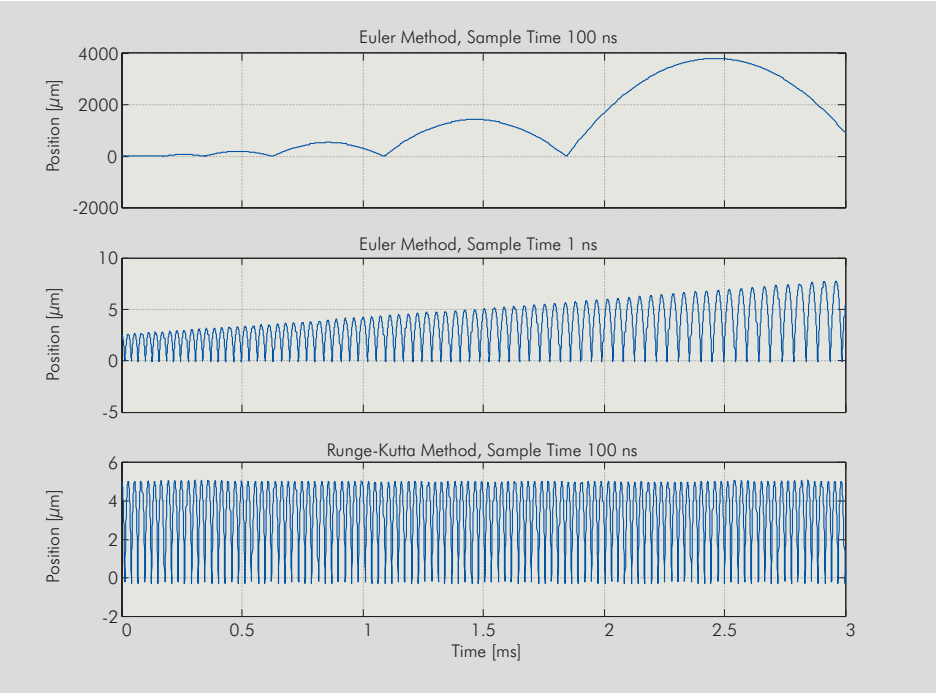

Figure 5.19: Particle bouncing calculated with different integration methods

Fig. 5.19 shows the result of the calculation done with Euler's method. The first one is calculated with a step size of 100 ns, where the result clearly becomes unstable after a few periods. The second one has been calculated with a 100 times higher accuracy, i.e. a step size of 1 ns. But even here the solution is obviously wrong, albeit nearer the physical reality then the first case. By adding a small damping factor, a seemingly realistic solution could be achieved. However, this is neither an elegant nor an efficient way, since it could never be guaranteed that the instabilities might not dominate the solution.

A better way lies in improving the integration algorithm: The reason for the inaccuracy of Euler's method lies mainly in the above mentioned asymmetry. If the formula were symmetric, it would cancel out the first-order error terms, creating a second order method. One way for such a method is to use the derivation at the starting point to make a trial step to the midpoint of the interval. Then the derivation at that midpoint can be used to compute the complete step across the whole interval. The equations for this procedure are:

$$\begin{aligned} k_1 &= h\, f\left(x_n, y_n\right) \\ k_2 &= h\, f\left(x_n + \frac{1}{2}h, y_n + \frac{1}{2}k_1\right) \\ y_{n+1} &= y_n + k_2 + O\left(h^3\right) \end{aligned}$$

The same procedure can be used to improve the integration method further: By evaluating $f\left(x, y\right)$ four times, at the starting, at two midpoints and at a trial end point one arrives at the

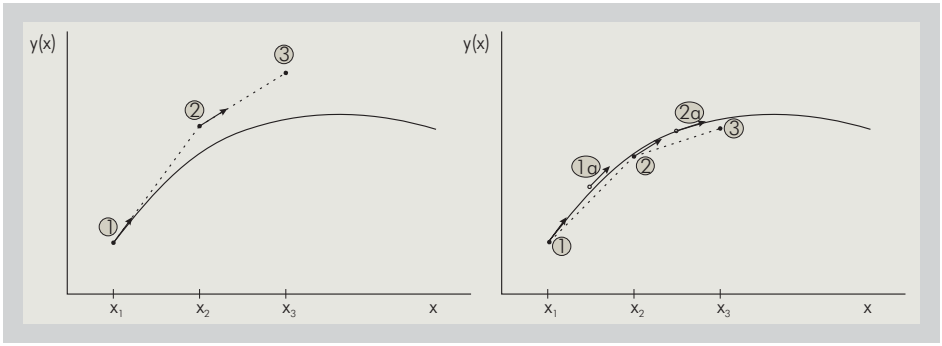

Figure 5.20: Euler vs. midpoint method

classical fourth-order Runge-Kutta formula.

$$k_1 = h\, f\left(x_n, y_n\right) \tag{5.4}$$

$$k_2 = h\, f\left(x_n + \frac{h}{2}, y_n + \frac{k_1}{2}\right) \tag{5.5}$$

$$k_3 = h\, f\left(x_n + \frac{h}{2}, y_n + \frac{k_2}{2}\right) \tag{5.6}$$

$$k_4 = h\, f\left(x_n + h, y_n + k_3\right) \tag{5.7}$$

$$y_{n+1} = y_n + \frac{k_1}{6} + \frac{k_2}{3} + \frac{k_3}{3} + \frac{k_4}{6} + O\left(h^5\right) \tag{5.8}$$

This routine is also the one which was used in the third diagram of figure 5.19, which shows the correct behavior even though the step size is 100 times larger than in the second try with Euler's method. Now, (5.8) has to be adapted to solve the second-order differential equation $\ddot{x} = f\left(\dot{x}, x, t\right)$. This results in the equations [MV91]:

$$\begin{aligned}
k_1 &= f\left(\dot{x}\left(t\right), x\left(t\right), t\right) \\
k_2 &= f\left(\dot{x}\left(t\right) + \frac{\Delta t}{2} k_1, x\left(t\right) + \frac{\Delta t}{2}\dot{x}\left(t\right) + \frac{\Delta t^2}{8} k_1, t + \frac{\Delta t}{2}\right) \\
k_3 &= f\left(\dot{x}\left(t\right) + \frac{\Delta t}{2} k_2, x\left(t\right) + \frac{\Delta t}{2}\dot{x}\left(t\right) + \frac{\Delta t^2}{8} k_1, t + \frac{\Delta t}{2}\right) \\
k_4 &= f\left(\dot{x}\left(t\right) + \Delta t\, k_3, x\left(t\right) + \Delta t\, \dot{x}\left(t\right) + \frac{\Delta t^2}{2} k_3, t + \Delta t\right) \\
x\left(t + \Delta t\right) &= x\left(t\right) + \Delta t\, \dot{x}\left(t\right) + \frac{\Delta t^2}{6}\left(k_1 + k_2 + k_3\right) \\
v\left(t + \Delta t\right) &= v\left(t\right) + \frac{\Delta t}{6}\left(k_1 + 2k_2 + 2k_3 + k_4\right)
\end{aligned}$$

For the actual software implementation, this means that the whole force calculation, which is proportional to the acceleration, has to be done four times, with different starting conditions for velocity, position and simulation time according to the above equations for k_i. Then, with the results of these four runs, the new position and velocity can be calculated, and the next time step can be started. A further speedup can be achieved by neglecting the calculation of k_3 and setting $k_3 = k_2$. This can be justified by the fact that k_2 and k_3 differ only by a slightly different velocity, while the position and simulation time are the same. Since the dependency of the total particle acceleration on the velocity is relatively weak (only the viscosity and the damping algorithm depend on the particle velocity), the error of disregarding the separate calculation of k_3 is very small.

5.9.2 Influence of discontinuous force functions

The usage of an integrator module based on predicting a function due to its derivative implies that discontinuities in the derivative, or even in the function itself, will worsen the result of the integration process dramatically. This can result in either increased error bounds or given a too large step size even in numerical instabilities, with particle behaviors completely different from the physical reality.

As a small example, the bouncing particle from above shall be simulated again. This time, the repelling force when the particle hits the wall shall be assumed as

$$F = \begin{cases} 0 & \text{for} \quad r \geq 0 \\ -\infty & \text{for} \quad r < 0 \end{cases}$$

The result is shown in figure 5.21: The apex of the particle motion is neither constant, as

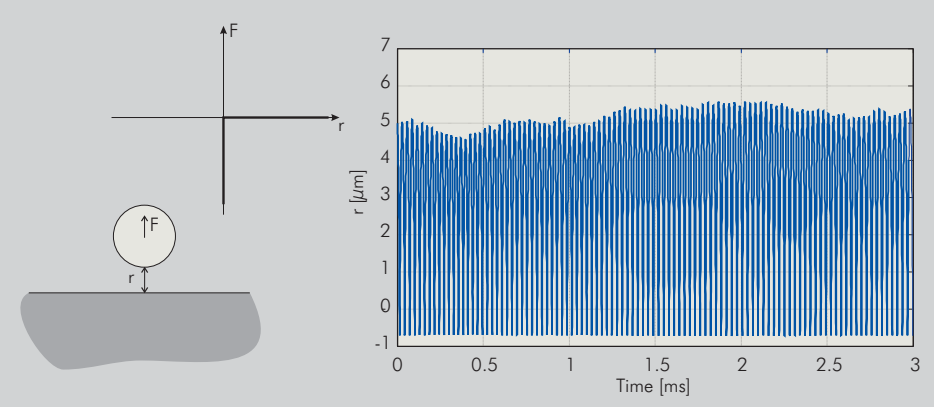

Figure 5.21: Discontinuous repelling force

could be expected from an undamped bouncing process, nor does it constantly decrease or even increase. In fact, it is tumbling around its initial value without a clear trend. This simulation was done with the 4th-order Runge-Kutta integrator introduced above.

This leads to the requirement that all force functions used have to be continuous and differentiable in time and space. The force function describing the force between two particles shown in figure 5.22 is a good example. Of course, a function like

$$F = \begin{bmatrix} f_{Coulomb}(r) & \text{for} & r > r_{coh} \\ f_{Cohesion} = +const & \text{for} & 0 < r < r_{coh} \\ -\infty & \text{for} & r < 0 \end{bmatrix}$$

would be very easy to implement and also computationally cheap, but the two discontinuities (and also the infinite force value) would result in an unpredictable numerical behavior. Therefore, a polynomial function with a pole of high order was chosen to represent the high repelling force, and a zero for $r = r_{t1} + r_{t2}$ to achieve the attracting cohesion force:

$$f(r) = k\frac{r - (r_{t1} + r_{t2})}{r^{12}} + f_{Coulomb}(r)$$

Force between toner particles Discussing the force curve between two toner particles, three different areas can be distinguished, depending on their distance :

- Deformation: If the distance is below zero, a strong backward force is acting proportional to the deformation

- Cohesion: At small distances, an attractive force acts which decreases proportional to $\frac{1}{r^{2aclmrstx}}$

- Coulomb repulsion: At larger distances, the coulomb repulsion of the toner charge dominates

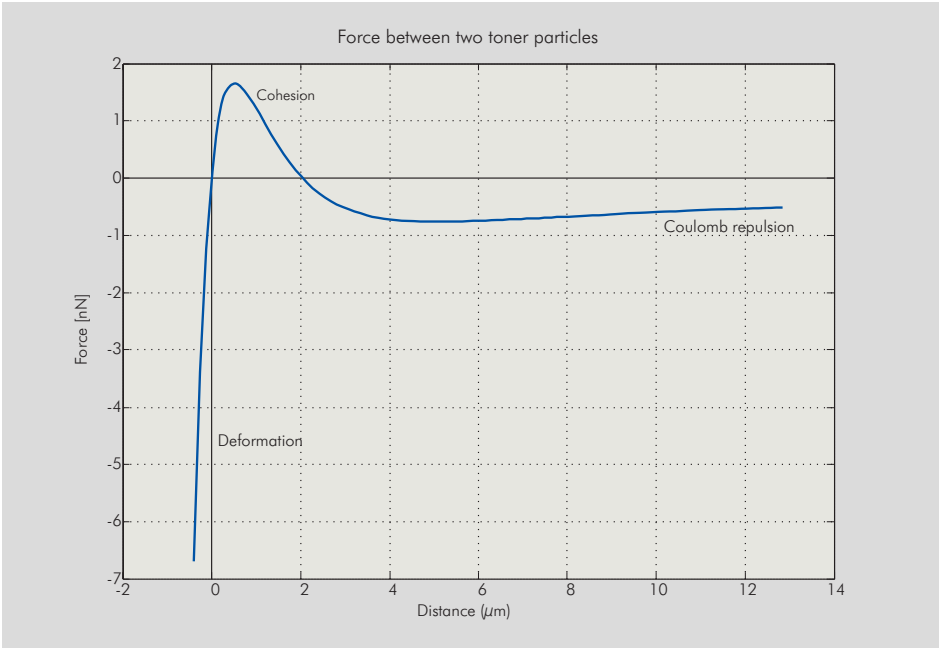

Figure 5.22: Force curve

5.9.3 Comparison of the applied forces

To get an idea of the relative magnitudes between the different forces acting on toner and carrier particles, table 5.1 lists the range of typical values

Force	Typical values	Chapter
Air-friction force on carrier	0..50 nN	4.2.3
Permanent magnet force on carrier	0..200 nN	4.2.5
Carrier-carrier magnet force	0..600 nN	4.2.6
Toner-carrier attractive force	20..100 nN	4.3
Air friction force on toner	0..5 nN	5.6
Electric field force on toner	0..75 nN	5.5
Electrostatic toner adhesion force	10..300 nN	5.7.1
Non-electrostatic toner adhesion force	10..300 nN	5.7.2
Toner-toner coulomb force	0..20 nN	5.8.1
Toner-toner cohesion force	0..40 nN	5.8.2

Table 5.1: Magnitude of forces

5.10 Summary

Figure 5.23 shows the main steps for performing the n-body simulation:

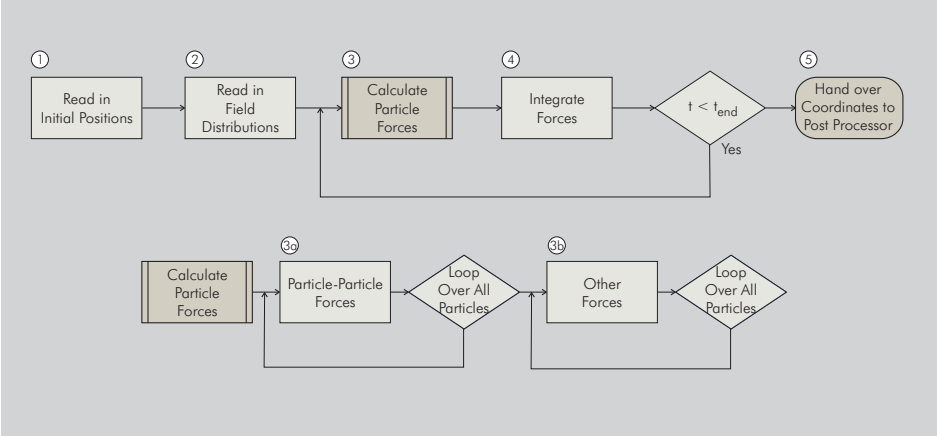

Figure 5.23: Flow chart for solving equations of motion

1. First the starting positions of the particles are read from a specified input file
2. Then the electric, magnetic and air flow field distributions from the previous FEM calculations are loaded
3. The main loop consists of summing up the forces from the particle-particle interactions and from all other sources
   (a) The particle-particle interactions use the tree algorithm described in chapter 6.5 to decide which particles can be grouped together
   (b) All other forces are only dependant on the position of the respective particle
4. From the sum of the forces, the integration module calculates the velocities and the positions
5. The positions are stored in an output file for the post processor

Chapter 6

Simulation sequence

6.1 Used software packages

After building mathematical models for the various physical processes, these models have to be evaluated numerically. Four different software packages have to be combined for a complete simulation run:

1. Treecode: Newly developed solver for the equation of motion of a large particle set, based on the Barnes-Hut tree code algorithm (see chapter 6.5). Fig. 6.1 shows some screenshots.

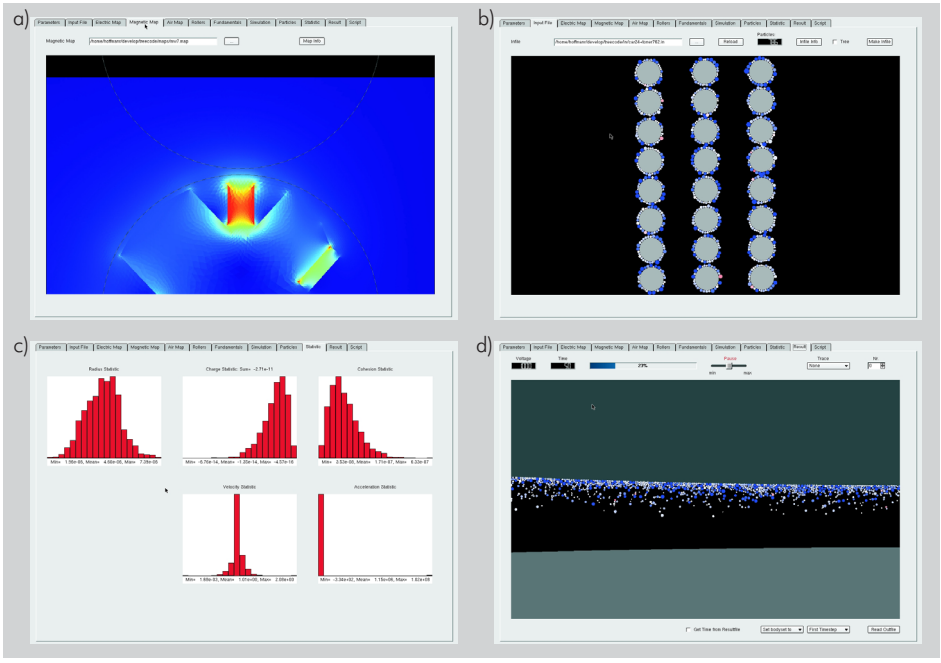

Figure 6.1: Screenshots of tree code program

The main features are:

- Runge-Kutta solver algorithm
- Multitasking-multithreaded application
- Cluster-distributed calculation using MPI

- Applicable for any number of particles (with q, m, r-distribution)
- Import of externally calculated field maps
- Display of map files (see fig. 6.1 a)
- Creation and display of initial particle configurations (see fig. 6.1 b)
- Display of particle set statistics (see fig. 6.1 c)
- Variation of particle characteristics (q, m, r, $\vec{x}$, $\vec{v}$, $\vec{a}$ during simulation run)
- New scripting language to control complex simulation sequences
- Display of current simulation state (see fig. 6.1 d)
- Export of particle coordinates as a binary file

2. Treeshow: Newly developed visualization tool based on OpenGL to display results from treecode

   - Hardware graphic acceleration support
   - Tracing of individual particles
   - Free camera motion and zoom

3. Matlab©: Integrated technical computing environment

   - Fast vectorized commands for large data amounts
   - Advanced graphics and visualization commands

4. Femlab©: Third-party add-on package for Matlab for finite element methods

   - Electrostatic
   - Magnetostatic
   - Stationary air flow

6.2 Main flow chart

Figure 6.2 shows the combination of the used software packages: From a given print pattern, the charge distribution on the photoconductor is calculated as described in chapter 3 using Matlab. With this distribution as one of the boundary conditions, the electric field in the development nip is calculated using Femlab, and stored in a data grid (see below), as well as the magnetic field and the air flow. The electric field has to be calculated once for every new print pattern, while the magnetic field and the air flow have to be recalculated if the magnetic or geometric setup has changed.

In addition to the field data the initial toner particle positions have to be calculated. As described in chapter 4.3 this is now done using the simplified stochastic deposition algorithm, which has been also implemented in Matlab.

After the grid data and the initial particle positions are stored, *treecode*, the main solver for the equation of motion starts. This is a newly developed tool written in ANSI C++ in combination with Trolltech's Qt©-library to provide a reasonable graphical user interface. The program is multi-threaded so that the actual simulation calculations are separated from the graphical i/o operations. There are no platform dependant components so that cross-platform compilation should be available with only minor changes. The main simulation platform is an Intel Linux cluster with the GNU C-Compiler gcc or the Intel C-Compiler icc. If the hardware platforms

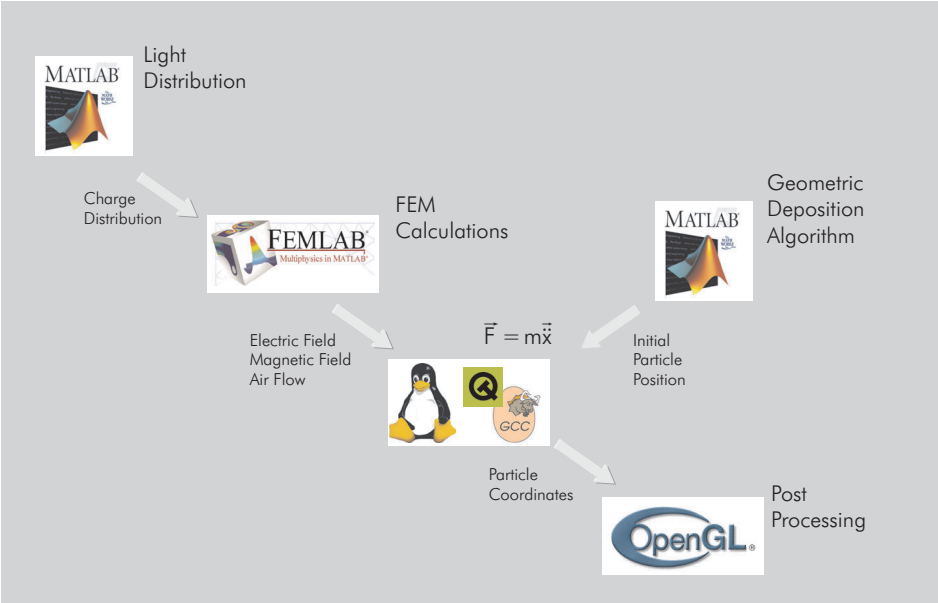

Figure 6.2: Use of the different software packages

use only Intel processors, the special optimizations used in icc can speed up the execution up to 20%. After the solver reads in the grid data at the beginning of the simulation, no further external interaction is necessary except for displaying a graphical view of the current particle positions and writing the particle positions to an output file at fixed intervals. This file consists of IEEE floating point numbers, so that the post processor needs not necessarily use the same platform as the simulation process.

The post processor *treeshow* is an OpenGL based visualization tool, which automatically uses any available accelerated graphics hardware, but can also be used with software emulation only. An animation of the simulation results can be shown with arbitrary speed, camera position and zoom window.

6.3 Parallelization

As the necessary computation time is a crucial issue for all simulations it is important to adjust the software architecture to the available hardware platform. An efficient way is to distribute the calculation load on several processor nodes by parallizing the calculation. Two different hardware architectures can be used for that purpose: Shared memory multi-processor machines, or clusters of workstations with their own memory connected by an Ethernet. It is also possible to combine both strategies, which is especially cost-effective since the most expensive components are the high-speed links. The best cost-performance ratio can be obtained by coupling dual-processor boards with fiber gigabit links (Myrinet©).

There are also two different software architectures which are commonly used for parallel programming:

- SIMD (Single Instruction stream, Multiple Data stream): SIMD refers to a parallel execution model in which all processors execute the same operation at the same time, but each processor is allowed to operate upon its own data. This model naturally fits the concept of performing the same operation on every element of an array, and is thus often associated

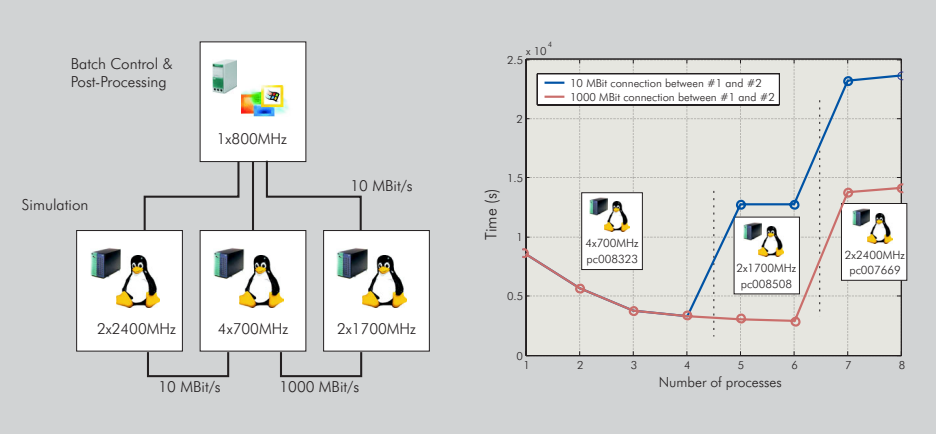

Figure 6.3: Network configuration

with vector or array manipulation. Because all operations are inherently synchronized, interactions among SIMD processes tend to be easily and efficiently implemented [SWW94].

- MIMD (Multiple Instruction stream, Multiple Data stream): MIMD refers to a parallel execution model in which each processor essentially acts independently. This model most naturally fits the concept of decomposing a program for parallel execution on a functional basis. This is a more flexible model than SIMD execution, but it is achieved at the risk of so called race conditions, in which a program may intermittently fail due to timing variations reordering the operations of one processor relative to those of others [FQG+92].

The solution chosen here was to assign each processor a subset of the whole particle set on which the different force calculations are performed, which is a classic SIMD approach. However, there is also a small MIMD component since one of the processes (slave 0 or master) has to perform some additional administrative tasks, like handling user requests, reading in the input data, distributing the particles to the other tasks, and writing the results of the calculation to the output file. Therefore the master process was constructed multi-threaded so that all the administrative tasks are executed in a different thread.

The software platform used is a standardized message passing interface (MPI). All processes communicate by sending and receiving messages, which can be either blocking or non-blocking. It does not matter whether the processes are running on the same machine or on a network-reachable machine. Another advantage of the usage of MPI was, that this library is also available on high-performance vector machines so that a porting of the code should be possible with only minor changes.

The bottleneck for this approach is the need to synchronize the results after every time step, since the force calculations even for a small subset depend on the positions of all other particles. The basic algorithm is:

1. After the program initializes, the master process distributes the position and velocity of every particle to all processes, and assigns each process its subset of the particles. The size of the subset can be chosen according to the processor speed, allowing for (static) load balancing.

2. Each process calculates the force (and thus the acceleration) for its subset, and changes the speed and position according to that acceleration.

3. Each process distributes the results for his subset to all other processes and the next time step starts.

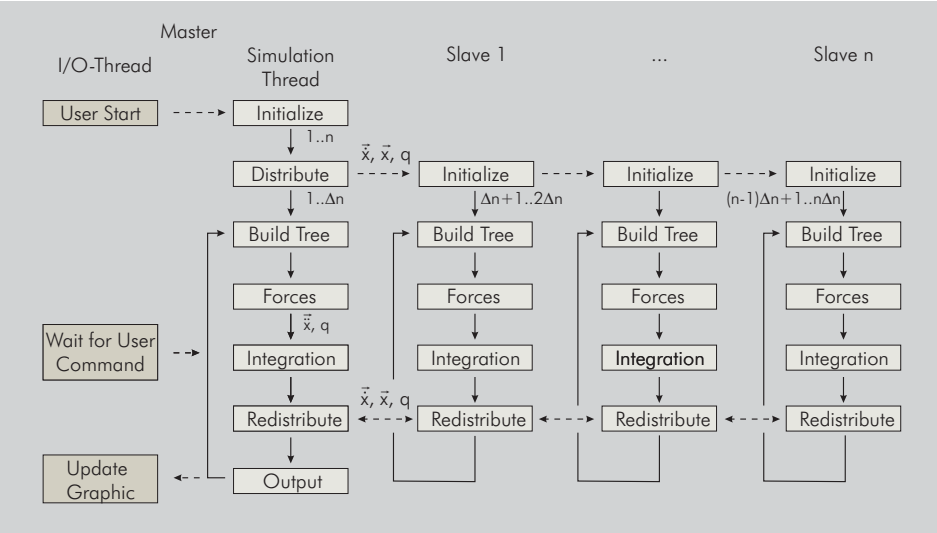

Figure 6.4: Parallelization flow chart

The components limiting the parallelization efficiency are the latency time during the inter-process communications as mentioned above, and the non parallizeable part of building the Barnes-Hut tree. Since the tree building is a complex procedure with many recursive function calls, there is no easy parallel algorithm available, despite many publications on this area [WS93, WS95a, WS95b].

In a typical simulation run of a serial treecode version, the computation time for the tree build function is about 10 % of the total computation time, so that the ratio of the non-parallizeable part t_s to the parallizeable part t_p is $\frac{t_s}{t_p} = \frac{1}{9}$. Amdahl's Law [Amd67] gives an upper limit for the speedup that can be achieved by parallization, i.e. the ratio of the necessary computation time when run on p processors $T(p)$ compared to a single processor version $T(1)$:

$$Speedup = \frac{T(1)}{T(p)} = \frac{1 + \frac{t_s}{t_p}}{\frac{1}{p} + \frac{t_s}{t_p}}$$

For p versus infinity the upper limit for the speedup is $\frac{t_p}{t_s}+1$. However, in practice, the number of processors is a tight resource so that it is important to consider how much performance gain can be expected from augmenting an additional processor. This is best expressed by comparing the computation times for p and $p+1$ processors.

$$\frac{T(p+1)}{T(p)} = \frac{\frac{t_s}{t_p} + \frac{1}{p+1}}{\frac{t_s}{t_p} + \frac{1}{p}}$$

For a serial percentage of about 10 % as measured here, Amdahl's Law suggests a reasonable upper limit of 4-6 processes for a parallel version, since any additional processor would result in a further speedup of less than 10 %. The measurements of the computation time in fig. 6.3 show, that it is more effective to start several simulation runs with different parameters than to start only one simulation that uses all available processors, since the speedup becomes only marginal if the number of processors is increased above 4. Furthermore the measurements have shown that a fast network connection is essential for grid computing over a cluster, especially for an

application like this, where large data amounts have to be exchanged between the participating processes in every time step.

6.4 Data handling

6.4.1 Grid storage

As mentioned in the previous chapters, the electric fields and the air flow are stored along a rectangular grid. To limit the amount of data, the simulation area is restricted to 8000 μm. Since the space dependency of the air flow is less then from the electric fields the resolution of the electric field grid was doubled. Similarly, the external magnetic fields do not vary much over small distances, due to the comparatively large permanent magnets. The matrices are stored and transferred between the submodules as IEEE binary files, so a data exchange between different hardware and operating system platforms is possible.

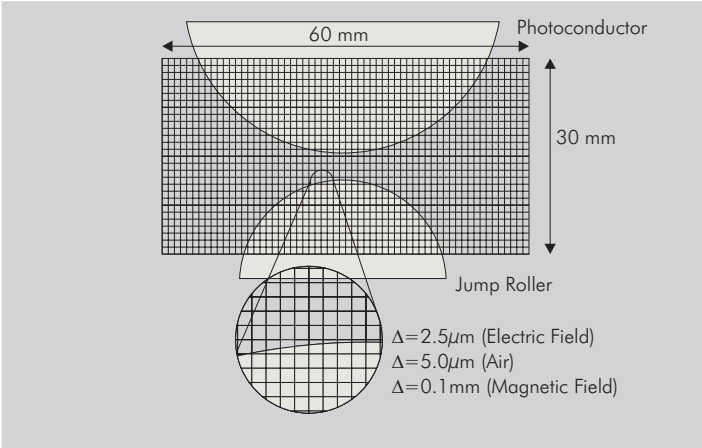

Figure 6.5: Data grid

	x_{min}	x_{max}	Δx	y_{min}	y_{max}	$y\Delta z$	File size
Magnetic field	-32mm	30mm	0.1mm	-32mm	20mm	0.1mm	15.7MB
Air flow	-40000μm	40000μm	20.0μm	-10000μm	20000μm	5.0μm	70.1MB
$(x, z) \rightarrow (u, v)$	-30000μm	30000μm	35.0μm	-10000μm	20000μm	35.0μm	24.1MB
	u_{min}	u_{max}	Δu	v_{min}	v_{max}	Δv	
$(u, v) \rightarrow (x, z)$	0.030	0.030	2.5e-6	0	200e-6	2.5e-6	60.0MB

Table 6.1: Grid Parameters

6.4.2 Interpolation of a previously calculated and stored field map

The results of the field calculations are stored on a rectangular grid. To get the values between the data points a bilinear interpolation is performed. The relative distances u and v are calculated using:

$$u = \frac{x - x_1}{\Delta x}$$

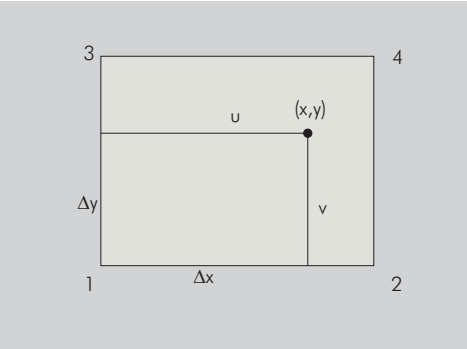

Figure 6.6: Particle position in a rectangular grid

$$v = \frac{y - y_1}{\Delta y}$$

Bilinear interpolation of the electric field yields [PA92]

$$\begin{aligned}\vec{E} = {} & (1-u)(1-v)\vec{E}_1 + u(1-v)\vec{E}_2 + \\ & (1-u)v\vec{E}_3 + uv\vec{E}_4\end{aligned}$$

where $\vec{E}_i$ is the field at the grid points $\vec{x}_i$.

6.4.3 Transformation of coordinate systems

If a correct geometric setup shall be simulated, all charge distributions on the photoconductor with a space dependency, i.e. all except for fully charged and discharged, have the problem that the electric fields in the gap vary continuously, due to the motion of the photoconductor. Therefore, the electric fields have to be calculated previously for all time steps to achieve a correct simulation, resulting in large data amounts and an equally large I/O-load.

One solution is to use a conformal mapping which transforms the parallel gap to the real curved gap. This allows to calculate the potential field in the parallel gap once, move it according to the respective time step along the parallel gap, and then transform it to the real gap. There, the electric field can be calculated from the gradient of the potential at the particle coordinates

A bipolar coordinate system fulfills these requirements. The transformation rule for bipolar coordinates (u, v) to Cartesian coordinates (x, y) is [Wol99]:

$$\begin{aligned}x &= \frac{a \sinh v}{\cosh v - \cos u} \\ y &= \frac{a \sin u}{\cosh v - \cos u}\end{aligned}$$

with $0 \leq u < 2\pi$, $-\infty \leq v \leq \infty$

The two poles are at $x = \pm a$. For $u = const$ or $v = const$, circles with the following equations are defined [Spi77]:

$$x^2 + (y - a\cot u)^2 = a^2 \csc^2 u \quad (6.1)$$

$$(x - a\coth v)^2 + y^2 = a^2 \operatorname{csch}^2 v \quad (6.2)$$

If a gap shall be modeled which is bordered by two circles with different radii, different poles have to be chosen. In this case, instead of the centers of the circles, those two points that are mapped onto themselves when mirrored at the circles have to be used as poles.

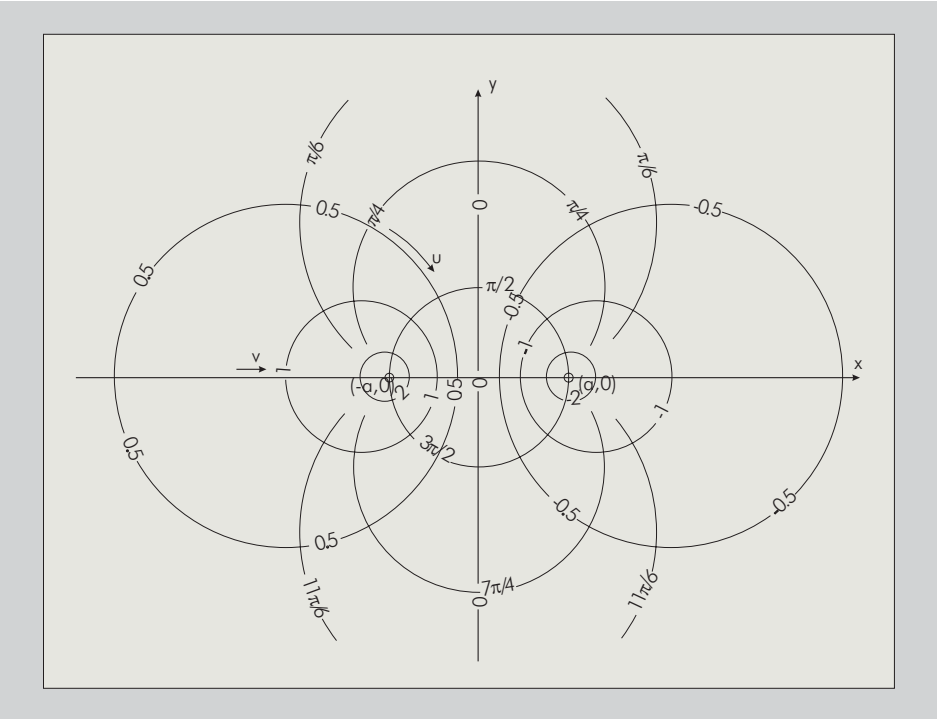

Figure 6.7: Bipolar coordinate system

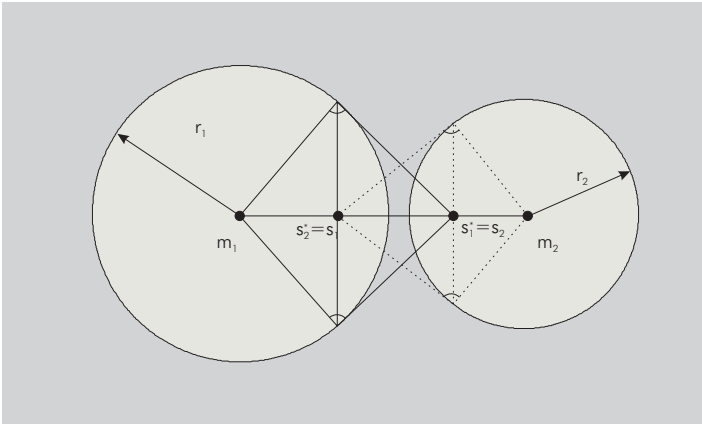

Figure 6.8: Mirror points at two circles

The mirror equations which have to be met for both points are:

$$\begin{aligned} s_1^* &= s_2 = \frac{r_1^2}{s_1 - m_1} + m_1 \\ s_2^* &= s_1 = \frac{r_2^2}{s_2 - m_2} + m_2 \end{aligned}$$

If this transformation is used on a gap, described in (u, v)-coordinates, the resulting coordinate system is not equally spaced along the circumference of the rollers. The figure 6.9 shows that the circles with $u = const$ have smaller distances at the narrowest part of the gap (for $u = \pi$), than for $u \to 0$, or $u \to 2\pi$. Also, the thus modeled parallel gap is finite (starting at $u = 0$ and ending at $u = 2\pi$), which is not desired if, for example, an infinite periodic charge distribution is to be simulated.

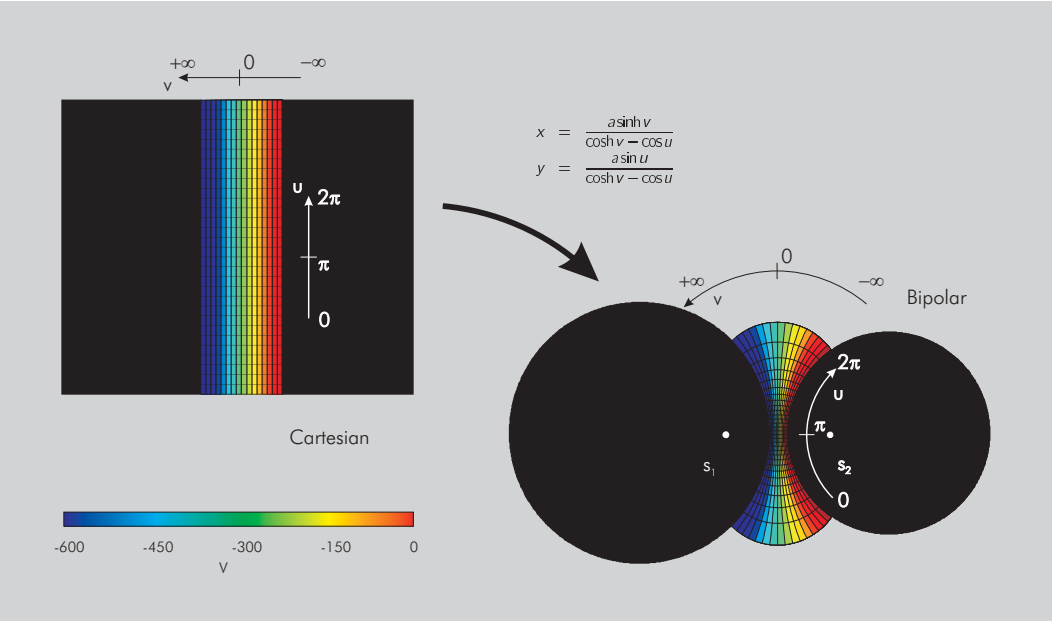

Figure 6.9: Unequally spaced transformation

To solve these two problems, an initial transformation to an intermediate coordinate system (u', v') has to be used before the actual transformation to the bipolar system. To ensure the equidistance of the coordinate transformation it is important to compare the arc length along the roller in the bipolar system to the distance along the parallel gap. The arc length can be calculated as usual as $s = \phi r$, where

$$\phi = \arctan \frac{x}{y - y_0}$$

r and y_0 can be derived from the equation for a bipolar circle with constant v (6.2).

$$\begin{aligned} r &= a \operatorname{csch} v \\ y_0 &= a \coth v \end{aligned}$$

This leads to a transformation from the gap length of the intermediate system u' to the arc length of the bipolar system s

$$\begin{aligned} s &= f(u') \\ &= a \operatorname{csch} v \arctan \frac{\sin u}{\sinh v - \coth v (\cosh v - \cos u)} \end{aligned}$$

To ensure the equidistance of the total transformation, it is important to choose the initial transformation

$$u' = g(u)$$

so that

$$s = f(g(u)) \stackrel{!}{=} u$$

Thus, an infinitely long parallel gap with $u \in]-\infty, \infty[$ is transformed to an intermediate finite gap with $u' \in [0, 2\pi[$ by

$$\begin{aligned} u' &= g(u) \\ &= f^{-1}(u) \\ &= \arccos \frac{\coth v \operatorname{csch} v \tan^2\left(\frac{u}{a}\sinh v\right) + \sqrt{1+\tan^2\left(\frac{u}{a}\sinh v\right)}}{1+\coth^2 v \tan^2\left(\frac{u}{a}\sinh v\right)} \end{aligned}$$

This gap can then be transformed to a bipolar system, where the circular arcs for $u' = const$ end with equal distances at the roller surfaces.

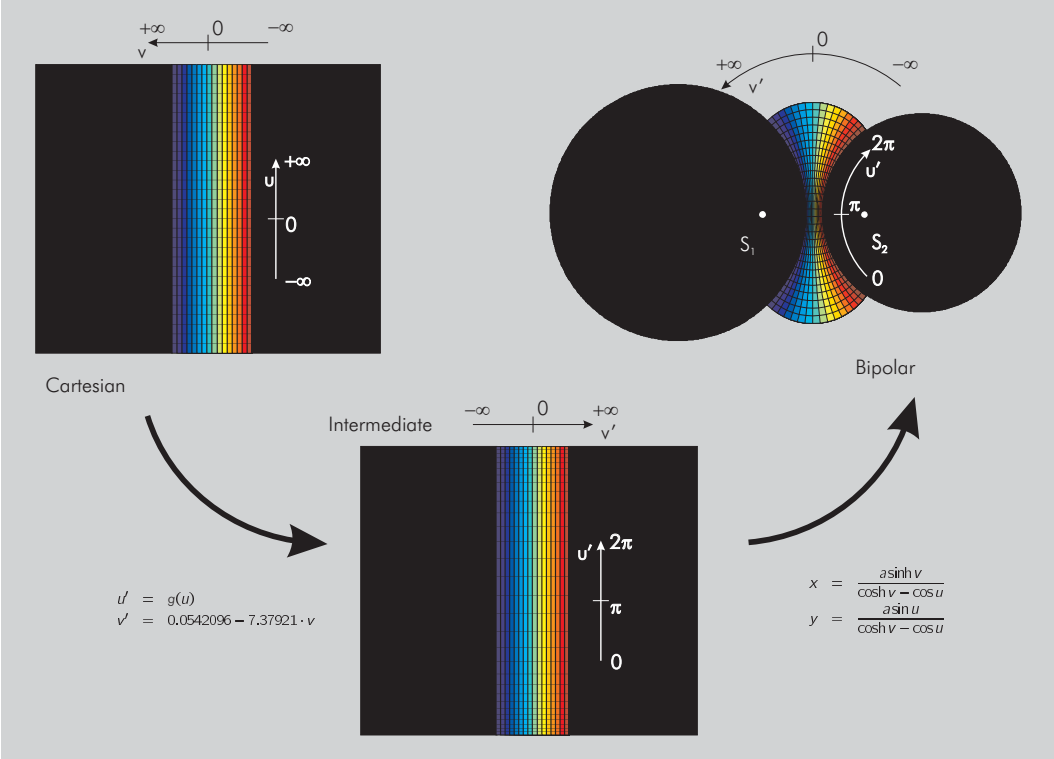

Figure 6.10: Equally spaced transformation in two steps

To calculate the electric field at a certain point, a plane has to be fitted through the potential values of the nearest points of the bipolar system whose gradient is the electric field at that point.

For this purpose, the coordinates of the 4 grid points have to be transformed to Cartesian coordinates. The general plane equation is

$$U(x, y) = ax + by + c$$

The three parameters have to be chosen so that the medium quadratic distance of the plane $U(x, y)$ from the voltage U at the grid points is minimal

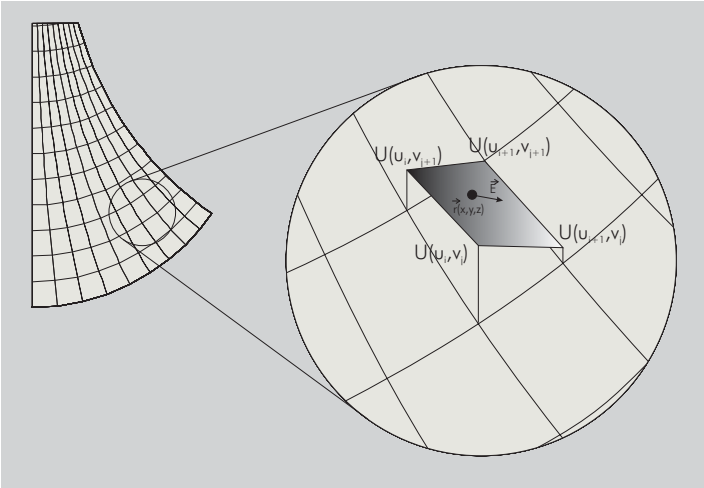

Figure 6.11: Field approximation

$$S = \sum \left(U\left(x, y\right) - U\right)^2 \stackrel{!}{=} Min \tag{6.3}$$

Forming the partial derivatives of 6.3

$$\frac{\partial S}{\partial a} = 0,\ \frac{\partial S}{\partial b} = 0,\ \frac{\partial S}{\partial c} = 0$$

leads to a system of equations [Sch92]

$$\begin{aligned} a\sum x^2 + b\sum xy + c\sum x &= \sum xU \\ a\sum xy + b\sum y^2 + c\sum y &= \sum yU \\ a\sum x + b\sum y + cN &= \sum U \end{aligned}$$

With these, the parameters a and b can be determined (c is not necessary as only the derivation of the potential $U\left(x, y\right)$is needed)

$$\begin{pmatrix} a \\ b \end{pmatrix} = \begin{pmatrix} \frac{\sum xU\left(\sum y\right)^2 + N\sum xy\sum yU - \sum x\sum y\sum yU - N\sum xU\sum y^2 - \sum xy\sum y\sum U + \sum x\sum y^2\sum U}{N\left(\sum xy\right)^2 - 2\sum x\sum xy\sum y + \sum x^2\left(\sum y\right)^2 + \left(\sum x\right)^2\sum y^2 - N\sum x^2\sum y^2} \\ \\ \frac{N\sum xy\sum xU - \sum x\sum xU\sum y + \left(\sum x\right)^2\sum yU - N\sum x^2\sum yU - \sum x\sum xy\sum U + \sum x^2\sum y\sum z}{N\left(\sum xy\right)^2 - 2\sum x\sum xy\sum y + \sum x^2\left(\sum y\right)^2 + \left(\sum x\right)^2\sum y^2 - N\sum x^2\sum y^2} \end{pmatrix}$$

These two parameters are equivalent to the electric field in x- and y-direction

$$\vec{E} = -\mathrm{grad}U = \begin{pmatrix} E_x \\ E_y \end{pmatrix} = \begin{pmatrix} -a \\ -b \end{pmatrix}$$

With these equations, all fundamental steps which are necessary during the simulation are described (see figure 6.12):

1. The simulation itself is calculated only in Cartesian coordinates, as always, therefore only (x, y, z)-coordinates are available for the toner particles.

2. The transformation from Cartesian to bipolar coordinate cannot be carried out analytically, since the above equations cannot be inverted. Thus, a table was calculated numerically, which lists the respective bipolar values for a narrow grid of Cartesian coordinates. This grid is now searched for the nearest 4 sampling points.

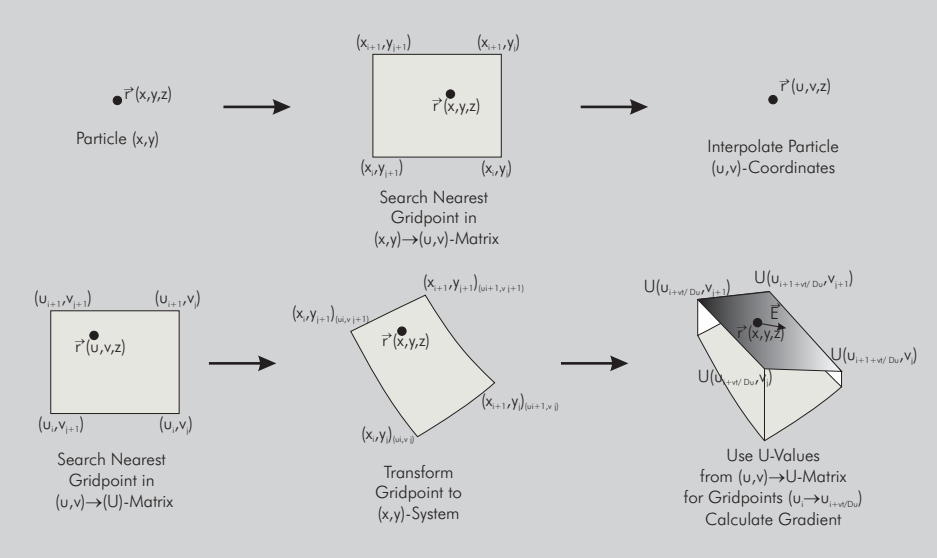

Figure 6.12: Bipolar transformation steps

3. The bipolar coordinates of the toner particle are calculated using bipolar interpolation from the 4 values from step 2.

4. The potential values in the bipolar system are also stored along a rectangular grid in (u, v)-coordinates. The nearest 4 grid points are calculated and

5. transformed to Cartesian coordinates. Analytical formulas are available for this transformation, but since it only has to be done for the coordinates where the potential values are stored, the (x, y)-coordinates for the grid points are once calculated and also stored in the file for the potential values.

6. If the boundaries were not moving, the potential values of the respective grid point could be used directly. If the field moves, however, a potential value has to be chosen according to the velocity of the boundaries and the simulation, which lies farther to left in the matrix. Through these potential values, a plane can be fitted as described above, whose gradient determines the field at the position of the particle.

This process offers the possibility to calculate field geometries with inhomogeneous charge distributions only once in the (u, v)-system, and then model the time variance by shifting the geometry in u-direction, and transform it to the (x, y)-coordinate system. Therefore the tedious field calculation is not necessary during the simulation process itself, enabling a dramatic improvement of simulation speed.

The figure 6.13 shows the example of the potential distribution of an edge at several time steps. These were simply calculated by using the transformation rule three times, where the original distribution was just shifted sideways before the transformation.

This configuration shows another advantage of the transformation process: By calculating the field in the (u, v)-system at a certain distance left and right from the edge, the field is the same as with a completely exposed or unexposed plane (i.e. charged and discharged). This area does not have to be stored completely in the matrix. The area near the edge, where the potential changes significantly, is sufficient. The areas far left and far right can be considered by calculating one column of u-values, which can then be multiplied.

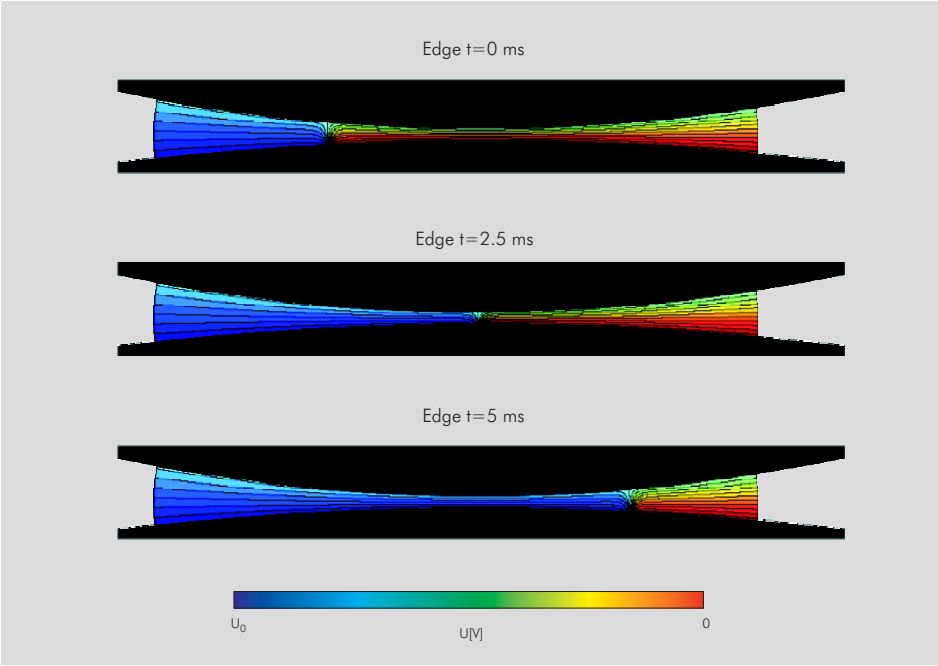

Figure 6.13: Time variance of the potential at an edge

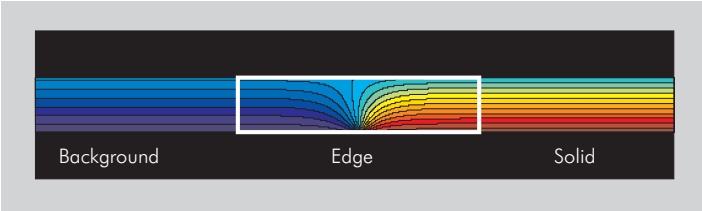

Figure 6.14: Partly calculated and stored edge

To test the correctness of the process, the jumping of a single particle to a completely discharged area is simulated. This jump process can be calculated both in a bipolar and a Cartesian coordinate system, since the photoconductor is discharged homogeneously, and therefore the motion of the photoconductor does not cause a time-variance of the electric field. The result from these two calculations can be seen in figure 6.15: The position where the particle is detached from the jump roller and also the time till deposition on the photoconductor, are comparable. An exact match was not to be expected, due to the many approximations made, and is also not necessary since the aim of this simulation is not an exact quantitative description of the motion of each particle, but a modeling of the qualitatively relevant (and observable) parameters.

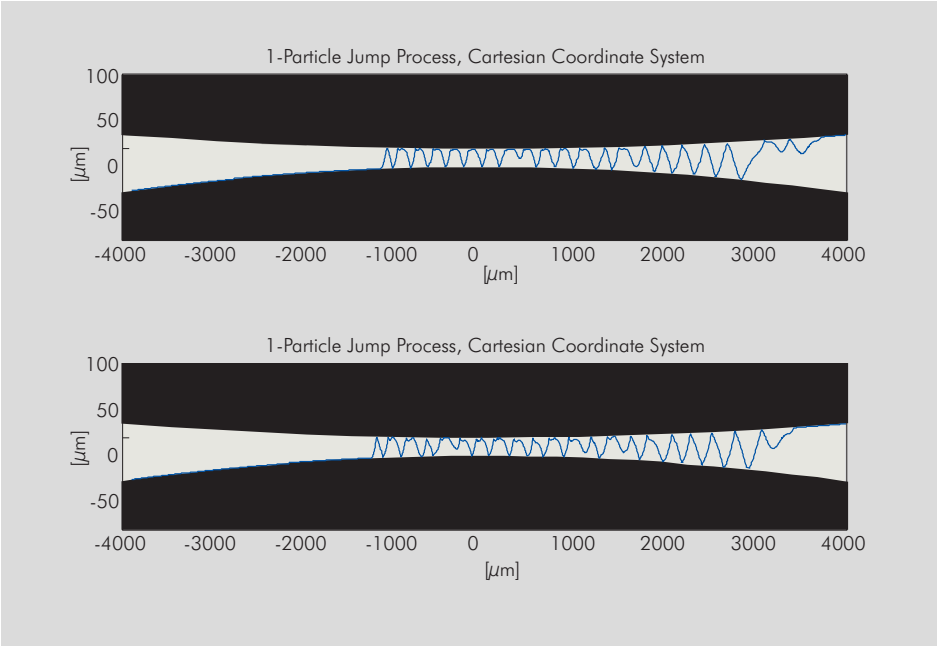

Figure 6.15: Comparison Cartesian/bipolar calculation

6.5 Hierarchical tree code

A general problem of all many-body simulations with far-reaching particle-particle interactions, like astrophysics or particle accelerators is, that the calculation cost rises asymptotically as $O\left(N^2\right)$, since the force on each particle depends on all other particles. This is also a problem for the toner simulation conducted here: The most obvious method to calculate the electric force due to the charge of the rest of the particle set is to sum up the coulomb force for every particle pair i-j, resulting in the $O\left(N^2\right)$-dependency:

$$\sum_j \vec{f}_{el_{ij}}(\vec{x}_i, \vec{x}_j) = q_i \sum_j \frac{q_j}{2d_j\pi\epsilon_0 \left|\vec{x}_i - \vec{x}_j\right|^2}(\vec{x}_j - \vec{x}_i)$$

Much effort has been expended to reduce the computational complexity of such simulations, while retaining acceptable accuracy. Several methods have been introduced which allow n-body simulations to be performed in much less time than $O\left(N^2\right)$. They all have in common the use of a truncated expansion to approximate the contribution of many bodies with a single interaction. The one used here originated in 1986 from Josh Barnes and Piet Hut [BH86].

The basic idea of an N-body algorithm based on a truncated series approximation is to partition an arbitrary collection of bodies in such a manner that the series approximation can be applied to the pieces, while maintaining sufficient accuracy in the force on each particle. In general, the methods represent a system of N bodies in a hierarchical manner by the use of a spatial tree data structure. Aggregations of bodies at various levels of detail form the internal nodes of the tree, and are called cells.

The creation of a simple Barnes-Hut tree is illustrated in figure 6.16: The first step is to define the spatial extent of the problem. The Barnes-Hut approach to this aspect of the problem is to make the problem space a rectangular. The length of the sides is the maximum spatial extent of the particles in any spatial dimension. For example, in two dimensions, the initial problem space is a square whose side is the maximum distance between particles in either of the two dimensions. Similarly, the problem space in three dimensions is a cube whose side is the greatest particle distance in any of the three spatial dimensions.

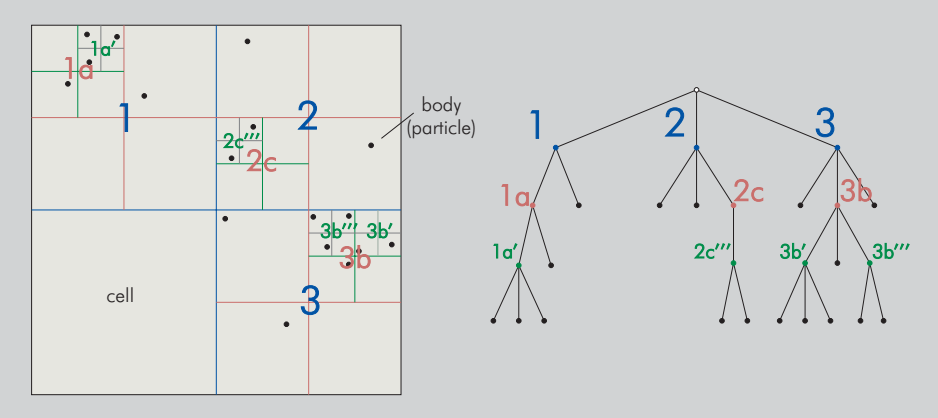

Figure 6.16: Creating a Barnes-hut tree

The second step is to divide the space recursively in cells. The approach taken in the Barnes-Hut method is to evenly divide the space in each dimension recursively. For example, in two dimensions the space is divided into four square regions; in three dimensions, the initial cube is divided into eight sub-cubes. The result of this division is a set of problem sub-spaces that are congruent with one another and are spatially scaled versions of the original problem space. Thus, this process can be repeated recursively until either one or no particles are in a cell. In each case, and at each stage of the recursive process, the center of charge of the particle distribution in each cell is calculated.

As this recursive process of subdividing the space continues, the results of each stage of the process can be stored in a tree structure similar to that shown at the right of fig. 6.16. Each node contains parameters associated with the array of particles in the cell. These parameters include center of mass coordinates and total mass for gravitational forces, or center of charge coordinates and total charge for electrostatic forces. The center of charge (CoQ) used here is defined as

$$\vec{r}_{CoQ} = \frac{\sum_i \vec{r}_i |q_i|}{\sum_i |q_i|}$$

There is no a priori reason that other parameters could not be included. For example, magnetic forces could be calculated on the basis of particle position and velocity. The important fact to note is that the utility of tree methods lies in efficiently calculating interparticle distances. Thus, distance dependent forces gain the most from a tree algorithm.

Given that the tree is constructed as shown above, the tree has to be traversed in order

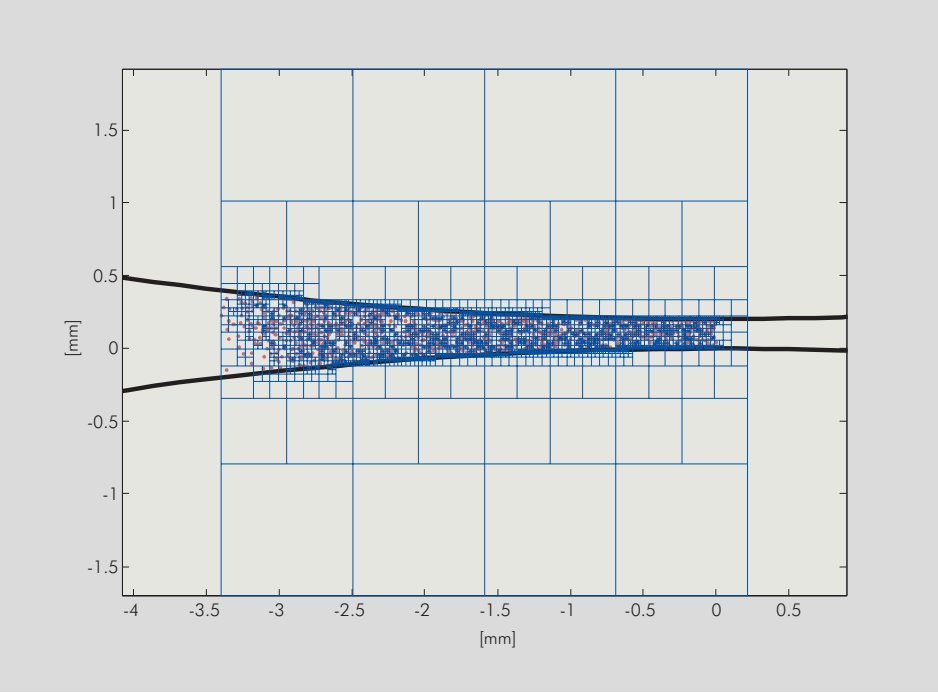

Figure 6.17: Development nip divided in Barnes-Hut quad-tree

to carry out the force calculations. Keeping in mind that the primary objective is to maximize the efficiency in calculating inter-particle distances, it is clear that if an array of particles is far enough away from an individual particle, the array can be treated as a single particle with a composite mass (or charge), located at the center of mass (or charge) of the array.

Thus, for each particle in turn, the tree is traversed, starting at the topmost node. The spatial extent of the node is divided by the distance from the center of mass of the node to the particle. If this quotient is less than a specified quantity (customarily called the theta parameter), the particles in the node are far enough away to be considered a single particle. If the quotient θ is greater than θ_{max}, the tree is recursively descended. θ is defined as

$$\theta = \frac{D}{r} = \frac{size\,of\,box}{distance\,from\,particle\,to\,center\,of\,mass\,of\,box} \tag{6.4}$$

It is remarkable that θ_{max} values as high as approximately 0.5 (equivalent to an angle of about 90 degrees) give an excellent approximation to the actual force, with an error of less then 5 %.

After the total force is calculated on each particle, the particles can be moved. After the motion, the tree may be reconstructed and traversed iteratively. This is the general way that the Barnes-Hut tree is used to calculate the motions of a large number of particles. Detailed analysis of the algorithm indicates that both the tree building phase and the tree walking phase are of $O\left(N \log N\right)$, clearly superior to the unsophisticated $O\left(N^2\right)$ direct summation method.

The code used for the simulation is an improved version of the original algorithm: It reduces the overhead of the tree search by using the fact that neighboring bodies have similar interaction lists. This idea was previously used to speed up hierarchical force calculation on vector machines [Bar90], but the earlier code simply performed a tree search for a small volume defined by a single cell. In the new code, this idea is applied to all levels of the tree.

Forces on bodies are computed during a single recursive scan of the entire tree. This scan maintains and continuously updates an interaction list; at each level, the fact that a body b lies

somewhere within a cell c is used to limit the set of possible interactions that b might have. The information used to define interaction lists is thus similar to that used in an early parallel code [BH86] or the Fast Multipole Method [GR87].

The diagram 6.18 compares the simulation runtime for the two approaches: Direct summation, which shows the predicted $O\left(N^2\right)$ dependency, and the new treecode implementation. The performance gain is significant: From as low as 50 particles, the treecode algorithm is faster than the particle-particle summation. Only for a very small number of particles the overhead for creating the tree eliminates the speedup of traversing the recursive tree.

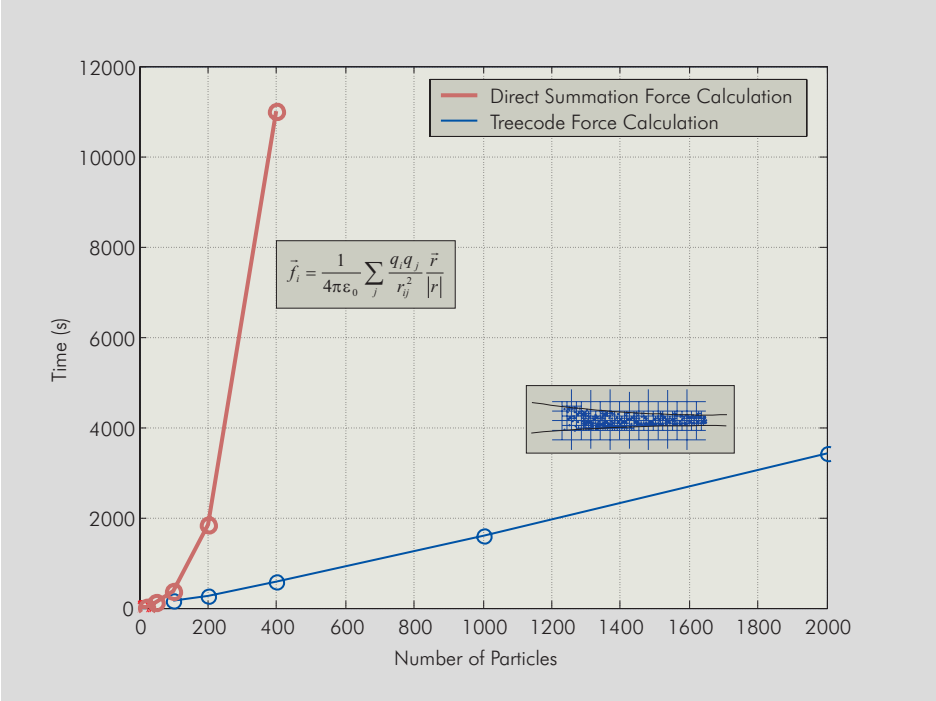

Figure 6.18: Simulation runtime

Compared to the original use of the treecode algorithm for astrophysical calculations by Barnes and Hut, the simulation of particles requires some additional considerations: The distances in astrophysics are literally "astronomical", so that collisions between bodies can be neglected. The spatial dimension of the bodies is therefore unimportant for the calculations. In fact, it is common practice for these applications to introduce a "softening parameter" δ in the gravitational force calculation [BH86]:

$$\vec{f}_{grav} = G\frac{m_1 m_2}{r^2+\delta^2}\frac{\vec{r}}{r}$$

However, for particle simulations, the consideration of particle collisions is essential since the simulation starts with a dense layer of particles on the jump roller and should end with a dense layer on the photoconductor. Obviously, a calculation-time intensive collision routine (see 5.8.3.2) has only to be carried out if two particles are in close proximity, i.e. if their distance is smaller than the sum of their radii. Testing this condition for every pair of particles results once again in an $O\left(N^2\right)$-calculation time dependency. But, since the treecode algorithm is already employed, there is a more elegant solution: The collision routine has only to be used for these pairs of particles, where the θ-value from (6.4) is greater than θ_{max}. It is important to set θ_{max} correctly to achieve reasonable results. Fig. 6.19, left, shows the problem that can arise,

if θ_{max} is chosen too large: The θ parameter for testing particle 1 in cell a with cell b would be $\theta = s/d < \theta_{max}$. This would have two consequences: First, the particles 2 and 3 in cell b would be combined to a virtual particle for the electric force calculation, resulting of course in a certain, but still tolerable, error. But second, the collision routine between particle 1 and 2 would never be activated since the tree is not descended that far, resulting in an intersection between the two particles. This means that θ_{max} has to be set carefully: Fig. 6.19, right, shows the worst case, i.e. with the maximum distance between a particle in cell a and the center of cell b. The θ-parameter is then

$$\theta = \frac{s}{d_{max}} = \frac{s}{\sqrt{\left(\frac{3}{2}s\right)^2 + \left(\frac{1}{2}s\right)^2}} \approx 0.63$$

This is the maximum value, θ_{max} can be set to, without risking particle intersections.

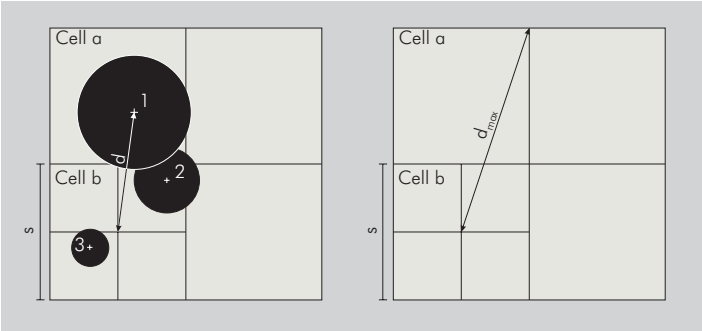

Figure 6.19: θ-Dependance of particle collisions

One way for further improvement of the tree code algorithm is to consider the spatial distribution of the charges within a cell [PG96]. The simple form introduced above uses only the center of charge of one cell, therefore neglecting all information about the particle distribution within the cell. This can be achieved by performing a multipole expansion leading to a force expression

$$\vec{f}(\vec{r}_c - \vec{r}_{pc}) = \vec{f}(\vec{r}_c) + \vec{r}_{pc}\frac{\partial}{\partial \vec{r}_c}\vec{f}(\vec{r}_c) + \frac{1}{2}\vec{r}_{pc}\frac{\partial^2}{\partial^2 \vec{r}_c}\vec{f}(\vec{r}_c)\,\vec{r}_{pc} + \ldots$$

with $\vec{r}_c$ the vector from the particle to the center of charge of the cell and $\vec{r}_{pc}$ the vector from an individual particle in the cell to the center of charge. For the two-dimensional case derived

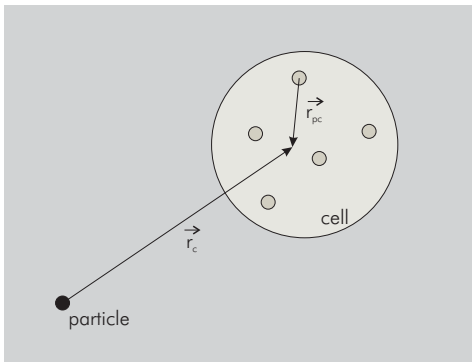

Figure 6.20: Multipole expansion of spatial distribution in cell

above, this leads to a force expression in x-direction for the monopole, dipole and quadrupole moments

$$\begin{array}{rcll} f_{x_{mon}} & = & \frac{q_i}{2d\pi\epsilon_0}\frac{x}{R^2}\sum_i q_i & \text{Monopole} \\ f_{x_{dip}} & = & \frac{q_i}{2d\pi\epsilon_0}\left[\left(\frac{2x}{R^4}-\frac{1}{R^2}\right)\sum_i q_i x_i + \frac{2xy}{R^4}\sum_i q_i y_i\right] & \text{Dipole} \\ f_{x_{quad}} & = & \frac{q_i}{2d\pi\epsilon_0}\left[\left(\frac{8x^3}{R^6}-\frac{6x}{R^4}\right)\sum_i q_i x_i^2\right. & \\ & & \left. + \left(\frac{8xy^2}{R^6}-\frac{2x}{R^4}\right)\frac{1}{2}\sum_i q_i y_i^2 + \left(\frac{8x^2y}{R^6}-\frac{2y}{R^4}\right)\sum_i q_i x_i y_i\right] & \text{Quadrupole} \end{array} \tag{6.5}$$

The respective formulae for the y-direction can be derived similarly.

The consideration of higher moments leads to two changes in the simulation sequence: First, after the tree building phase, another module has to be called where the dipole and quadrupole moments for every cell are calculated. Then, in the actual force calculation routine, the force algorithm has to be extended as described in (6.5). While the implementation of the second step is straightforward, the calculation of the multipole moments needs some more thought to keep the computation time within tolerable limits. The most efficient way possible is to calculate the required moments like $\sum q_i$, $\sum q_i x_i$ or $\sum q_i x_i^2$ at the highest level of the tree, and then use these moments to calculate the moments of the parent cells.

Due to the different center of charge of the daughter and the parent cells, the moments have to be calculated relative to the new origin. The difference vector

$$\vec{r}_{diff} = \vec{r}_{CofQ_{new}} - \vec{r}_{CofQ_{old}}$$

can be used to substitute the original coordinates in the momentum calculation

$$\begin{aligned} D_{x_{new}}^{daughter} &= \sum_i q_i \left(x_i - x_{diff}\right) \\ &= \sum_i q_i x_i - x_{diff}\sum_i q_i \end{aligned}$$

This expression can be used to get the whole dipole moment of the parent cell by summing up the shifted moments of the daughter cells

$$\begin{aligned} D_x^{parent} &= \sum_d \left(\sum_i q_i x_i - x_{diff}\sum_i q_i\right) \\ &= \sum_d \left(D_{x_{old}}^{daughter} - x_{diff} M^d\right) \end{aligned}$$

The same procedure can be applied for the higher moments. It has been shown however that the refinement of the tree code by including the dipole moments is sufficient to reduce the error below 1% compared to a direct summation algorithm. An inclusion of higher moments would not improve the accuracy of the whole simulation significantly since the approximations made in other modules will dominate the total error. Therefore the tree code used here utilizes only monopoles and dipoles to reduze computation time.

Chapter 7

Results

7.1 Simulation of a DC voltage experiment

7.1.1 Cohesion force calibration

The experiment described in chapter 2.5.2, where toner was transferred between two rollers using only a DC voltage, has only a few number of influencing factors compared to the experiments with AC voltages or the real print process. Therefore it seemed reasonable to start by simulating these simplified conditions, so the simulation results could be calibrated and verified. The simulation of this experimental setup has also the additional advantage, that due to the symmetry of the setup, only half of the number of particles has to be used, which helps to reduce the computation time. As a consequence, for every particle (x_i, y_i) a symmetric particle is placed at $(-x_i, y_i)$.

As mentioned in chapter 5.8.2, the short-range inter-particle attractive cohesion force cannot be measured directly and has therefore to be adjusted by comparing the results of a simulation run and a real experiment. The DC voltage experiment seems to be a suitable testing environment due to the limited number of physical effects.

The assumptions made for the cohesion force are that the cohesion force increases for larger particles and decreases for particles that are covered with a higher amount of nano-scale silica particles. These are the same dependencies that exist also for the particle-substrate adhesion force. Therefore, a cohesion force was assigned to each particle that is proportional to the measured adhesion force (see chapter 2.4)

$$f_{coh_i} = k \cdot f_{adh_i}$$

The force used for the interaction of two particles i and j is calculated from the geometric mean of the two cohesion forces

$$f_{coh_{ij}} = \sqrt{f_{coh_i} \cdot f_{coh_j}}$$

Several simulation runs were made, where a compact toner layer on the jump roller was exposed to an electric field, resulting from a DC voltage of 1000 V. k was varied in a wide range from nearly zero to numbers far greater than 1. To minimize any additional external effects, the initial toner layer on the jump roller was not formed using the geometric deposition algorithm (see chapter 4.3). Instead the particles formed a compact layer where all particle properties like diameter, charge or cohesion were distributed completely homogeneously.

The simulation results should reproduce two characteristic results of the experiment:

- The thickness of the transferred toner layer should be equal to the thickness measurements (see fig. 2.14), i.e. about one fourth or one third of the original thickness

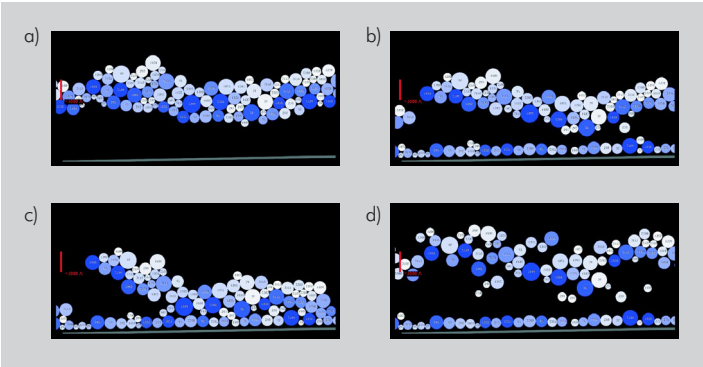

Figure 7.1: Variation of cohesion force

- The transferred toner does not cover the counter electrode completely, since a large area of uncovered aluminum can be seen in the microscope (fig. 2.15). Most of the particles lie separately on the counter electrode surface, yet the SEM micrographs show, that some clusters exist where particles are also lying on top of each other

Fig. 7.1 shows the results from the simulation runs for four different values of k. The illustrations show the moment of particle detachment, as this simplifies the comparison of the different behavior: Fig. 7.1(a) shows the effect of a very large cohesion force ($k \gg 1$). The particle layer is detached as a whole. In fig. 7.1(b) the cohesion force is smaller than the particle-roller adhesion ($k < 1$). In this case, all the particles are detached as one large cluster except for the ones directly connected to the roller. In fig. 7.1(c) the cohesion force is of the same order of magnitude as the adhesion force ($k \approx 1$). Large clusters are detached where the charges are high enough, while at other locations they remain on the roller. Fig. 7.1(d) shows the case where there is almost no cohesion force ($k \to 0$). All the particles not in touch with the roller are detached and are almost instantaneously separated.

Obviously, none of these four cases reproduces the behavior observed in the experiment, where only a small fraction of the particles is detached. So additional effects not considered so far have to be taken into account.

7.1.2 Model refinement

If only a small fraction of the initial toner layer shall be detached, the forces on these particles have to be different from those on the rest of the layer. The initial explanation of the experimental results was that the repulsive coulomb forces of the first layer of detached particles will detain the rest of the layer from being detached. However, since the simulation contains the electric interaction between all particles, the consequences of this effect are already included in the simulation results shown above.

Two additions have to be made to the model to achieve correct results: First, the initial conditions have to be changed according to the stochastic magnetic brush algorithm described in chapter 4.3. As shown in fig. 4.10, this leads to a different distribution of charge and cohesion: The particles on the outward side of the layer, that should be detached first, are higher charged and have lower cohesion forces, facilitating their detachment.

The results with such an initial layer show an improved detachment behavior (fig. 7.2), compared to fig. 7.1. Less particles are detached, so that the coverage of the counter electrode is almost comparable to the experiment. However there are still too many relatively large clusters of particles, meaning that there is another effect that has yet to be added to the model.

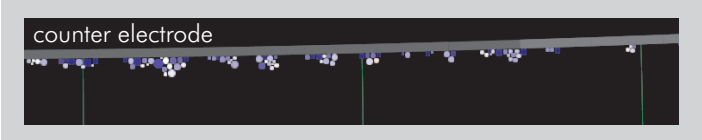

Figure 7.2: Result from DC voltage simulation with initial layer from geometric deposition algorithm

The idea was, that due to the toner conductivity, electric charge might be transferred between adjacent toner particles instead of being fixed on them. In this case, the electric fields could cause a charge transfer from the particles near the roller towards the outer particles, thus further facilitating their detachment [HW02]. Measurements have shown, that there is indeed a conductivity in toner layers.

An additional simulation step was introduced: Whenever two particles come into contact, a certain percentage of the charge on the particle near the roller is transferred to the particle further away from the roller, with the percentage chosen proportional to the component of the electric field $\vec{E}$, that is parallel to the vector $\vec{r}$ connecting the two particles.

$$\delta q \sim \frac{\vec{r} \cdot \vec{E}}{|\vec{r}|}$$

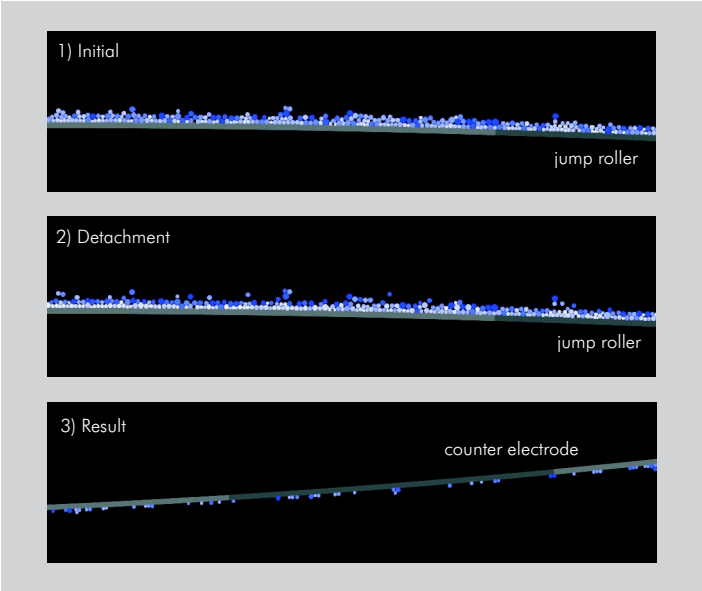

Figure 7.3: Charge transfer, detachment and result

Fig. 7.3 shows the results from a simulation run with included charge-transfer. The second picture clearly shows a motion of the charges (indicated by blue color) towards the outward particles, compared to the initial values in the first picture. This facilitates the detachment of these higher charged particles leading to the resulting distribution on the counter electrode. As can be seen in the third picture, there are some small agglomerates of up to three particles, but the majority of the particles is deposited isolated which is very similar to the experimental observations.

7.2 Simulation of an AC voltage experiment

7.2.1 Calibration of the damping factor

The next step after simulating a DC voltage transfer experiment is the simulation of an AC transfer experiment. The main characteristic known from the corresponding experiments is that a small number of particles detached initially, can trigger the detachment of a far larger number of particles. The idea is that these initial particles are jumping back and forth in the nip, due to the alternating electric fields. When they are bouncing back on the toner layer on the jump roller, they convey a momentum on the remaining particles, enabling them to be also detached. An important parameter for this mechanism is the damping, that occurs when two particles collide, modeled by the damping factor d (see chapter 5.8.3.2). That factor has the disadvantage that although its use for the DEM simulation here is correct, it is difficult to observe in an experiment. A variable that is more easily understood is the coefficient of restitution, i.e. the ratio of the momentum after the collision compared to the ratio before it [Kuc91]. The relation between the damping factor and the coefficient of restitution has to be established numerically by simulating the bouncing of a particle on a rigid boundary at different damping factors and comparing the resulting coefficients of restitution.

The way to find out the correct damping is to compare the simulation results for different damping factors with the measurements of chapter 2.5.4. If the damping is too high, a particle bouncing back will just stick to the toner layer due to the cohesion forces, instead of detaching other particles. On the other hand, if the damping is too low or even zero, this would contradict to the physical reality and, in addition, could lead to numerical instabilities, as small disruptions in a compact particle layer would cause the destruction of the whole layer (the problem of numerical instability, however, is reduced by the implementation of air viscosity that acts also as a damping influence).

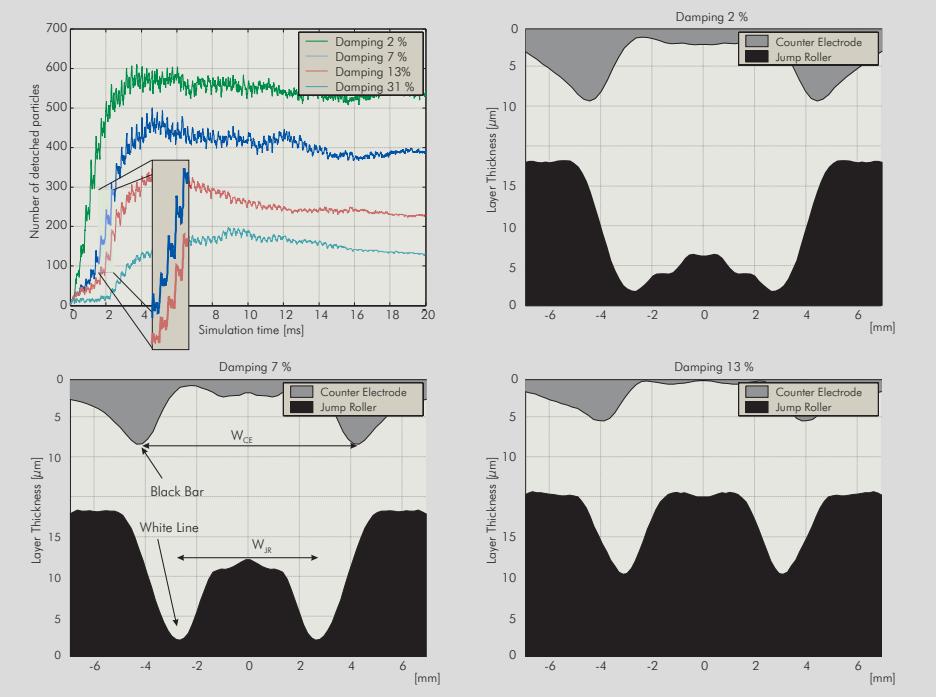

Figure 7.4: Simulation results for experiment with AC voltage at different damping factors

Fig. 7.4 shows the summarized results of several simulations of the experiment with an AC

voltage applied. The upper left diagram shows the amount of particles that are detached during the simulation, depending on the damping factor. For higher damping factors, less particles are detached, as expected. A closer look on the curve (see magnification) shows, that the detachment does not occur continuously, but at certain periodic time steps. These are exactly the time steps, where the AC voltage moves the already detached particles back on the original toner layer, thus confirming the theory, that particle detachment with AC voltage influence follows some sort of avalanche effect. The other three pictures in fig. 7.4 show the thickness of the remaining particle layer on the jump roller and of the deposited particle layer on the counter electrode for different damping factors. To decide which damping factor approximates reality best, these layers have to be compared with the experimental result in fig. 2.16. As mentioned in chapter 2.5.3, two black bars of toner can be seen on the counter electrode, while two lines of missing toner are found on the jump roller. The width between the two bars on the counter electrode W_{CE} is larger than the width between the lines on the jump roller W_{JR}. In general, all three damping factors reproduce this behavior roughly. Especially the two black bars and the two white lines are clearly visible. Also, the distances W_{CE} and W_{JR} that result from the simulation are comparable to the measured distances in the experiment. However, there are some differences: For a higher coefficient of restitution (e.g. 13 %), the lines of missing toner on the jump roller are not distinctive. There is still a remaining toner layer of about 10 μm at these lines, so that the jump roller surface would not be seen, which is contrary to the results from fig. 2.16. For lower coefficients of restitution (e.g. 2 %), toner is not only removed from the jump roller at the two lines, but also in between them. Therefore the coefficient of restitution was set at a compromise of 7 %, equivalent to a damping factor d of $2 \cdot 10^{-8} N\frac{s}{m}$, for the further simulations, since the results shown in fig. 7.4 for that damping factor confirm quite well the experimental results. It is obvious, that this not an exact way of determining that parameter, rather an approximation of the order of magnitude.

To confirm the correctness of the model refinements made in chapter 7.1.2, the simulations were also run without the initial conditions according to the stochastic magnetic brush algorithm and without the additional charge transfer step. The result was, that both additions had to be present to receive the results shown in fig. 7.4. If the charge transfer step was left out, the were no highly-charged particles, that could be detached initially. These particles seem to be crucial to start the avalanche effect of detachment. On the other hand, if the initial particle layer was not created by the stochastic magnetic brush algorithm, the avalanche effect did not start. The special distribution of particle properties, created in the magnetic brush, seems to be a necessary prerequisite for the detachment of the whole particle layer.

7.2.2 Dependence of transfer efficiency on the applied voltage

The experiments in chapter 2.5.4 have shown, that the transfer efficiency depends on the magnitude, the frequency and the wave form of the applied AC voltage. Several simulations were performed, where these parameters were varied to test the correctness of the simulation and to find out the reason for these dependencies.

The main reason for higher transfer efficiency for these different parameters is a higher mean velocity of the particles, when they are bouncing back on the original toner layer. Thus, a higher momentum can be transferred, increasing the probability of detaching other particles. Thus, it is obvious that higher magnitudes of the AC voltage result in higher transfer efficiency, as the enlarged accelerating forces imply higher particle velocities. In practice, the limit for this way of improving transfer is the breakdown limit of air ($E_{max} \approx 7.5 \cdot 10^6 \frac{V}{m}$).

Experimental and simulation results have both shown, that the efficiency can be further increased by switching from a sine to a square-formed voltage. This is understandable, since the velocity after one half-cycle depends on the integral of the acceleration. Therefore the ratio

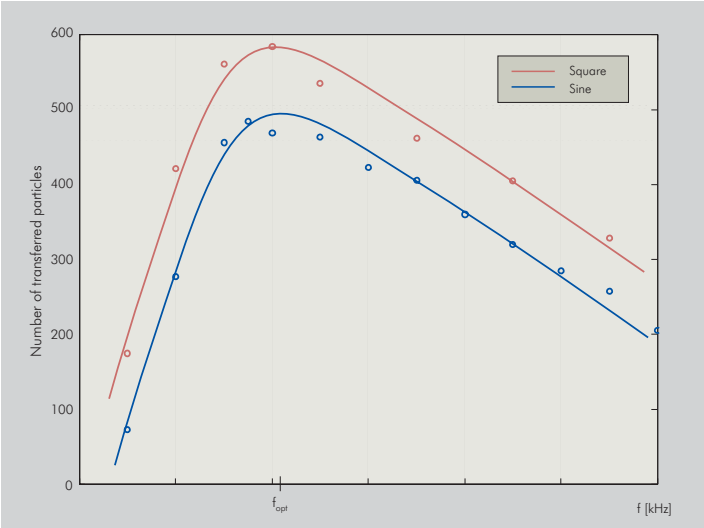

Figure 7.5: Simulation results for experiments with different AC voltages

between the velocity after one sine half-cycle and one square half-cycle is

$$\frac{v_{square}}{v_{sine}} = \frac{\int_0^{T/2} U dt}{\int_0^{T/2} U \sin \omega t dt} = \frac{\pi}{2}.$$

Of course, this is only a theoretical maximum value, since the high number of particle-particle interactions lead to a complex non-linear n-body system. Nevertheless, a square-formed AC voltage is the most efficient way of accelerating particles in a parallel gap, if a certain maximum electric field shall not be exceeded.

The reason for the dependence on the AC frequency can be shown best with a simplified model: A single toner particle is moving up and down in a parallel gap under the influence of an alternating electric field. All effects like air viscosity, adhesion at the boundaries or damping when bouncing off are included. Fig. 7.6 shows the trajectories at different frequencies: There is one frequency f_{opt}, where the wave length of the AC voltage is such, that it corresponds optimally with the gap size. The particle is then bouncing between the two walls in the shortest possible time and hits the walls with the highest possible velocity. For a many-body system an excitation at this frequency means, that every detached particle bounces back on the original layer more often and can transfer a higher momentum.

For lower frequencies $f < f_{opt}$, the particle bounces off the wall, before the accelerating force is reversed (see fig. 7.6, upper), while for higher frequencies $f > f_{opt}$, the particle is too slow to follow the excitation.

Summary All in all, the applied AC voltage has to meet three conditions to maximize toner transfer:

- The peak value has to be chosen so that the resulting fields remain shortly below the air breakdown limit.
- The wave-form has to be square-formed.
- The frequency has to be adjusted according to the gap size, so that $f \approx f_{opt}$.

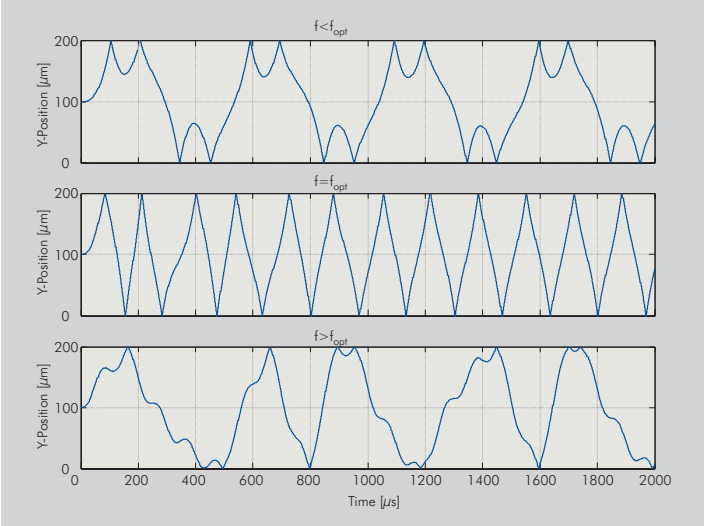

Figure 7.6: Simplified model for toner jumping at different excitation frequencies

7.3 Simulation of a real print process

7.3.1 Process characteristics

7.3.1.1 General

When simulating and analyzing the development process with the boundary conditions of the real developer station, a high number of particles has to be used, to ensure, that any initial phenomena have decayed. Typically, a number of 10000 particles has proven to be sufficient. With a typical toner layer thickness of about 20 μm this results in a layer length of about 35 mm. According to the surface velocity, the simulation has to cover about 40 ms of simulated time to include the development process of all particles until their final deposition. A complete simulation run takes about 2-4 days of computation time, depending on the hardware platform and the calculation accuracy.

The most simple case is the development of a completely discharged photoconductor. The result should be a densely covered homogeneous area of toner, ideally with all the particles offered on the jump roller transferred to the photoconductor.

When starting the simulation, first some particles which are only loosely bound to the rest of the particle layer are detached. As shown in fig. 7.4, these initial particles start an avalanche effect by jumping back and forth, thus detaching the majority of the other particles. It takes about 10 ms of simulation time until a stable equilibrium between newly detached particles and finally deposited particles is achieved. Any statistics dealing with transfer efficiency or jump behavior must only take the particles after this initial phase into account.

Fig. 7.7 shows the trajectories of a large number of particles during the jump process. The figure is split: The upper part shows all particles, that are deposited on the jump roller after passing the nip, the lower part shows all particles, that are deposited on the photoconductor. For each of the two cases, the trajectory of a typical particle is drawn as a thick red line. These trajectories illustrate, that the development process is a complex jumping up and down with several intra-particle collisions until the particle is finally deposited.

For this example configuration, the transfer efficiency was about 57 %. It is interesting to notice, that this is not due to the fact, that the others particles could not be detached from the jump roller. Quite in contrary, fig. 7.7 shows, that a large number of particles that rest on

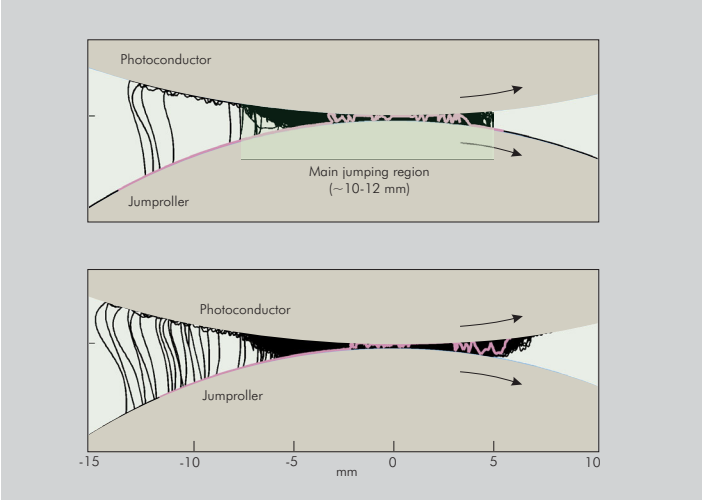

Figure 7.7: Particle trajectories for particles deposited on the jump roller (upper part) and on the photoconductor (lower part)

the jump roller in the end of the process had been detached while they went through the nip. However, when leaving the nip, the forces from the applied electric field were smaller than the repulsive forces from the already transferred toner particles. Therefore, they were deposited back on the jump roller. An analysis of the trajectories shows that only one fourth of the particles that rest on the jump roller afterwards had never been detached in the nip.

This can be verified by varying the AC and the DC component of the applied voltage separately. Adjusting the AC voltage changes the percentage of particles that are detached at all, while adjusting the DC component changes the percentage of those detached particles, that are deposited on the photoconductor.

There is also a certain percentage of particles that is detached from the jump roller but is neither deposited on the photoconductor nor back on the jump roller (not displayed in the figure). These are typically particles which are charged very lowly, so that the electric forces acting on them are very small. This behavior can also be observed in the real developer station: If for some reason a higher percentage of toner is only charged very lowly, a cloud of emitted toner can be observed that is obviously neither deposited on the photoconductor nor on the jump roller.

When looking at the trajectories, there is clearly one region at the center of the nip, where most of the jumping occurs. This region is about 10 to 12 mm wide and can also be verified in the real process: When the photoconductor motion is stopped before the electric fields at the developer station have been switched off, the rest of the toner on the jump roller is transferred to the photoconductor. This region on the photoconductor can be measured and shows to be also about 10 mm wide.

7.3.1.2 Influence of adhesion forces

It is well-known that the use of rollers with a coating, that creates a high toner particle adhesion, influences the whole print process negatively. Therefore, high efforts are being made to optimize the coating for rollers and photoconductors to minimize toner adhesion. To show the influence of the adhesion forces on the transfer efficiency, several simulations with a completely discharged photoconductor were done. To simulate different coatings, the mean adhesion force (electrostatic and non-electrostatic) was varied in a wide range. The variation was done for the

roller and the photoconductor surface simultaneously. Fig. 7.8 shows the distribution of the particles after the simulation:

- For very low adhesion forces, almost all particles were detached from the jump roller. Some of them were however deposited back on the jump roller while another large percentage wasn't deposited either on the jump roller nor on the photoconductor.
- The percentage of particles on the photoconductor does not vary much for low adhesion forces. There seems to be some limit for the maximal thickness of the transferred toner layer since lower adhesion forces result only in a higher percentage of particles that were not deposited at all.
- Higher adhesion forces result in a higher percentage of particles that could not be detached from the jump roller.

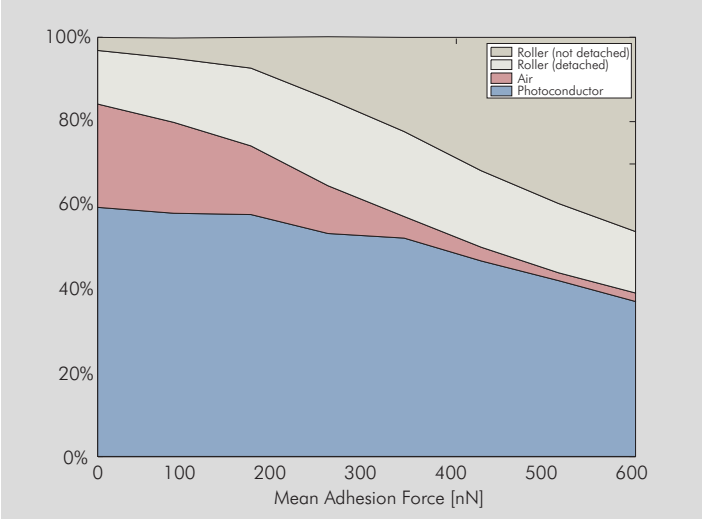

Figure 7.8: Simulation results for different adhesion forces

7.3.2 Special print patterns

7.3.2.1 Periodic Lines

A typical test to evaluate the print quality is to print a test pattern, consisting of periodic lines. The pattern chosen here is built up from one black micro line, followed by three white micro lines. The large white space between the black lines was chosen to assure that the Gaussian light curves of the LEDs, that form the black lines, do not intersect (see fig. 3.4). This print pattern allows to evaluate the uniformity of the line width, which is important for the visual impression of the printed result.

Since only every fourth LED is switched, it could be expected, that the amount of transferred toner is only a fourth compared to the previous simulation of a completely discharged photoconductor. However, the simulation results show, that there is still a transfer efficiency of 33 %, compared to 57 % for the discharged photoconductor. Two effects account for this phenomenon:

1. Due to the broad Gaussian light curve, the mean width of the deposited lines in the simulation is 66 μm compared to the 42.3 μm that an ideal line should have at 600

dpi print resolution. This corresponds to measurements of real print samples where the measured line width was 72 μm.

2. Due to the curved electric field lines around the black lines, toner particles from the area of the three white lines is drawn towards the black lines, resulting in an accumulation of toner there. This means that the maximum thickness of the toner layer is more than 50 % higher for a periodic line pattern than for a homogeneous full plane.

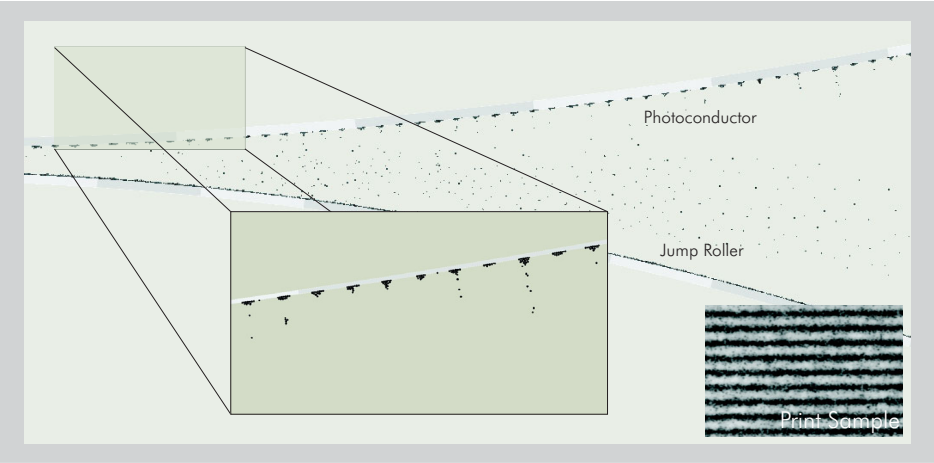

Figure 7.9: Simulation results for periodic lines

7.3.2.2 Edge

Another interesting print pattern is an edge, i.e. the border between a completely discharged and a completely charged plane. One would expect, that the result is simply the combination of these two patterns, so that one half would be covered homogeneously and densely with toner, while the other half shows only some mistakenly deposited background particles. However, print tests have shown a line with a width of about 1 mm at an edge, which is more densely covered with toner. This can be observed visually only, if the optical density (i.e. the blackness of a full plane) is set so low, that an additional toner deposition results in an additional blackness. This is the reason why the discharged area in the print sample of fig. 7.10 seems to be so inhomogeneous.

The effect of an increased toner deposition near edges is called edge effect and can be measured at all optical densities: For lower optical densities, it can be observed visually, for higher optical densities, a sensor like in chapter 2.5.2 has to be used to measure the thickness of the toner layer. The simulation can help to explain that behavior: The results from the FEM calculation of the electric field in fig. 7.10 show, that near the edge some field lines are bent from the charged area to the discharged area. Since the field lines indicate the direction of the electric force on the charged toner particles, this means that a number of particles that are jumping up and down in the charged area and would have otherwise been deposited back on the jump roller will get an additional momentum towards the discharged area. There, they augment the number of deposited toner particles on the photoconductor, thus creating the visible black line at the edge.

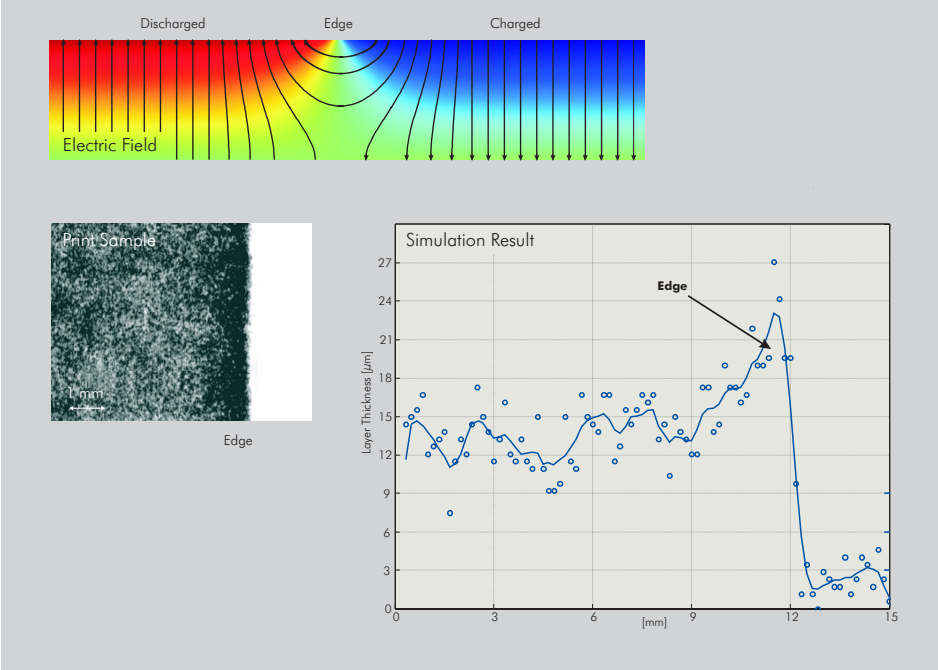

Figure 7.10: Edge Effect

7.4 Summary and outlook

This work has shown that it is possible to simulate a complete electrophotographic process by building up physical models for the various process steps and solving the resulting equations numerically.

Starting from the optical image created by the LED print head, the creation of the latent charge image on the photoconductor was modeled as one of the key input parameters for the many-body toner simulation. Another important input parameter for that simulation is the initial configuration of the toner layer, that results from the simulation of the magnetic brush. Due to computation time restrictions, a simplified model had to be chosen here. The validity of this model could be proven by comparing the results of the discrete element method simulation of the toner development process with an appropriate experiment. The toner simulation delivered only reasonable results when combined with the results from the magnetic brush simulation. In addition, a further model refinement was necessary to simulate all the effects which were found in the experiment: An additional inter-particle charge transfer had to be included in the simulation loop.

Together with the basic discrete element method where all relevant forces on the particles are included and the particle properties are distributed according to previous measurements, the resulting model makes it possible to simulate and understand the basic mechanisms of toner transfer and toner deposition. It could be shown, that the transfer of a thick toner layer consists of a two-step process: First, some highly-charged particles are detached, then these initial particles bounce back on the original toner layer, following the alternating electric fields and detach other particles, thus starting an avalanche effect. The simulation was also successfully to understand certain phenomena at typical test patterns like periodic lines or edges.

Apart from understanding the physical background of certain process steps, the simulation tools developed in this work can now be used to optimize the process by a systematic variation of materials, geometries, electric or magnetic setups. Thus, time-consuming series of real experiments can be partly replaced by virtual ones.

For the future, there are several ways how this work can be continued. The main issue for all simulations are the limitations due to the available computation time. By porting the code to a powerful vector computer it should be possible to circumvent that limitation. Thus, it would be possible to extend the model: The algorithm for a thorough discrete element modeling of the carrier brush described in chapter 4 could be applied for a better understanding of the complex phenomena in that many-body environment. Another extremely interesting extension could be a three-dimensional discrete-element simulation, so that the creation of two-dimensional print patterns could be studied.

Appendix A

Physical Data

Fig. 2.1: $d_{50,3} = 7.1\mu\text{m}$

Fig. 2.3: $q_{max} = 30\text{fC}$

Fig. 2.8: $d_{50,3} = 7.1\mu\text{m}$

Fig. 2.22: $f_{opt} = 3.2\text{kHz}$

Fig. 3.2: $H_{res} = 1.2\mu\text{J/cm}^2$
$U_{res} = -60\text{V}$
$U_0 = -530\text{V}$
$\sigma_{res} = -7.14 \cdot 10^{-4}\text{C/cm}^2$

Fig. 3.5: $H_{res} = 1.2\mu\text{J/cm}^2$

Fig. 3.6: $v_{max} = 1\text{m/s}$

Fig. 3.7: $H_{res} = 1.2\ \mu\text{J/cm}^2$
$H_{100} = 5.9\mu\text{J/cm}^2$
$H_{lbo} = 4.7\mu\text{J/cm}^2$
$H_{lin} = 0.8\mu\text{J/cm}^2$
$U_{res} = -60\text{V}$
$U_0 = -530\text{V}$

Fig. 4.2: $v_{max} = 1.5\text{m/s}$

Fig. 4.3: $B_{ext} = 0.12\text{T}$
$B_{max} = 0.4\text{T}$

Fig. 4.5: $B_{ext} = 0.12\text{T}$
$M_{max} = 67\text{emu/g}$

Fig. 4.10: $Q_{max} = 30\text{fC}$
$d_{50,3} = 7.1\mu\text{m}$

Fig. 5.4: $v_{Surface} = 1\text{m/s}$
$v_{max} = 1.5\text{m/s}$

Fig. 5.5: $U_0 = -530\text{V}$

Fig. 6.13: $U_0 = -530\text{V}$

Bibliography

[Amd67] G. M. Amdahl. Validity of single-processor approach to achieving large-scale computing capability. In *Proceeding of AFIPS Conference*, pages 483–485, 1967.

[ANCN86] I. Abiko, Y. Nakamura, M. Chiba, and K. Nihei. High printing quality led printheads. *Journal of Imaging Technology*, 12(5):300–303, 1986.

[ARO01] Hussain Al-Rubaiey and Pirkko Oittinen. Transfer current and efficiency in toner transfer to paper. In *Proc. of IS&Ts NIP 17 International Conference on Digital Printing Technologies*, pages 648–652. Society for Imaging Science and Technology, 2001.

[Bar90] Joshua Barnes. A modified tree code. *Journal of Computational Sciences*, 87(161), 1990.

[BCP92] N. A. Burnham, R. J. Colton, and H. M. Pollock. Interpretation of force curves in force microscopy. *Nanotechnology*, 1992.

[BD96] George L. Batten and Paul J. Delekto. A new test for toner adhesion. In *TAPPI Proceedings*. Papermakers Conference, 1996.

[BG94] Thomas J. Behe and Daniel R. Gilmore. Ceramic donor roll for scavengeless development in a xerographic apparatus. *United States Patent*, Jun. 21 1994. #5,322,970.

[BH86] Joshua Barnes and Piet Hut. A hierarchical o(n log n) force calculation algorithm. *Nature*, 324(446), 1986.

[BP83] Claus Bischof and Wulff Possart. *Adhäsion: Theoretische und experimentelle Grundlagen*. Akademie-Verlag, 1983.

[BPÅ99] Anders Berg-Palmqvist and Johannes Åkesson. Tools for simulation of toner particle motion in a tonerjet printer. In *Proc. of IS&Ts NIP 15 International Conference on Digital Printing*, pages 276–279, 1999.

[Cam96] Peter Campbell. *Permanent Magnet Materials and Their Applications*. Cambridge University Press, 1996.

[Com02] Comsol AB. *Femlab - Electromagnetics Module*, 2002.

[CS79] P. Cundall and O. Strack. A discrete numerical model for granular assemblies. *Geotechnique*, 29(1):47–65, 1979.

[CS97] G. Castle and L. Schein. General model of sphere-sphere insulator contact electrification. In George Marshall, editor, *Recent Progress in Toner Technology*, pages 149–151. The Society for Imaging Science and Technology, 1997.

[CY02] C. Chou and A. Yang. The tribocharging behaviour in toner-carrier systems. *Journal of Imaging Science and Technologies*, 46(3):208–215, 2002.

[DMB55] J. H. Dessauer, G. R. Mott, and H. Bogdonoff. Electrophotography. *Photo. Eng.*, 6(250), 1955.

[Fen98] James Q. Feng. Theory of electric field detachment of charged toner particles. In *Proc. of IS&Ts NIP 14 International Conference on Digital Printing Technologies*, pages 374–377, 1998.

[FH98] James Q. Feng and Dan A. Hays. A finite-element analysis of the electrostatic force on a uniformly charged dielectric sphere resting on a dielectric-coated electrode in a detaching electric field. *IEEE Transactions on Industry Applications*, 34(1):84–91, 1998.

[FH00] James Q. Feng and Dan A. Hays. Theory of electric field detachment of charged toner particles in electrophotography. *Journal of Imaging Science and Technology*, 44(1):19–24, 2000.

[Flü86] Siegfried Flügge. *Rechenmethoden der Elektrodynamik*. Springer, 1986.

[FQG+92] David P. Fullagar, Peter J. Quinn, Carl J. Grillmair, John K. Salmon, and Michael S. Warren. N-body methods on MIMD supercomputers: Astrophysics on the intel touchstone delta. In *Fifth Australian Supercomputing Conference*, 1992.

[FR88] Wm. Y. Fowlkes and K. S. Robinson. The electrostatic force on a dielectric sphere resting on a conducting substrate. In K. L. Mittal, editor, *Particles on Surfaces 1*, pages 143–155. Plenum Press, 1988.

[FT98] Yutaka Fukuchi and Manabu Takeuchi. A comparative study on toner adhesion force measurements by toner jumping and centrifugal method. In *Proc. of IS&Ts NIP 14 International Conference on Digital Printing Technologies*, pages 390–393. Society for Imaging Science and Technology, 1998.

[FT99] Yutaka Fukuchi and Manabu Takeuchi. Particle adhesion force measurements by toner jumping methods. In *Proc. of IS&Ts NIP 15 International Conference on Digital Printing Technologies*, pages 582–585. Society for Imaging Science and Technology, 1999.

[Gal77] C. F. Gallo. Corona - a brief status report. *IEEE IA-13*, 6:550–557, 1977.

[GFM02] R. Gundlach, A. Fornalik, and W. Mey. New corona charging system. In *Proc. of IS&Ts NIP 18 International Conference on Digital Printing Technologies*, pages 41–44. Society for Imaging Science and Technology, 2002.

[Gol01] Gerd Goldmann. *World of Printers*. Océ Printing Systems, 2001.

[GP03] M. Götzinger and W. Peukert. Dispersive forces of particle-surface interactions: Direct afm measurements and modelling. *Powder Technology*, 130(203):102–109, 2003.

[GQR98] B. Gady, D. J. Quesnel, and D. S. Rimai. Surface treatment and its effects on toner adhesion, cohesion, transfer and image quality. In *Proc. of IS&Ts NIP 14 International Conference on Digital Printing Technologies*, pages 363–366, 1998.

[GQR99] B. Gady, D. Quesnel, and D. Rimai. Effects of silica additive concentration on toner adhesion, cohesion. *Journal of Imaging Science and Technology*, 43(3):288–294, 1999.

[GR87] Greengard and Rokhlin. Many-body tree methods. *Journal of Computational Physics*, 1987.

[GS00] P. M. Gresho and R. L. Sani. *Incompressible Flow and the Finite Element Method*. John Wiley and Sons, 2000.

[GSR96] B. Gady, D. Schleef, and R. Reifenberger. Identification of electrostatic and van der waals interaction forces between a micrometer-size sphere and a flat substrate. *Physical Review B*, 53(12):8065–8070, 1996.

[GV93] Christian Gerthsen and Helmut Vogel. *Physik*. Springer, 1993.

[Ham37] H. C. Hamaker. Adhesion forces. *Physics 4*, page 1058, 1937.

[Hay88] Dan A. Hays. Electric field detachment of charged particles. In K. L. Mittal, editor, *Particles on Surfaces 1*, pages 351–360. Plenum Press, 1988.

[Hay94] Dan Hays. Toner adhesion physics: Measurements of toner/substrate contact areaa. In *Proc. of IS&Ts NIP 10 International Conference on Digital Printing Technologies*, pages 142–145. Society for Imaging Science and Technology, 1994.

[Hay95] Dan A. Hays. Toner adhesion. *Adhesion*, 51:41–48, 1995.

[Her60] G. Herdan. *Small particle statistics*. Butterworths, London, 1960.

[Her02] Martin Herb. Adhäsionsmessungen von polymerpartikeln mit hilfe einer ultrazentrifuge. Master's thesis, Technische Universität München, Lehrstuhl für Feststoff- und Grenzflächenverfahrenstechnik, 2002.

[Hun95] Robert Hunter. *Foundations of Colloid Science*. Clarendon Press, 1995.

[HW02] R. Hoffmann and G. Wachutka. Electrical field induced particle transfer. In *Proc. of Intern. Conference on Modeling and Simulation of Microsystems*, page 258. Nano Science and Technology Institute, 2002.

[IKY99] Haruo Iimura, Hisao Kurosu, and Takeo Yamaguchi. The effects of surface treatment on toner adhesion force. In *Proc. of IS&Ts NIP 15 International Conference on Digital Printing Technologies*, pages 535–538, 1999.

[Jac82] John David Jackson. *Classical Electrodynamics*. de Gruyter, 1982.

[Jak98] Gerd Jakob. Coaxial interferometric measuring of layer thickness. *Photonik*, 1998.

[Jil91] David Jiles. *Introduction to Magnetism and Magnetic Materials*. Chapman and Hall, 1991.

[JKR71] K. L. Johnson, K. Kendall, and A. D. Roberts. Adhesion. *Proc. R. Soc. London, Ser. A*, 324(301), 1971.

[Joh92] Jerome L. Johnson. *Principles of Nonimpact Printing*. Palatino Press, 1992.

[Jon95] Thomas B. Jones. *Electromechanics of Particles*, chapter Electrostatic Contributions to Adhesion, pages 194–207. Cambridge University Press, 1995.

[JP96] S. Jeyadev and Damodar M. Pai. Photoconductor implications in digital electrophotography. *Journal of Imaging Science and Technology*, 40(4):327–333, 1996.

[KE98] Andreas Küttner and Reinhold Epping. Measurements with a small, low-cost toner-charge spectrometer. In *Proc. of IS&Ts NIP 14 International Conference on Digital Printing Technologies*, pages 623–626, 1998.

[KK02] A. Kleier and H. Kleinschrodt. Discontinuous mechanical modeling of granular solids by means of pfc and ls-dyna. In H. Konietzky, editor, *Numerical Modeling in Micromechanics via Particle Methods*, pages 37–43, 2002.

[KNSA98] S. Katakura, M. Nemoto, H. Sato, and K. Ashida. Simulation of electrophotographic process. Technical Report 64, Oki Data Corporation, August 1998.

[Kuc91] Horst Kuchling. *Taschenbuch der Physik*. Fachbuchverlag Leipzig, 1991.

[Lea99] Meng H. Lean. Microscopic particle simulation of air ionization. In *Proc. of IS&Ts NIP 15 International Conference on Digital Printing Technologies*, pages 513–516. Society for Imaging Science and Technology, 1999.

[Lif56] E.M. Lifshitz. Adhesion. *Sov. Phys. JETP 2*, page 73, 1956.

[LT98] Won-Sup Lee and Yasusuke Takahashi. Comparison and evaluation of various tribocharging models of two-component developer. In *Proc. of IS&Ts NIP 14 International Conference on Digital Printing Technologies*, pages 319–323. Society for Imaging Science and Technology, 1998.

[Meh94] Anita Mehta, editor. *Granular Matter: An interdisciplinary approach*. Springer, 1994.

[MOEH00] Howard Mizes, Mary Ott, Elliott Eklond, and Dan Hays. Small particle adhesion: measurement and control. *Colloids and Surfaces*, 165:11–23, 2000.

[MT97] J. W. May and T. N. Tombs. Electrostatic toner transfer model. In *Proc. of IS&Ts NIP 13 International Conference on Digital Printing Technologies*, pages 71–76. Society for Imaging Science and Technology, 1997.

[MV91] K. Meyberg and P. Vachenauer. *Höhere Mathematik 2*. Springer, 1991.

[NK02] Nobuyuki Nakayama and Hiroyuki Kawamoto. Statics of magnetic bead chain in magnetic field. *Journal of Imaging Science and Technology*, 46(5):422–428, 2002.

[NST98] Y. Nakamura, Y. Suzuki, and Y. Terao. Tribocharging of toner particle in two-component developer. In *Proc. of IS&Ts NIP 14 International Conference on Digital Printing Technologies*, pages 315–318. Society for Imaging Science and Technology, 1998.

[OF02] D. Owen and Y. Feng. The modelling of multi-fracturing solids and particulate media. In *Proceedings of the Fifth World Congress on Computational Mechanics*, 2002.

[OFC02] D. Owen, Y. Feng, and M. Cottrell. Numerical modeling of industrial applications with multi-fracturing and particulate phenomena. In H. Konietzky, editor, *Numerical modeling in micromechanics via particle methods*, pages 3–12. A. A. Balkema Publishers, 2002.

[PA92] William H. Press and Seul A.Teukolsky. *Numerical Recipes in C*. Cambridge University Press, 1992.

[PBC96] H. Pollock, N. Burnham, and R. Colton. Attractive forces between micron-sized particles: A patch charge model. In Donald S. Rimai, editor, *Advances in Particle Adhesion*, pages 71–86. Overseas Publishers Associations, 1996.

[Peu02] W. Peukert. Skriptum zur vorlesung grundlagen der mechanischen verfahrenstechnik i. Technical report, TU Mnchen, 2002.

[PG96] Susanne Pfalzner and Paul Gibbon. *Many-Body Tree Methods in Physics*. Cambridge University Press, 1996.

[PGM02] W. Peukert, M. Götzinger, and C. Mehler. Novell concepts for characterization of particulate surfaces. *Applied Surface Sciences*, 196(202):30–40, 2002.

[Pur83] Edward M. Purcell. Berkely physics course. In *Electricity and Magnetism*. McGraw Hill College, 1983.

[RF01] A. J. Rushing and R. D. Fields. Toner satellite formation in electrostatically transferred images. *Journal of Imaging Science and Technology*, 45(2):187–197, 2001.

[RQ02] D. Rimai and D. Quesnel. Toner adhesion. *Journal of Imaging Science and Technology*, 46(3):200–207, 2002.

[Sch71] R. M. Schaffert. A new high sensitivity organic photoconductor for electrophotography. *IBM Journal of Research and Development*, 15(75), 1971.

[Sch75] R. M. Schaffert. *Electrophotography*. Focal Press, 1975.

[Sch92] Elmar Schrüfer. *Signalverarbeitung*. Carl Hanser Verlag, 1992.

[SN97] Yasushi Shinjo and Hideyuki Nishizawa. Study of tribo-charging characteristics between toner and carrier. In *Proc. of IS&Ts NIP 13 International Conference on Digital Printing Technologies*, pages 123–127. Society for Imaging Science and Technology, 1997.

[Spi77] Murray R. Spiegel. *Theory and Problem of Vector Analysis*. McGraw-Hill, 1977.

[SR99] J. Shaw and T. Retzlaff. particle simulation of xerographic line images. In *Proc. of IS&Ts NIP 15 International Conference on Digital Printing*, pages 467–469, 1999.

[Ste97] Charles W. Steele. *Numerical Computation of Electric and Magnetic Fields*. Chapman and Hall, 1997.

[SWW94] John K. Salmon, Grégoire S. Winckelmans, and Michael S. Warren. Fast parallel treecodes for gravitational and fluid dynamical N-body problems. *Intl. J. Supercomputer Appl.*, 8, 1994.

[Tab69] M. D. Tabak. Photogeneration effects in amorphous selenium. *Applied Optics Supplement 3: Electrophotography*, 65(4), 1969.

[Taj83] Hatsuo Tajima. Developing device. *United States Patent*, May 17 1983. #4,383,497.

[Tom98] Thomas N. Tombs. Electrostatic toner transfer to an intermediate: Results from a continuum model. In *Proc. of IS&Ts NIP 14 International Conference on Digital Printing Technologies*, pages 440–443, 1998.

[VB98] Richard Veregin and Robert Bartha. Metal oxide surface additives for xerographic toner: Adhesive forces and poweder flow. In *Proc. of IS&Ts NIP 14 International Conference on Digital Printing Technologies*, pages 358–361. Society for Imaging Science and Technology, 1998.

[Wol99] Stephen Wolfram. *The Mathematica Book*. Cambridge University Press, 1999.

[WS93] Michael S. Warren and John K. Salmon. A parallel hashed oct-tree N-body algorithm. In *Supercomputing '93*, pages 12–21, Los Alamitos, 1993. IEEE Comp. Soc.

[WS95a] Michael S. Warren and John K. Salmon. A parallel, portable and versatile treecode. In *Seventh SIAM Conference on Parallel Processing for Scientific Computing*. SIAM, 1995. available as http://qso.lanl.gov/papers/siam95/pp.ps.

[WS95b] Michael S. Warren and John K. Salmon. A portable parallel particle program. *Computer Physics Communications*, 87, 1995. available as http://qso.lanl.gov/papers/cpc/v9.ps.

[YC97] Arnold Yang and Ching-Yu Chou. Modeling of the tribo-charging between toner and carrier beads. In George Marshall, editor, *Recent Progress in Toner Technology*, pages 225–229. The Society for Imaging Science and Technology, 1997.